DOE/ER-0046/4
Vol. 1

Damage Analysis and Fundamental Studies

Quarterly Progress Report
Oct - Dec 1980

February 1981

U.S. Department of Energy
Assistant Secretary for Energy Technology
Office of Fusion Energy
Washington, DC 20545

Printed in the United States of America
Available from
National Technical Information Service
U.S. Department of Commerce
5285 Port Royal Road
Springfield, VA 22161

NTIS price codes
Printed copy: A14
Microfiche copy: A01

DOE/ER-0046/4
UC-20,20c
Vol. 1

Damage Analysis and Fundamental Studies

Quarterly Progress Report
Oct - Dec 1980

February 1981

U.S. Department **of** Energy
Assistant Secretary for Energy Technology
Office of Fusion Energy
Washington, DC 20545

FOREWORD

This report is the twelfth in a series of Quarterly Technical Progress Reports on *"Damage Analysis and Fundamental Studies"* (DAFS) which is one element of the Fusion Reactor Materials Program, conducted in support of the Magnetic Fusion Energy Program of the U. S. Department of Energy. The first eight reports in this series were numbered DOE/ET-0065/1 through 8. Other elements of the Materials Program are:

- Alloy Development for Irradiation Performance (ADIP)
- Plasma-Materials Interaction (PMI)
- Special Purpose Materials (SPM).

The DAFS program element is a national effort composed of contributions from a number of National Laboratories and other government laboratories, universities, and industrial laboratories. It was organized by the Materials and Radiation Effects Branch, Office of Fusion Energy, DOE, and a Task Group on *Damage Analysis and Fundamental Studies* which operates under the auspices of that Branch. The purpose of this series of reports is to provide a working technical record of that effort for the use of the program participants, for the fusion energy program in general, and for the Department of Energy.

This report is organized along topical lines in parallel to a Program Plan of the same title so that activities and accomplishments may be followed readily, relative to that Program Plan. Thus, the work of a given laboratory may appear throughout the report. The Table of Contents is annotated for the convenience of the reader.

This report has been compiled and edited under the guidance of the Chairman of the Task Group on *Damage Analysis and Fundamental Studies*, D. G. Doran, Hanford Engineering Development Laboratory. His efforts and those of the supporting staff of HEDL and the many persons who made technical contributions are gratefully acknowledged. M. M. Cohen, Materials and Radiation Effects Branch, is the Department of Energy counterpart to the Task Group Chairman and has responsibility for the DAFS Program within DOE.

Klaus M. Zwilsky, Chief
Materials and Radiation
Effects Branch
Office of Fusion Energy

CONTENTS

Page

CONTENTS (Cont'd)

FIGURES

Page

FIGURES (Cont'd)

FIGURES (Cont'd)

FIGURES (Cont'd)

TABLES

TABLES (Cont'd)

CHAPTER 1

IRRADIATION TEST FACILITIES

I. PROGRAM

Title: RTNS-II Operations (WZJ-16)

Principal Investigator: C. M. Logan

Affiliation: Lawrence Livermore National Laboratory

II. OBJECTIVE

The objectives of this work are operation of OFE's RTNS-II (a 14-MeV neutron source facility), machine development, and support of the experimental program that utilizes this facility. Experimenter services include dosimetry, handling, scheduling, coordination, and reporting.

RTNS-II is dedicated to materials research for the fusion power program. Its primary use is to aid in the development of models of high-energy neutron effects. Such models are needed in interpreting and projecting to the fusion environment engineering data obtained in other neutron spectra.

III. RELEVANT DAFS PROGRAM TASK/SUBTASK

TASK II.A.2,3,4.

TASK II.B.3,4.

TASK II.C.1,2,6,11,18.

IV. SUMMARY

Irradiations were done for a total of eight different experimenters from six laboratories. Five "piggy back" experiments were performed during this period. Major unscheduled outages during this period were due to experiment component failure and functional checks of accelerator equipment.

V. ACCOMPLISHMENTS AND STATUS

A. Irradiations - M. W. Guinan, C. M. Logan and D. W. Heikkinen (LLNL).

The HEDL-5 two-zone furnace experiment for N. Panayotou (HEDL) was continued during this quarter. The irradiations for R. Jones (PNL) were also continued, and four of five presently requested samples have been

completed. Another in-situ creep experiment on Nb for W. Barmore (LLNL) was done. The low temperature irradiation of resistivity samples by M. Guinan (LLNL) was also completed. The following "piggy back" experiments were also performed during this quarter.

1) Irradiation of electronic components for H. Murray (PPPL).
2) Activation analysis of RTNS-II target substrates. C. Logan (LLNL).
3) Irradiation of thermocouple wires. C. Logan (LLNL).
4) Effects of neutron irradiation on reproduction in mice. L. Goldstein (U.C. Medical Center, San Francisco).
5) Radiation effects on the thermal/mechanical properties of TFTR insulators. G. Hurley (LANSL).

B. RTNS-II Status - C. M. Logan and D. W. Heikkinen (LLNL)

Several improvements and/or modifications have been made at RTNS-II. Among these are:

1) A light array has been installed to provide for alignment verification on the TV beam monitoring system.
2) Monitoring equipment has been installed on the Haefely high voltage power supply.
3) A low fluence sample holder for "piggy back" experiments has been installed.

Several 50-cm target substrates have been tested and qualified. These are in final preparation for the tritium loading process. In addition, the 50-cm rotating target test assembly has been mechanically completed. The major unscheduled outages during this period were due to a complete functional test of the Haefely high voltage power supply and to turbo pump and heater failure on the HEDL two-zone furnace.

VII. FUTURE WORK

During the quarter, irradiations are scheduled for Panayotou (HEOL), and Jones (PNL). A "piggy back" experiment is scheduled for Srour (Northrup) and Nethaway (LLNL). Preparation is underway for an OFE radiation review.

VIII. PUBLICATIONS

None

I. PROGRAM

Title: Nuclear Data for Damage Studies and FMIT (WH025/EDK)
Principal Investigators: D.L.Johnson/F.M.Mann
Affiliation: Hanford Engineering Development Laboratory (HEDL)

II OBJECTIVE

The objective of this work is to supply nuclear data needed for damage studies and in the design and operation of the Fusion Material Irradiation Testing (FMIT) facility.

III. RELEVANT DAFS PROGRAM PLAN TASK/SUBTASK

All tasks that are relevant to FMIT use, with emphasis upon:

SUBTASK	II.A.2.3	Flux spectra definition in FMIT
TASK	II.A.4	Gas Generation Rates
SUBTASK	II.A.5.1	Helium Accumulation Monitor Development
SUBTASK	II.B.1.2	Acquisition of Nuclear Data

IV. SUMMARY

Additional evaluation of deuteron-induced activation of gold and aluminum was done to provide dose estimates.

An evaluation was made of the neutron environment at large angles to the 35-MeV deuteron beam in the FMIT test cell for comparison with positions at small angles to a 20-MeV beam.

Predictions of the neutron source characteristics for deuterons incident upon gold were made to aid in estimating dose near the accelerator.

V. ACCOMPLISHMENTS AND STATUS

A. Deuteron-Induced Activation of FMIT Materials --

D.L. Johnson (HEDL)

Activation of FMIT materials by deuterons will produce major contributions to residual gamma radiation doses following operation of the FMIT facility. Results of measurements of deuteron-induced activation of various materials were described previously in the DAFS quarterly report for January-March 1980. The following new results have been obtained.

An updated analysis of activation of thick gold by 35-MeV deuterons was completed. Gold is very important for reducing the activation in the vicinity of the beam caused by small beam losses. The new analysis showed a long-lived radioisotope (^{195}Au - 183 days) that was not previously observed. This isotope will build up to significant levels during long irradiations but can be easily shielded because of its low energy decay gamma rays.

Analysis of the activation of thick aluminum by 35-MeV deuterons was begun. Aluminum is the material currently planned for the beam tubes between the accelerator and the target and will, therefore, be activated by any beam losses. The results to date indicate significant quantities of ^{24}Na which decays away with a half life of 15 hours. They also show ^{22}Na which has a half life of 2.6 years and will build up to significant levels. Since the gamma rays are higher in energy, it is expected that, for comparable beam exposures, more shielding will be required than for activated gold.

A computer code was written to estimate activation cross sections for (d,p), (d,n), (d,2n), and (d,3n) reactions for any element with Z between about 20 and 83. These estimates are based upon systematics presented in Reference 1. The primary need for this information is for calculat-

ing the residual doses associated with activation of contaminants and corrosion products that may be present in the FMIT liquid lithium target. Previous dose estimates were based upon crude activation cross section estimates of 0.5 barns above threshold for any reaction, hence a significant improvement in accuracy is expected.

B. Neutron Environment in FMIT - F.M.Mann (HEDL)

Flux, dpa, and He production at large angles from the deuteron beam were investigated at E_d = 35 MeV to compare damage parameters at these positions with parameters obtained for E_d = 20-MeV operation. Although the flux spectrum is similar for these positions and for 20-MeV operation, the flux is at least a factor of 6 lower than could be obtained with an optimized target at 20 MeV, moreover, significant gradients exist [$(\Delta dpa/dpa)/\Delta y$ (mm) $\simeq$ 7-11%].

C. Cross Section Calculations - F.M.Mann (HEDL)

Since gold will be used to plate the drift tubes down most, if not all, of the length of the FMIT linac, the neutron source from deuterons on Au must be known to determine radiation zoning specifications. Unfortunately there is not enough experimental data to determine this neutron source. Therefore, theoretical models and the experimental data of Meulders *et al*[2] were used to predict the needed neutron spectra.

Equilibrium[3] and pre-equilibrium[4] models treat that part of the reaction which proceeds by emitting a particle out of the composite system d + Au. The reaction cross section code PRECO-D[5] was used to calculate this part of the reaction for thin targets as a function of deuteron energy. PRECO-D also incorporates the recently found angular distribution systematics of Kalbach and Mann[6] to determine the angular dependence of the neutron yields.

The reaction cross section input to PRECO-D was calculated using the HEDL

code HAUSER*5,[7] using standard optical model parameters. All other parameters were taken to be the standard PRECO-D values.

Because the deuteron is so weakly bound, the deuteron becomes strongly polarized in the nuclear field and the effective deuteron reaction cross sections increase at low energies.[8] Using the relative systematics of Peaslee,[9] the effect of this Phillips-Oppenheimer effect was included. Equivalent thick target yields were generated by combining the above thin target data with the deuteron stopping power.[10] These thick target data were then given an overall normalization factor based upon the 16-MeV data of Meulders et al. which is predominately equilibrium and pre-equilibrium.

At higher deuteron energies, deuteron stripping must be added. The proton is stripped from the weakly bound deuteron to yield a forward peaked neutron distribution.[11] For thin targets, the shape of this part of the neutron spectrum is predicted to be roughly Gaussian in both neutron energy and emission angle and is nearly deuteron-energy independent. Therefore, the thick target stripping was obtained as a sum of Gaussians. The parameters of this part of the model were adjusted to fit the 33-MeV data of Meulders et al., which clearly show a breakup peak.

The results of the two models were added to form the final values as a function of deuteron energy. Figure 1 presents the E_d = 33-MeV data of Meulders et al. with the results of this evaluation at E_d = 30 and 35 MeV.

D. CSEWG Task Group - F.M.Mann (HEDL)

The Cross Section Evaluation Working Group (CSEWG) has created a working group under the chairmanship of F.M.Mann to coordinate cross section evaluation efforts above 20 MeV for the ENDF/B system.

VI. REFERENCES

1. J. Lange and H. Munzel, KFK-767, May 1968.
2. J.P.Meulders, P.Leleux, P.C.Macq, and C.Pirat,"Fast Neutron Yields and Spectra from Targets of Varying Atomic Number Bombarded with Deuterons from 16 to 60 MeV," Phys. Med. Bio. 20 (1975) 235.
3. V.F.Weisskopf and D.F.Ewing, "On the Yield of Nuclear Reactions with Heavy Elements," Phys. Rev. 57 (1940) 472.
4. C.Kalbach, "The Griffin Model, Complex Particles, and Direct Nuclear Reactions," Z.Phys. A283 (1977) 401.
5. C.Kalbach, "PRECO-D, Program for Calculating Pre-equilibrium and Direct Double Differential Cross Sections," Triangle Universities Nuclear Laboratory informal report, Durham, NC, 1980.
6. C.Kalbach and F.M.Mann, "Phenomonology of Emitted Particle Angular Distributions for Preequilibrium Reactions," Phys. Rev. C23 (1981) 112.
7. F.M.Mann, HAUSER*5, A Computer Code to Calculate Nuclear Cross Sections., HEDL-TME-78-83, Hanford Engineering Development Laboratory, Richland, WA, 1979.
8. J.R.Oppenheimer and M. Phillips, "Note on the Transmutation Function for Deuterons," Phys. Rev. 48 (1935) 500.
9. D.C. Peaslee, "Deuteron-Induced Reactions," Phys. 74 (1948) 1001.
10. H.H.Anderson and J.F.Ziegler, Hydrogen Stopping Powers and Ranges in All Elements. Pergamon Press 1977, New York.
11. R.Serber, "The Production of High Energy Neutrons by Stripping," Phys. Rev. 72 (1947) 1008.

VII. FUTURE WORK

Continued updating of deuteron-induced activation data.

Evaluation of activation and neutron sources associated with beam stops used for tuning of accelerator.

Investigation *of* discrepancy between calculated and experimental results for the transmission of FMIT neutrons through thick iron (described in DAFS July-Sept. 1980 quarterly report).

VIII. PUBLICATIONS

None

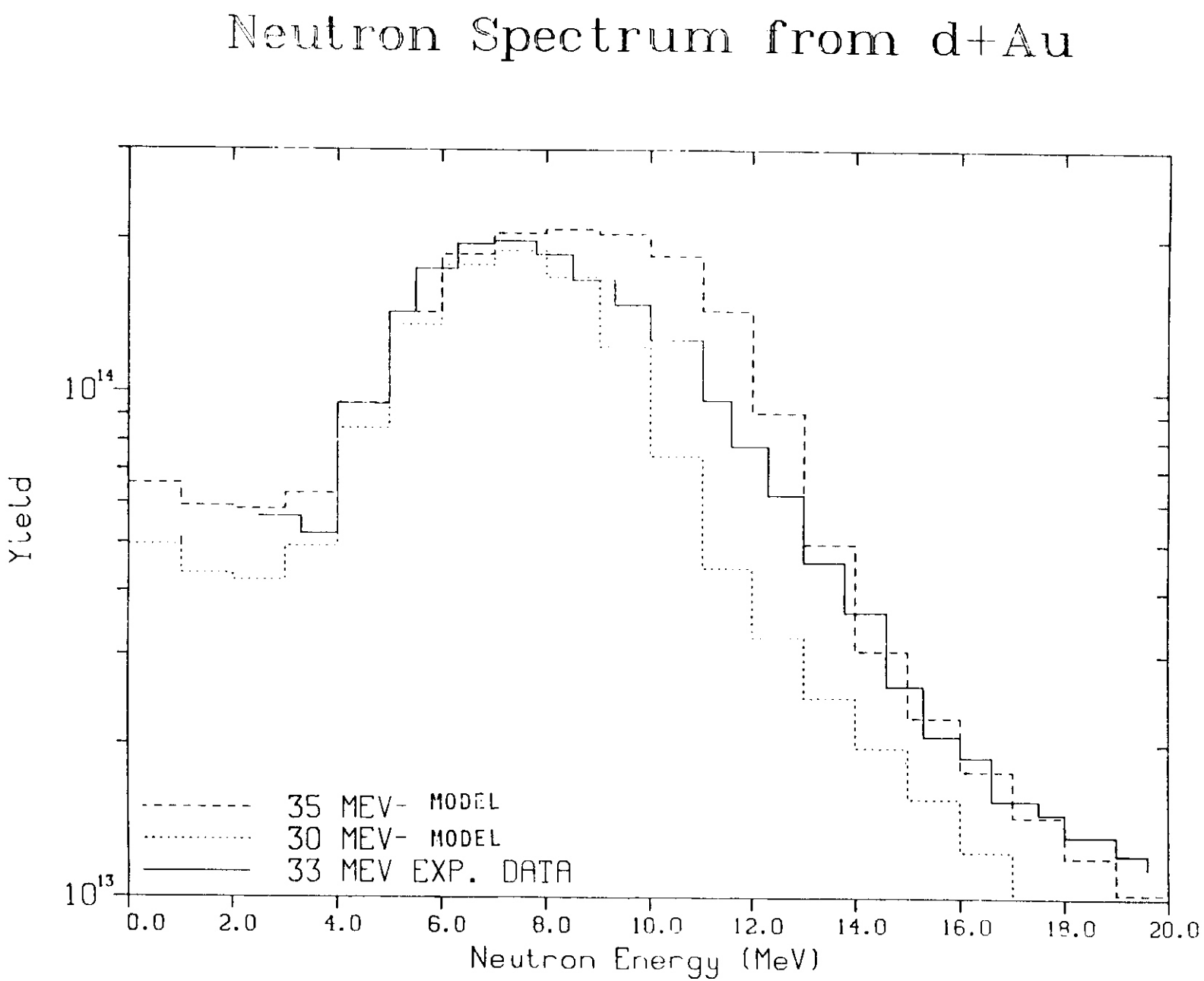
Neutron Spectrum from d+Au
Yield
10^{14}
10^{13}
35 MEV- MODEL
30 MEV- MODEL
33 MEV EXP. DATA
0.0
2.0
4.0
6.0
8.0
10.0
12.0
14.0
16.0
18.0
20.0
Neutron Energy (MeV)

CHAPTER 2

DOSIMETRY AND DAMAGE PARAMETERS

HIGHLIGHTS

CHAPTER 2. DOSIMETRY AND DAMAGE PARAMETERS

Fission Reactor Dosimetry (ANL)

A neutron spectral measurement was made in the core of the Omega West Reactor (LASL) on October 21, 1980. All radiometric samples have been analyzed and flux values are presented along with an unfolded spectrum.

The dosimeters were received in December 1980 from the ORR-MFE 2 irradiation. The capsules are now being opened and samples prepared for gamma counting.

I. PROGRAM

Title: Dosimetry and Damage Analysis
Principal Investigator: L. R. Greenwood
Affiliation: Argonne National Laboratory

II. OBJECTIVE

To establish the best practicable dosimetry for mixed-spectrum reactors and to provide dosimetry and damage analysis for OFE experiments.

III. RELEVANT OAFS PROGRAM TASK/SUBTASK

SUBTASK II.A.1.1 Flux-spectral definition in a tailored fission reactor.

SUBTASK II.A.1.3 Applications.

IV. SUMMARY

The neutron flux spectrum was measured in the Omega West Reactor (LASL) in October. Flux values and a spectrum are now available. Dosimeters were received in December from the ORR-MFE2 irradiation. The status of all other irradiations is summarized in Table I.

V. ACCOMPLISHMENTS AND STATUS

A. Characterization of the Omega West Reactor (LASL)
L. R. Greenwood (ANL)

An irradiation was conducted in the Omega West Reactor (OWR) at Los Alamos Scientific Laboratory on October 21, 1980. Samples were placed in a furnace constructed by R. Van Konynenburg (LLL), which will be used for fission-fusion (RTNS II) correlation experiments by LLL and HEOL. The irradiation lasted for 8 hours with an average power level of 7.8 MW (7.63 hours at 8.0 MW). The capsule temperature was about 65°C during most of the irradiation.

Table I. Status of Reactor Experiments

Facility/Experiment		Status and Comments
ORR	- MFE1	Analysis complete.
	- MFE2	Samples received 12/80.
	- MFE3	Planning in progress.
	- MFE4A,B	Irradiation in progress.
	- TBC07	Analysis complete.
	- TRIO	Planning in progress.
HFIR	- CTR 30,31,32	Irradiation in progress.
	- T1,T2	Irradiation in progress.
	- RB1	Planning in progress.
Omega West	- Spectral Run	Analysis complete.
	- HEDL/LLL1	Irradiation in progress.
EBR II	- X287	Analysis in progress.

Dosimetry specimens were placed in an aluminum cylinder (0.75" O.D. x 0.74" length) with nine holes. An attempt was made to position the entire assembly at the maximum flux position near core center. Since this identical setup will be used for most irradiations, no additional gradients were measured. Analysis of our data shows that flux values within the small capsule vary less than 2%.

After irradiation, the samples were shipped to ANL for analysis. Helium monitors were also included and these were sent to D. Kneff (Rockwell International) for analysis. A total of 40 samples were gamma counted and 32 reactions were measured for spectral analysis. The final activation rates are listed in Table II.

Twenty-nine reactions were then used to unfold the neutron spectrum. The input spectrum was taken from previous measurements in the Oak Ridge Research Reactor since no neutronics calculations are available. All activation cross sections and errors were taken from ENDF/B-V. The STAYSL-adjusted spectrum is shown in Fig. 1 and the 8-MW flux integrals are. as follows:

Energy Range, MeV	Flux Integral (n/cm^2-s)	Error, %
Total	1.81×10^{14}	5
Thermal	7.3×10^{13}	15
>0.11	5.7×10^{13}	9
>1.0	2.9×10^{13}	7
>5.0	2.0×10^{12}	11
>10.0	4.5×10^{10}	16

More complete results are available on request.

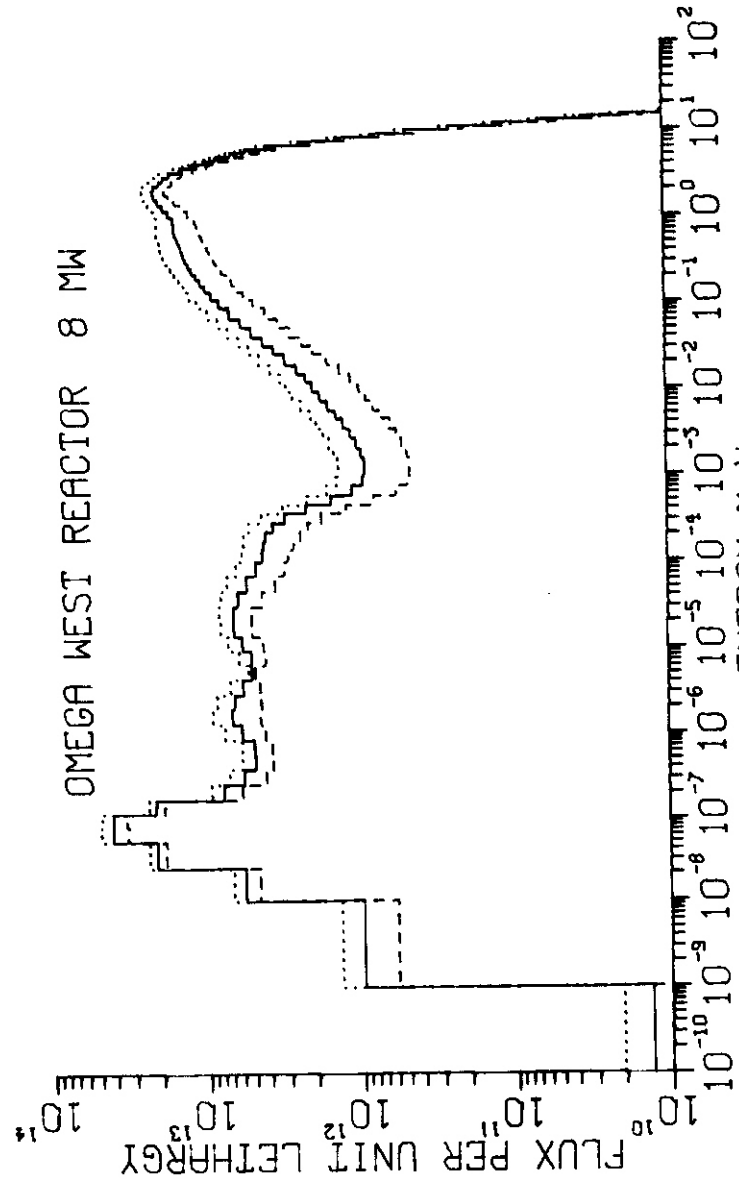

Figure 1. Flux spectrum for the Omega West Reactor at 8 MW, core center. Twenty-nine reactions were used. Dotted and dashed lines represent one standard deviation error limits.

Table II. Saturated Activation Rates for the Omega West Reactor (7.8 MW, Core Center)

Reaction	$\sigma\phi$ (atoms/atom-s)	Reaction	$\sigma\phi$ (atom/atom-s)
$^{59}Co(n, \gamma)\ ^{60}Co$	2.10×10^{-9}	$^{237}Np(n, f)$ t Gd	6.19×10^{-11}
+ Gd cover	4.26×10^{-10}	$^{237}Np(n, \gamma)\ ^{238}Np$ + Gd	3.74×10^{-9}
$^{197}Au(n, \gamma)\ ^{198}Au$	1.17×10^{-8}	$^{27}Al(n, \alpha)\ ^{24}Na$	2.32×10^{-14}
+ Gd cover	7.47×10^{-9}	$^{54}Fe(n, p)\ ^{54}Mn$	2.99×10^{-12}
$^{63}Cu(n, \gamma)\ ^{64}Cu$ + Gd	2.36×10^{-11}	$^{54}Fe(n, a)\ ^{51}Cr$	2.82×10^{-14}
$^{58}Fe(n, \gamma)\ ^{59}Fe$	6.13×10^{-11}	$^{55}Mn(n, 2n)\ ^{54}Mn$	8.44×10^{-15}
+ Gd cover	9.20×10^{-12}	$^{58}Ni(n, p)\ ^{58}Co$	3.69×10^{-12}
$^{45}Sc(n, \gamma)\ ^{46}Sc$	1.22×10^{-9}	$^{60}Ni(n, p)\ ^{60}Co$	8.24×10^{-14}
+ Gd cover	1.31×10^{-10}	$^{63}Cu(n, a)\ ^{60}Co$	1.83×10^{-14}
$^{94}Zr(n, \gamma)\ ^{95}Zr$	3.93×10^{-12}	$^{46}Ti(n, p)\ ^{46}Sc$	3.89×10^{-13}
$^{96}Zr(n, \gamma)\ ^{97}Zr$	2.90×10^{-11}	$^{47}Ti(n, p)\ ^{47}Sc$	6.24×10^{-13}
$^{176}Lu(n, \gamma)\ ^{177}Lu$	2.29×10^{-7}	$^{48}Ti(n, p)\ ^{48}Sc$	1.01×10^{-14}
+ Gd cover	3.30×10^{-8}	$^{90}Zr(n, 2n)\ ^{89}Zr$	3.82×10^{-15}
$^{235}U(n, f)$	2.18×10^{-8}	$^{93}Nb(n, 2n)\ ^{92m}Nb$	1.63×10^{-14}
+ Gd cover	2.68×10^{-9}		
$^{238}U(n, f)$	1.19×10^{-11}		
$^{238}U(n, \gamma)\ ^{239}Np$	5.31×10^{-10}		
+ Gd cover	4.17×10^{-10}		

Note: The above values are not corrected for neutron self-shielding. Such corrections are spectral dependent and are done during the spectral adjustment process. All other known corrections have been included.

B. Dosimetry for the ORR-MFE2 Irradiation

L. R. Greenwood (ANL)

Dosimetry samples were received in December for the ORR-MFE2 irradiation. These specimens were irradiated for about 15 months in position E7 between September 1978 and March 1980. Sixteen small specimens were placed inside experimental assemblies and two long tubes contained gradient wires and helium specimens. The samples are currently being disassembled at ANL and prepared for gamma counting. Helium specimens will be sent to Rockwell International for analysis.

VI. REFERENCES

None.

VII. FUTURE WORK

Some of the irradiations listed in Table I will take several years to complete and many more will be added. Damage calculations will be performed for the Omega West Reactor and most other experiments. Helium measurements (Rockwell International) will be integrated with the radiometric data.

VIII. PUBLICATIONS

1. L. R. Greenwood, The Status of Neutron Dosimetry and Damage Analysis for the Fusion Materials Program, Proc. Int. Conf. on Nucl. Cross Sections for Technology, NBS 594, p. 812, September 1980.

I. PROGRAM

Title: Helium Generation in Fusion Reactor Materials
Principal Investigators: O. W. Kneff and Harry Farrar IV
Affiliation: Rockwell International, Energy Systems Group

II. OBJECTIVE

The objectives of this program are to measure helium generation rates of materials for Magnetic Fusion Reactor applications in the various neutron environments used for fusion reactor materials testing, to characterize these neutron test environments, and *to* develop helium accumulation neutron dosimeters for neutron fluence and energy spectrum dosimetry in **these** test environments.

III. RELEVANT DAFS PROGRAM PLAN TASK/SUBTASK

SUBTASK II.A.2.2	Flux-Spectral Definition in RTNS-II
SUBTASK II.A.4.2	T(d,n) Helium Gas Production Data
SUBTASK II.A.4.3	Be(d,n) Helium Gas Production Data

IV. SUMMARY

Helium analyses have been initiated for the helium accumulation dosimetry materials irradiated in the neutron characterization experiment at RTNS-II. Analyses of the separated isotopes of molybdenum irradiated in the RTNS-I, RTNS-II, and Be(d,n) neutron fields are in progress. The emphasis during the present period was on improving the gas mass spectrometer sensitivity for these samples.

V. ACCOMPLISHMENTS AND STATUS

Helium Production by Fast Neutrons -- D. W. Kneff, B. M. Oliver, M. M. Nakata, and Harry Farrar IV (Rockwell International, Energy Systems Group)

Helium analyses have been initiated for the pure element helium accumulation dosimetry rings irradiated in the joint Rockwell International-Argonne National Laboratory (ANL)-Lawrence Livermore National Laboratory (LLNL) experiment to characterize the neutron spectrum of RTNS-II. This irradiation was described in detail in the previous progress report.[1] During the present reporting period the rings were etched (to remove helium enhancement and depletion effects due to alpha recoils), segmented, and weighed, and a number of samples have subsequently been analyzed for helium by high-sensitivity gas mass spectrometry. The initial results indicate that the generated helium concentrations are about as expected from the irradiation parameters, and indicate a flux about three times higher than for the earlier RTNS-I irradiations. The higher fluence obtained (a factor of five) will facilitate measuring the lower helium generation cross sections expected for some of the separated isotope samples incorporated in the experiment. These preliminary results also show that there was a slight offset of the irradiation capsule from the neutron source axis, producing a ~±15% variation in neutron fluence around the periphery of the capsule. This offset is significantly smaller than that observed in our most recent RTNS-I experiment.

A series of helium analyses is also in progress to measure the cross sections of the molybdenum pure element and separated isotope samples irradiated in the RTNS-I, RTNS-II, and Be(d,n) neutron fields. These measurements are sponsored in part by the Office of Basic Energy Sciences of the Department of Energy. It was reported in a previous progress report[2] that the helium generated in molybdenum could be released from the sample without vaporizing it, by heating the molybdenum with nickel to form a eutectic alloy. This has the advantage, for low-level helium

measurements, of reducing the heating in the mass spectrometer furnace and thus reducing the background helium release. This procedure was tested extensively during the present reporting period, using previously-irradiated molybdenum samples from EBR-II having much larger helium concentrations. It was found, however, that this alloying technique does not consistently release all of the helium, occasionally leaving as much as 4% in the molten alloy. The incomplete helium release could not be explained by incomplete alloying, as the alloying was confirmed by X-ray diffraction analysis of representative alloy products.

As a result of these findings, alternate procedures are now being tested to vaporize, rather than alloy, the molybdenum. Smaller graphite crucibles are being used, and initial results indicate that a significant heating reduction, and consequently a smaller helium background, can be obtained. It should be noted that the standard crucibles work well for most materials, and that the present efforts are aimed at measuring the particularly small cross sections of the high-mass molybdenum isotopes.

VI. REFERENCES

1. D. W. Kneff, B. M. Oliver, M. M. Nakata, and H. Farrar IV, "Characterization of the RTNS-II Neutron Field," in Damage Analysis and Fundamental Studies, Quarterly Progress Report July-September 1980, DOE/ER-0046/3, U.S. Department of Energy (1980).

2. D. W. Kneff, B. M. Oliver, M. M. Nakata, and H. Farrar IV, "Helium Accumulation Neutron Dosimetry for the T(d,n) and Be(d,n) Neutron Irradiation Environments," in Damage Analysis and Fundamental Studies, Quarterly Progress Report January-March 1980, DOE/ER-0046/1, U.S. Department of Energy (1980).

VII. FUTURE WORK

Analyses of the helium accumulation dosimetry materials from the RTNS-II characterization experiment will continue during the next quarter.

Helium analyses will also be continued to determine the (n,total helium) cross sections for the separated isotopes irradiated in the RTNS-I, RTNS-II, and Be(d,n) neutron spectra.

CHAPTER 3

FUNDAMENTAL MECHANICAL BEHAVIOR

I. PROGRAM

Title: Simulating the CTR Environment in the HVEM

Principal Investigators: W. A. Jesser and R. A. Johnson

Affiliation: University of Virginia

II. OBJECTIVE

The objective of this work is to experimentally investigate some of the critical parameters employed in recent helium embrittlement theories.

III. RELEVANT DAFS PROGRAM TASK

Task II.C.14.2 Fundamental relations between microstructure and fracture mechanisms.

IV. SUMMARY

Experimental evidence indicates that a helium-filled, bubble-hardening model can explain helium embrittlement at tensile test temperatures below ~ 550° C. Critical values for edge-to-edge bubble spacing ($L_c \leq 30$ nm) and bubble diameter ($d_c \leq 4$ nm) for the onset of brittle fracture were found. In this test temperature regime, those bubbles may be slightly overpressurized. In contrast, at test temperatures above 550° C, no critical values of L_c and d_c were discovered. In addition, bubble pressure was not a factor in this temperature range. Finally, no critical values for α_R, the area fraction of bubbles covering grain boundaries, could be found at any temperature.

V. ACCOMPLISHMENTS AND STATUS

Microstructural Aspects of Helium Embrittlement, J. I. Bennetch and W. A. Jesser, Materials Science Department, University of Virginia, Charlottesville. Virginia 22901.

1. Introduction

At present there are two main schools of thought concerning the role of helium in the high temperature embrittlement of irradiated metals. One school maintains that helium only serves to alter the process of thermal aging in irradiated austenitic steels. The appearance on grain boundaries of precipitates that differ from those normally found in aged unirradiated steels is thus thought to lead to the observed brittle behavior at high test temperatures[1, 2]. However, the more popular school of thought bases its embrittlement model on the concept of stress-induced growth of helium-filled cavities or bubbles on grain boundaries [3, 4]. These bubbles presumably grow until the grain boundary is sufficiently weakened to allow intergranular failure to take place.

It is the intent of this report to examine experimentally the parameters in the theoretical treatment of fracture behavior in steels as set out by proponents of the helium gas bubble model. Such parameters as bubble size and spacing, α_R (the area fraction of grain boundary occupied by helium bubbles) and helium bubble gas pressure will be correlated with the type of failure in order to find which parameters correlate well.

2. Experimental Details

40-μm thick tensile samples of solution-annealed stainless steel type 316 were punched into ribbons whose center portions were electropolished to electron transparency for 500 kV electrons. They were then helium ion irradiated to doses up to 3×10^{18} cm^{-2} at either high (600°-650" C) or low (250"-300" C) irradiation temperatures to produce varying sizes and densities of bubbles, dislocation loops and precipitates. Post-

irradiation annealing treatments served to coarsen these radiation-induced microstructural features. In-situ tensile tests were performed inside a high voltage electron microscope (HVEM) at strain rates initially at $\sim 10^{-4}\ S^{-1}$, and at temperatures ranging from 25° to 650" C. Specimens were aged for at least one hour at the test temperature before tensile testing commenced. More complete information on experimental details can be obtained from previous DAFS reports.

3. Experimental Results

a. Bubble, Void Diameter and Spacing

Both the concepts of bubble spacing, L, and bubble diameter, d, as parameters are important in recent helium bubble models of helium embrittlement [5-10]. In order to obtain experimental values of L and d from the literature, one must either rely on values of ρ (bubble density in the matrix) and d quoted in the text or else estimate these values from printed micrographs, if ρ and d are not given. The center-to-center bubble spacing, ℓ, can be obtained by the classical formula [11]; however since dislocations intersect obliquely at bubble surfaces, not at bubble centers, it was felt a more fundamental parameter would be edge-to-edge bubble spacing, L, which can be computed as:

$$L = \ell - d = \frac{1}{\sqrt{\rho d}} - d$$

Computed values of L in irradiated austenitic steels and from the literature, together with those values of L measured from 316 and 304 stainless steel samples tested in this laboratory are plotted against test temperatures in Figure 1. Circular symbols denote data obtained from neutron irradiated samples and square symbols indicate L values obtained from ^4He

ion irradiated samples or ^3He containing specimens. Ductility is indicated by the degree of shading of each symbol: complete shading = transgranular (T) fracture, no shading = intergranular (I) fracture, half shading = mixed (I + T) fracture, and crosshatching = channel (C) fracture. Numbers 15 and 18 indicate data obtained from this laboratory. Note that this fracture map does not include creep data, because elongation rates averaged $\sim 10^{-4}\ S^{-1}$.

An examination of the implications of Figure 1 revealsanumber of interesting observations. First, the shape of the zone of L values which represents samples that exhibited a mixed (I + T) fracture behavior resembles a "J" curve. The shape itself of the "J" curve suggests that the effect of cavity spacing on the process of helium embrittlement can be separated into two distinct parts: a roughly horizontal section ($< \sim$ 550" C) and a nearly vertical section ($> \sim$ 550" C). The horizontal section denotes an athermal effect of L on fracture below $\sim$ 550" C where for a critical value, $L_c \lesssim \sim$ 30 mm the onset of brittle fracture is evidenced. Above $\sim$ 550" C, the vertical section of the L-Temperature curve is an indication that the bubble spacing has little influence on fracture behavior. Thus irradiated austenitic steels fail in an (I + T) mode for test temperatures ranging from $\sim$ 550° C to 700" C and in an I mode for temperatures above 700" C, independent of L. In contrast, unirradiated steels fail in a transgranular mode for the same test temperature ranges.

A plot of cavity diameter, d, vs. test temperature closely parallels the "J" shape of Figure 1, since d is probably not independent of L. By use of the same arguments as before, it was found that there is a critical

bubble diameter ($d_c \leq \sim 4$ nm) for the onset of brittle fracture below $\sim$ 550" C and no correlation of cavity size with fracture type above that test temperature.

b. Area Fraction of Bubbles Occupying Grain Boundaries

Another important parameter in the helium bubble model of helium embrittlement is α_R, the area fraction of bubbles occupying grain boundaries. Presumably the more fractional area occupied by bubbles, the weaker the grain boundary, and the more susceptible the irradiated specimens are to premature intergranular failure. Proponents of this theory would thus predict $(\alpha_R)_{brittle} > (\alpha_R)_{ductile}$. Further, a critical value for brittle fracture of $\alpha_R = 0.1$ has been assigned by Trinkhaus and Ulmaier [7, 8] in their recent theory of helium embrittlement.

To calculate values of α_R from data given in the literature is again no easy task. Estimates were made from grain boundary micrographs. More commonly, a less satisfactory method was employed. The fractional coverage of bubbles in an arbitrary plane in the matrix, $_m\alpha_R$, was computed from values of cavity densities and diameters quoted in the literature. The equation employed for the calculation is $_m\alpha_R = \pi(d)^3\rho/6$ = swelling, and α_R was directly measured. These values are smaller than the actual α_R values by some factor; however, most of the values of $_m\alpha_R$ thus computed are probably not off by more than a factor of ten. All these computed values of a_R and $_m\alpha_R$ from the literature, together with those values calculated from data from this laboratory, were plotted as a function of test temperature in Figure 2. All symbols have the same meaning as before. Those symbols with an asterisk denote $_m\alpha_R$ values, all others are α_R values. The

square symbol marked #24 is the only value derived from a creep test and symbol #5 the only non-austenitic steel alloy (Ni-6% W).

Again, there are several important aspects to this Figure. First, below about 600" C, there is no correlation between (α_R) and test temperature. Indeed, both at 25° C and at 500" C, instances of brittle fracture occurred below α_R = 1%, while ductile failure still occurred for α_R values up to ∿ 30%. Second, above 600" C, almost all samples failed in a brittle mode, independent of values of α_R and $_m\alpha_R$. All failed for α values < 0.1 and most fell below 0.01 in magnitude. Clearly, these findings imply α_R is not a critical parameter at any test temperature.

c. Helium Cavity Gas Pressure

The amount of overpressurization in cavities is another parameter in some theoretical considerations of helium ernbrittlement. Larger gas pressure in grain boundaries is thought to lead to a shorter rupture time [8, 9, 13]. However, to measure this pressure is a very difficult task for the experimentalist. In order to circumvent this problem, a different approach to examine the effects of pressure was explored. First, the number density of helium atoms, N_{eq} that could be accommodated in equilibrium bubbles of diameter d and density ρ was calculated by using the method of Cost and Chen [26]. Then, knowing the neutron or helium fluence, the concentration of helium N_{imp} was estimated [27, 28]. If one assumes all the helium migrated to the cavities (an overestimate), the ratio, N_{imp}/N_{eq}, should be an indication of the relative overpressure of the helium-filled cavities (i.e., if $N_{imp}/N_{eq} >> 1$, the cavities are probably overpressurized) Indeed, when a plot of N_{imp}/N_{eq} vs. the test temperature, T_{test} is exam-

ined (Figure 3), one can see a cluster of data points represents (I + T) and (I) mode failure for $N_{imp}/N_{eq} > 1$ for T < ∿ 600" C. However, it must be pointed out that those ratios are rough overestimates, so that the actual ratios will be closer to equilibrium than is indicated by this figure. Further, for temperatures > ∿ 600" C, this ratio can assume any value and brittle fracture will still occur. This suggests that over-pressurization may possibly be a factor in the helium embrittlement process for test temperatures below ∿ 600° C. However, it is clear that pressure as a parameter, is not important at high test temperatures.

4. Discussion

From the previous section, it appears there are two temperature regimes in which two distinct processes of helium embrittlement occur in austenitic steels. At temperatures below ∿ 550° C, the parameters L, d, and possibly helium bubble pressure are significant. This suggests a bubble-hardening mechanism in this temperature range where a high density of small, possibly overpressurized cavities provides obstacles to dislocations moving through the grain interior. It has been observed for some time that a high density of small dislocation loops and bubbles can increase the yield stress in neutron irradiated materials by a factor proportional to $\frac{1}{\ell}$ [14, 30]. In addition, Bloom and Stiegler claimed that a given density of small bubbles had a larger effect on increasing the yield stress than an equal density of dislocation loops [21]. However, despite large increases in yield strength, none of these irradiated samples failed in a brittle fashion at temperatures below ∿ 500" C, as reported by those same authors. In view of this result the effect on ductility of more closely

packed bubbles, as produced by this facility in 316 stainless steel, is to further harden the matrix, apparently by a larger amount than the grain boundary. As the equicohesive temperature is lowered by this method, brittle fracture can ensue at a lower temperature. Indeed any transgranular cracks that did propagate through grains containing these high bubble populations were almost always cleavage in nature. The presence of only cleavage or grain boundary cracks indicated the inability of dislocations in front of the crack tip to cross slip as normally happens with dislocations associated with ductile transgranular cracks. This cleavage like transgranular fracture is further evidence that extremely close-packed small bubbles can embrittle solids by acting as effective dislocation obstacles.

Helium embrittleinent is normally associated with high irradiation/test temperatures. It can be deduced from the results of the previous section that for temperatures above $\sim 550^{\circ}$ C, neither the magnitude of bubble size, spacing, fractional coverage on grain boundaries, nor gas pressure has an appreciable effect on ductility. These observations would seem to preclude any further consideration of a model of helium embrittlement based on a weakening of grain boundaries due to the presence of helium bubbles. Yet helium does have a pronounced effect on high temperature fracture. Sagüés observed that as little as 5 appm of helium caused a significant amount of embrittling in creep tested DIN 1.4970 stainless steel samples tested at 700" C [24]. Moreover, he observed that this effect saturated at $\sim$ 20 appm of helium. In contrast, at test temperatures well below 700" C ($T < \sim$ 500" C) some 316 stainless steel specimens containing large amounts of He (irradiated at this facility to doses of 10,000

appm and greater) failed in a purely transgranular fashion. Clearly, the presence of large amounts of helium is not sufficient by itself to cause embrittlement. It is tempting to propose as an alternative to the helium bubble model, a helium accelerated thermal aging model where helium serves to drive the formation of more brittle grain boundary precipitates than those found in normal unirradiated thermally aged specimens. In fact, this effect has been observed in helium irradiated samples irradiated at this facility to high doses (1000 appm He and higher) and neutron irradiated samples irradiated in HFIR to doses of ∿ 3300 appm He [30]. In contrast, a recent study on radiation-enhanced precipitation revealed no difference between precipitates found in EBR-II irradiated samples (helium concentrations up to ∿ 20 appm) and those produced by normal thermal aging processes in aged unirradiated austenitic alloys. In spite of the lack of an observable difference in the precipitates of the irradiated and unirradiated specimens, the EBR-II irradiated ones failed intergranularly above 700" C and represent the majority of the points in Figures 1, 2, and 3, denoting neutron irradiations. In view of the above conflicts, a helium accelerated thermal aging model is also inadequate.

However, there is some experimental evidence of high-temperature, helium-assisted, solute segregation to grain boundaries with EBR-II samples. On a PE-16 steel alloy tested at ∿ 575" C, Sklad found an excess of highly embrittling P and S impurity atoms, in addition to a Ni excess and Cr depletion, at the intergranular fracture surface [16]. This sample contained * 8 appm helium. In contrast, Horton found a large Cr excess (with respect to Ni and Fe) on the brittle part of the fracture surface of a 316

stainless steel, He ion irradiated to a large dose (> 20,000 appm **He)** and tested at 600" C [31]. He made no attempt to search for the presence of impurities. In addition, it is known than an excess of Ni or Cr tends to enhance the deleterious effect of impurity segregation to grain boundaries [32]. Hence, the results of both cases hint at the possibility of helium-driven temper embrittlement.

5. Conclusions

A capsule account of the conclusions reached from this investigation follows. For austenitic stainless steel:

a. $T_{test} < 550°$ C

1. α_R is not a critical parameter
2. $L_c < \sim 30$ nm, $d_c < \sim 4$ nm for the onset of brittle fracture
3. Bubbles may be slightly overpressurized in the critical region for intergranular fracture.

b. $T_{test} > 550$" C

α_R, d, L and bubble pressure are not critical parameters in determining the fracture type.

VI. REFERENCES

1. Z. E. Ostrovsky, G. A. Sernyaev, P. P. Grintchuk, S. N. Votinov, and V. I. Prokhorov, "The Effect of Neutron Irradiation on Second Phase Precipitation Processes," Trans. Iron Steel Inst. Japan 11 (1971) 289.

2. R. B. Roy and B. Solly, "Einbrittlement of Neutron-Irradiated 20Cr-25Ni-Nb Austenitic Steel at 650" C," J. Iron Steel Inst. 205 (1967) 58.

3. D. R. Harries, "Neutron Irradiation Embrittlement of Austenitic Stainless Steels and Nickel Based Alloys," J. Brit. Nucl. Energy Soc. 5 (1966) 74.

4. R. S. Barnes, "Embrittlement of Stainless Steels and Nickel-Based Alloys at High Temperature Induced by Neutron Radiation," Nature 206 (1965) 1307.

5. S. H. Goods and W. D. Nix, "A Comparison of the Embrittling Effects of H_2O Bubbles in Ag With Those of Helium Bubbles in Ni-6%," Acta Met. 24 (1976) 1041. (Ni-6% W alloy)

6. G. W. Greenwood, "The Coarsening of Intergranular Bubbles Containing Sparingly Soluble Monatomic Gas," Phil. Mag. 31 (1975) 673.

7. H. Trinkhaus and H. Ullmaier, "Some Aspects of the Theory of Helium Embrittlement," J. of N. Mat. 85 and 86 (1979) 823.

8. H. Trinkhaus and H. Ullmaier, "A Model for the High-Temperature Embrittlement of Metals Containing Helium," Phil. Mag. A. 39 (1979) 563.

9. D. Hull and D. E. Rimmer, "The Growth of Grain Boundary Voids Under Stress," Phil. Mag. 4 (1959) 673.

10. W. O. Nix, O. K. Matlock, and R. J. Dimelfi, "A Model for Creep Fracture Based on the Plastic Growth of Cavities at the Tips of Grain Boundary Wedge Cracks," Acta Met. 25 (1977) 495.

11. M. F. Ashby, "The Hardening of Metals by Non-Deforming Particles," Z. Metallk. 55 (1964) 5.

12. J. J. Holmes, R. E. Robbins, and J. L. Brimhall, "Effect of Fast Irradiation on the Tensile Properties of 304 Stainless Steel," J. of N. Mat. 32 (1969) 330. (304 SS)

13. K. Matsumoto, T. Kataoka, M. Terasawa, M. Shimada, S. Nakahigashi, H. Sakoiri, and E. Yagi, "Embrittlement of Austenitic Stainless Steel Irradiated with a-Particles," J. of N. Mat. 67 (1977) 97. (316 SS)

14. A. W. Thompson, "Mechanical Behavior of Face-Centered Cubic Metals Containing Helium," Materials Science and Engineering 21 (1975) 41. (309S SS, 304L SS)

15. This facility: (316 SS)

16. P. S. Sklad, R. E. Clausing, and E. E. Bloom, "Effects of Neutron Irradiation on Microstructure and Mechanical Properties of Nimonic PE-16" in Radiation Effects on the Microstructure and Properties of Metals STP 611 (American Society for Testing and Materials, Philadelphia, 1976), 139. (PE-16)

17. R. D. Nicholson and R. B. Jones. "Fracture Toughness of Irradiated Nimonic PE 16 at High Temperatures" in Effects of Radiation on Structural Materials STP 683 (American Society for Testing and Materials, Philadelphia, 1978), 529.

18. J. A. Horton, Ph.D. Dissertation (January, 1980). (304 SS - neutron irradiated, 316 SS - helium irradiated)

19. D. E. Rawl, Jr., G. R. Cashey, Jr., and J. A. Donovan, "Low Temperature Helium Embrittlement of Tritium-Charged Stainless Steel," 190th AIME Meeting, Las Vegas, Nevada, February 24-28, 1980 (to be published in Metallurgical Transactions). (21-6-9 SS, 3041 SS)

20. M. I. de Vries, B. van der Schaaf, H. U. Staal, and J. D. Elen, "Effects of Neutron Irradiation and Fatigue on Ductility of Stainless Steel DIN 1.4948" in Effects of Radiation on Structural Materials STP 683 (American Society for Testing and Materials, Philadelphia, 1978), 477. (DIN 1.4943 SS)

21. E. E. Bloom and J. O. Stiegler, "Postirradiation Mechanical Properties of Types 304 and 304 + 0.15% Titanium Stainless Steel," Nuclear Technology 17 (January, 1972) 24. (304 SS)

22. M. Kangilaski, J. S. Perrin, and R. A. Wullaert, "Irradiation-Induced Embrittlement in Stainless Steel at Elevated Temperatures" in Irradiation Effects in Structural Alloys for Thermal and Fast Reactors STP 457 (American Society for Testing and Materials, York, Pennsylvania, 1969), 67. (347 SS) †bubble diameters and densities estimated from H. R. Brager and R. E. Robbins, "Stabilized Cavities in Irradiated Austenitic Stainless Steel," Transactions American Institute for Mining, Metallurgical and Petroleum Engineering, 242 (1968), 2010.

23. M. Weisz, J. Malkin, J. Erler, and J. P. Andre, "High-Temperature Embrittlement of AISI Type 316 Stainless Steels after Irradiation" in Irradiation Effects in Structural Alloys for Thermal and Fast Reactors STP 457 (American Society for Testing and Materials, York, Pennsylvania, 1969), 352. (316 SS) †bubble diameters and densities estimated from data from E. E. Bloom, J. O. Steigler, and C. J. McHargue, "Radiation Damage in Annealed Type 304 Stainless Steel," Radiation Effects 14 (1972) 231. (estimated from micrographs in the text)

24. A. A. Sagüés, H. Schroeder, W. Kesternich, and H. Ullmaier, "The Influence of Helium on the High-Temperature Mechanical Properties of an Austenitic Stainless Steel," J. of N. Mat. 78 (1978) 289. (DIN 1.4970 SS)

25. J. H. Evans, "An Intergranular Fracture Mechanism of Blister Formation on Helium Irradiated Metals," J. of N. Mat. 68 (1977) 129.

26. J. R. Cost and K. Y. Chen, "The Number of Gas Atoms per Bubble of Inert Gas in a Solid," J. of N. Mat. 67 (1977) 265.

27. R. L. Simons, "Helium Production in Fast Breeder Reactor Out-of-Core Structural Components" in Effects of Radiation on Structural Materials, ASTM STP 683, J. A. Sprague and D. Kramer, Eds., American Society for Testing and Materials, 1979, 365.

28. D. R. Harries, "Neutron Irradiation-Induced Embrittlement in Type 316 and Other Austenitic Steels and Alloys," J. of N. Mat. 82 (1979) 2.

29. I. 0. Smith and B. Russell, "The Dependence of the Tensile Properties of Irradiated Aluminum-Lithium Alloys Upon Gas Bubble Size and Distribution," J. of N. Mat. 37 (1970) 96.

30. P. J. Maziasz. "Precipitation Response of Austenitic Stainless Steel to Stimulated Fusion Irradiation" in The Metal Science of Stainless Steels, E. W. Collings and H. W. King, Eds., The Metal. Soc. of AIME (1979) 160.

31. J. A. Horton, HVEM Studies of Helium Embrittlement in Stainless Steel, Ph.D. dissertation, University of Virginia (1980).

32. D. F. Stein and L. A. Heldt, "Grain Boundary Segregation and Materials Properties" in Interfacial Segregation, W. C. Johnson and J. M. Blakely, Eds., American Society for Metals (1979) 239.

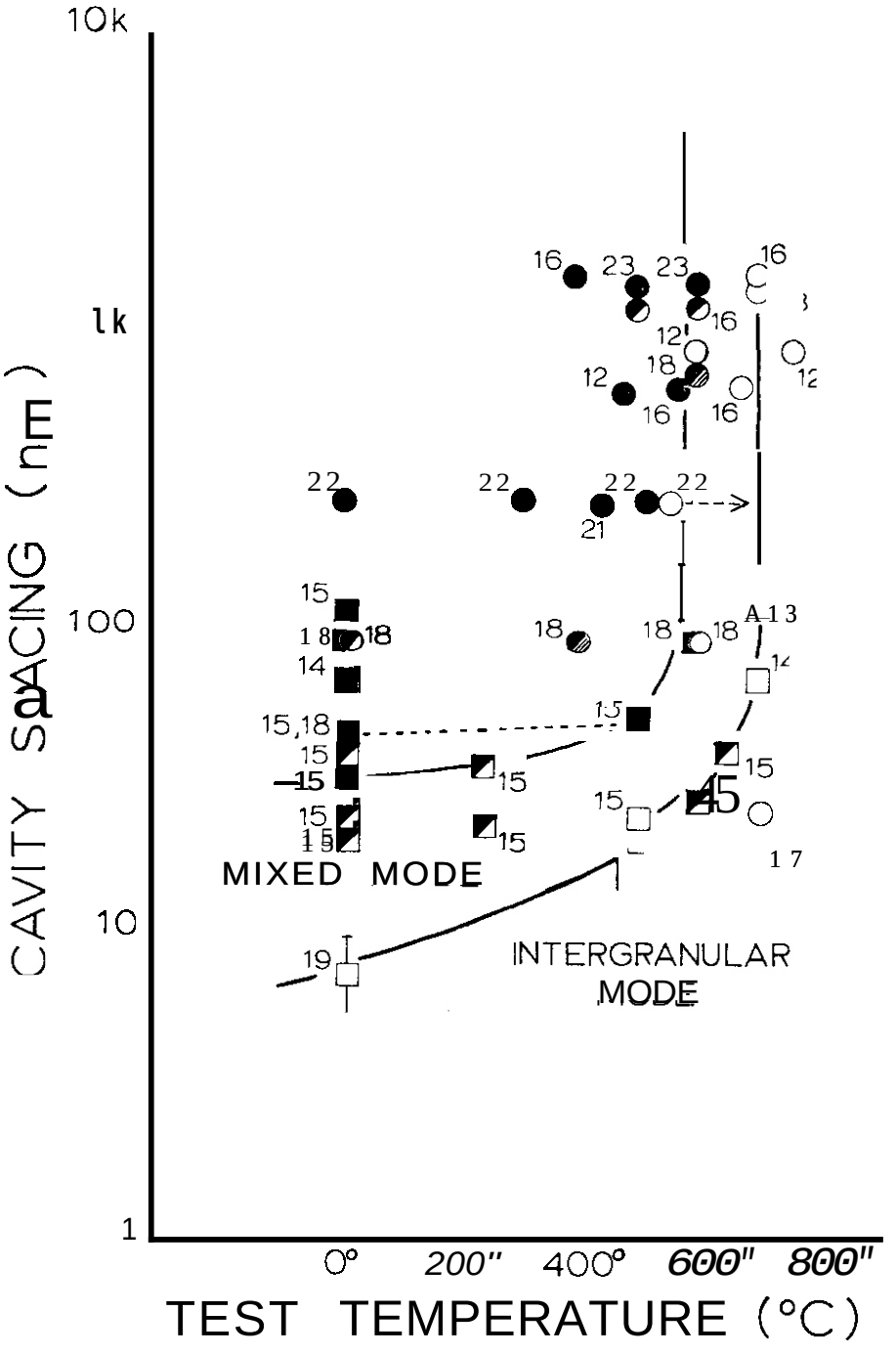

Figure 1: Plot of separation between cavity surfaces in austenitic stainless steel vs. tensile test temperature. Explanation of Symbols: 1. Type of Irradiation: circle-neutron, square-'+He ion or ^{3}He. 2. Type of Fracture: filled-transgranular, open-intergranular, half filled-mixed, crosshatched-channel.

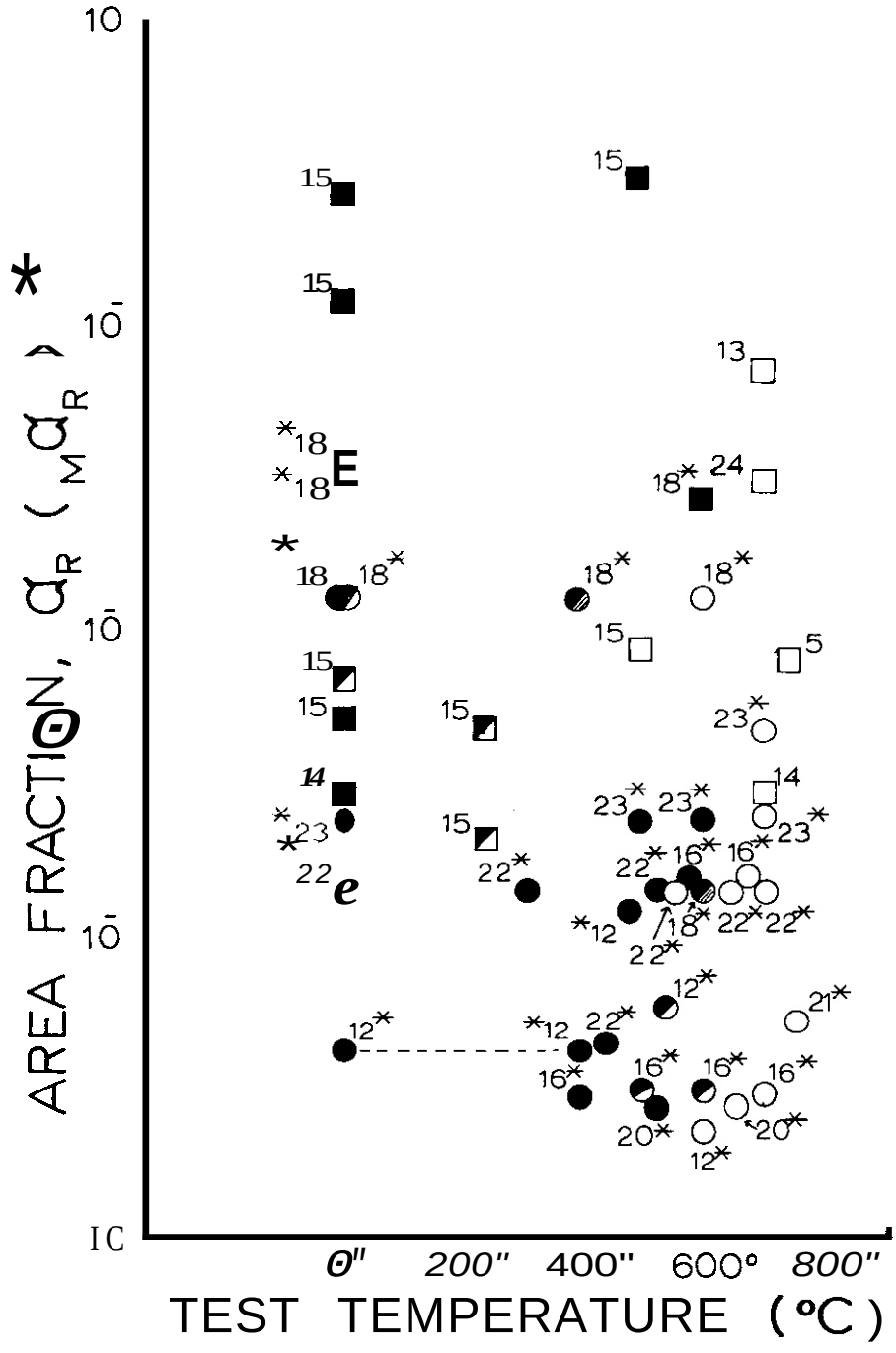

Figure 2: Plot of the area fraction, α_R, of grain boundaries in austenitic stainless steel occupied by bubbles, vs. tensile test temperature. * denotes area fraction, $_m\alpha_R$, of an arbitrary plane in the grain interior occupied by bubbles. See Figure 1 for an explanation of the symbols and the text for information about data points 5 and 24.

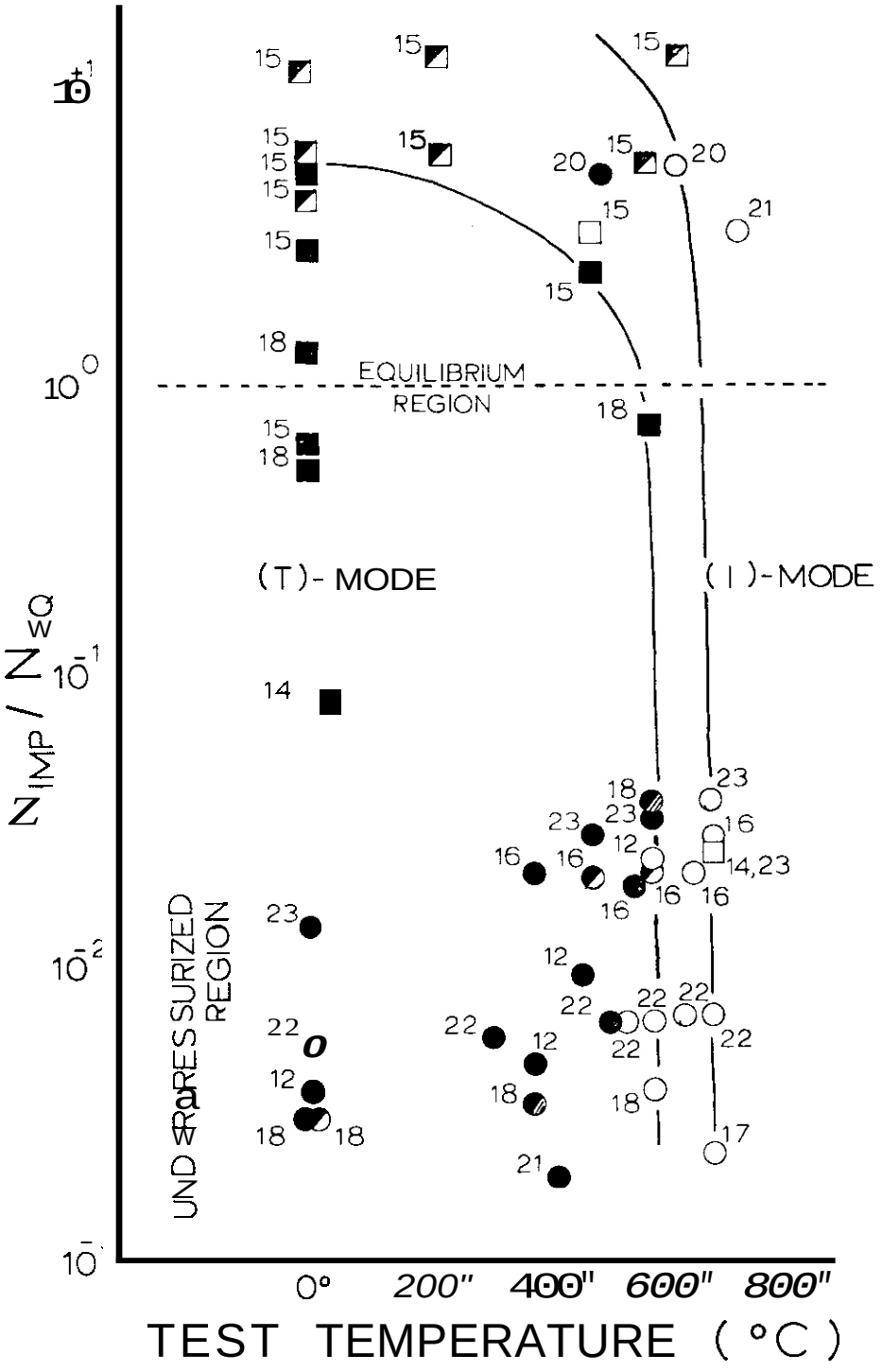

Figure 3: Plot of the estimated ratio (N_{imp}/N_{eq}) of the total number of helium atoms contained in an austenitic stainless steel specimen to the number of atoms that could be contained in equilibrium bubbles of diameter, d, and density, ρ, vs. tensile test temperature. For syinbol explanation, see Figure 1.

I. PROGRAM

Title: Damage Analysis and Fundamental Studies for Fusion Reactor Materials Development

Principal Investigators: G.R. Odette and G.E. Lucas

Affiliation: University of California, Santa Barbara

II OBJECTIVE

The objective of this work is to develop analytical and experimental procedures to correlate irradiation effects data taken in an array of irradiation environments and extrapolate materials behavior to the range of service conditions which will be encountered by structural components in fusion reactors.

III. RELEVANT DAFS PROGRAM TASK/SUBTASK

SUBTASK B Fundamental Mechanical Properties

SUBTASK C Correlation Methodology

IV. SUMMARY

An instrumented microhardness tester was designed, built and tested. Although components of the microhardness tester performed within their specifications, difficulties in referencing the specimen surface introduced an unacceptable level of uncertainty in the predicted stress-strain behavior of the sample. A second commercial microhardness tester was then modified to permit indentations with steel balls 1.59mm in diameter and less. This has produced satisfactory predictions of material stress-strain behavior in the strain range 1-10% from data taken at as few as two penetration locations per sample.

To complement the microhardness tests, two ductility test techniques were investigated; namely, a shear punch test and a bulge test. Preliminary results on a variety of sheet materials

indicate that both tests are promising for monitoring changes, especially reductions, in material ductility.

Work has also proceeded on the development of an indentation load relaxation test to assess time-dependent flow properties. Baseline creep, creep indentation, and load relaxation data have been generated; and investigations of specimen thickness effects are in progress.

Finally, work is in progress to develop small specimens and test techniques to determine the fracture resistance of materials.

V. ACCOMPLISHMENTS AND STATUS

Small Specimen Test Development - G.E. Lucas, G.R. Odette, W. Sheckherd, C. Pendleton, F. Haggag, M. Dooley, W. Server, P. McConnel (UCSB).

1. Introduction

Because of the limited irradiation volume in existing (RTNS-II) and near-term (FMIT) high energy neutron irradiation devices, it is necessary to develop test techniques to extract mechanical property information from small volume specimens. It is preferable to use specimens of a multipurpose geometry, such as TEM discs, to maximize irradiation capsule packing efficiencies; moreover, it is desirable to develop nondestructive or pseudo-nondestructive test techniques to permit periodic testing of a single specimen after intervals of irradiation or post-irradiation conditioning.

In keeping with this, a number of such test techniques are under development at the University of California, Santa Barbara. These include an instrumented microhardness test, a shear ductility test, a bulge ductility test, an indentation load relaxation test, and a variety of miniature test specimens to characterize fracture. The status of these test developments is reported here.

2. Instrumented Microhardness Test

As reported earlier [1], a procedure has been developed and tested on the macrohardness scale, whereby ball indentation depth as a function of applied load is measured *in situ* and these data are used in conjunction with a semi-empirical correlation to predict a segment of the uniaxial, tensile stress-strain curve for the sample material. Based on the macrohardness work, attempts have been in progress to scale the test down to the microhardness regime.

A prototype, instrumented microhardness apparatus was built to test the applicability of the macrohardness approach in the microhardness regime and to test the integrated response of a high-sensitivity LVDT-load cell configuration. A schematic of the apparatus is shown in Figure 1. The apparatus consists of a rigid steel frame on which a stage is mounted and through which a load application plunger penetrates. Loads can be applied to the load pan at the top of the plunger either by calibrated weights or by the active loading of a mechanical testing machine. At the tip of the plunger, hardened steel balls of various diameters (currently down to .25mm) can be attached. The plunger also features a collar for contacting the spring-loaded LVDT core arms. The stage attached to the frame consists of several components. The base is an XY travelling stage with an X and Y micrometer drum; each micrometer has positional resolution to 10^{-4} inch. Attached to the travelling stage is a 2-kg capacity load cell for measuring the real load on the specimen minus the force of the LVDT core springs. Resting in the load cell is the specimen stage. This contains a rosette of three miniature, spring-loaded LVDT's with a $\pm$ .125mm stroke and .25% linearity. The specimen rests at the center of this rosette. Finally, in conjunction with the design and operation of the instrumented microhardness testing, a full-sensitivity analysis was conducted of the parameters in the semi-empirical

correlation between the hardness load-displacement data and the tensile stress-strain behavior.

The components of the microhardness tester have all performed within their specifications. However, several important limitations of the original approach have been demonstrated by the operation of the tester itself and by the sensitivity analysis. The major problem with the tester has been referencing the sample surface; i.e., a surface datum is required from which plastic penetration depth can be measured. Attempts to reference the surface by contacting it with the penetrator under a small preload were unsuccessful. The preloads required to produce no plastic indent with small balls and low-strength materials were in many instances smaller than the resolution capability of the load cell (10g) and approaching the frictional forces of the apparatus. An alternate attempt was made to signal initial contact between the specimen and penetrator with an indicator lamp in a d.c. circuit in which the penetrator/sample served as a switch. Because of contact resistance effects, the surface could be referenced only to within $\pm 2 \times 10^{-5}$ inches, even using a high-sensitivity ammeter in place of the indicator lamp.

As determined from the sensitivity analysis, this level of uncertainty in referencing the specimen (or indent) surface precluded the prediction of stress-strain behavior below strains of approximately 3%, with an uncertainty in the predicted stress of less than 10%. That is, the semi-empirical correlation developed previously [1] is very sensitive to the uncertainty of plastic penetration depth h_p in the microhardness regime. The sensitivity analyses also showed that the correlation is fairly insensitive to such parameters as the elastic modulus of the ball and specimen and the penetrator ball size, and only moderately sensitive to the measured load W and chordal diameter d of the indent.

Consequently, it was decided to attempt direct measurement of d as a function of W instead of h_p as a function of W. A Wilson Tukon^{r} microhardness tester was modified to accept ball indenters

with diameters in the range .25mm to 1.5mm; and the specimen stage alignment was adjusted so that a repeated loading up to some maximum load at a single penetration location produced the same indent size d as a single penetration at that maximum load. As with most microhardness testers, d is measured with a filar eyepiece following load application. Although accumulating d-W data is somewhat more laborious than accumulating h_p-W data, the lower sensitivity of the correlation to uncertainties in d permit prediction of stress-strain behavior over a wider strain range. Using two ball sizes, a strain range of 1%-10% can be predicted. To illustrate this, Figure 2 is a plot of stress-strain data predicted from microhardness data taken with a 1.5mm and a .25mm ball size and compared to uniaxial tensile data for a cold-rolled SAE 1015 steel.

The ball-modified microhardness tester has been used to acquire microhardness data from TEM discs of several materials being irradiated in RTNS-II in the HEDL program; these are Ni, Cu, V, Nb, Ti, and an Fe-Cr-Ni ternary. Obtaining data from these samples has been straightforward. The only significant problems encountered have been as-fabricated surface roughness on some samples which has encumbered d measurements, and a lower indentation load limit of 100g. Below 100g, the predicted stress-strain data scatter becomes unacceptable. While sensitivity analyses indicate this may be in part a result of uncertainties in the measured value of d, tests on steel with an ASTM grain size 7 indicate that below 200g the ball penetrator intersects less than 3 grains at the surface. Consequently, grain size effects may provide a greater limitation than dimensional resolution capabilities.

Grain size effects are currently being investigated in the TEM disc materials as part of a task to establish standardized ball microhardness test procedures. In addition, the hardness data are to be compared to tensile data on these same materials as soon as these data are made available. Results will be reported in a future quarterly.

3. Ductility Tests

The instrumented hardness and ball-microhardness technique can provide a measure of such material flow properties as yield strength, strain hardening exponent, and ultimate tensile strength; and for some materials a measure of uniform ductility can be ascertained from the strain hardening exponent. However, no measure of total ductility (failure ductility) is obtained. Since failure ductility is a property of interest both as an engineering parameter and as a monitor of microstructural changes, test techniques are needed to provide a measure of failure ductility. Two such techniques, a shear punch test and a bulge test, have been investigated as complementary tests to microhardness.

The basis for the shear punch test is taken from sheet metal forming operations, [2,3] in which metal parts are separated by oppositely directed moving blades. For a punch (moving blade) moving into a sheet fixed within a die (stationary blade), the depth to which the punch must penetrate the die before complete material separation is proportional to the ductility of the material. Hence, instrumenting the punching apparatus to permit determination of the punch depth at fracture should provide a means of ascertaining material ductility.

One of the potential attractions of a shear punch test is that it may be made an integral part of irradiated specimen preparation in a materials evaluation program. Specifically, the punch may be machined as a 3mm diameter cylindrical punch, and hence TEM blanks may be the product of the test. This would render the test "productive" rather than destructive. However, it may be more desirable to perform the shear punch test on prefabricated specimens (e.g. TEM discs), and this has been kept in mind during the development of the test. Consequently, although the test has initially been developed on a fairly large scale, it may be scaled down to a size appropriate for the fusion materials program.

The apparatus constructed to test initially the concept of the shear punch test consists of a simple two-piece die and a ,250-inch diameter, flat cylindrical punch. A sheet metal sample is clamped firmly in the die, and the die is rigidly mounted to the fixed crosshead of a 20-kip MTS testing machine. The cylindrical punch is forced through a honed hole in the die, and thus through the sheet metal sample, by the hydraulically driven ram in the MTS. The force applied to the punch and the travel of the punch are monitored simultaneously on the MTS XY chart recorder.

Eight different .020" sheet materials - a yellow brass, a mild steel, and a stainless steel given different heat treatments - were tested in the shear punch apparatus as a scoping experiment. In addition, standard tensile tests (four each) were performed on each of the materials. Tensile properties are given in Table 1. A typical load-displacement curve generated in a shear punch test has all the features of a load-displacement curve generated in a standard tensile test: namely, an initial linear (elastic) regime; a non-linear, monotonically increasing (plastic work hardening) regime; a maximum (necking between the blade contacts); and a monotonically decreasing regime terminated by complete separation of the sample pieces. It was found that for the range of materials tested, these features of the punch load-displacement curve tracked corresponding features of the tensile load-displacement curve; for example, the maximum load in the punch test increased with the ultimate tensile strength of the test material, and as described below the displacement to failure in the punch test increased with the total ductility of the material. However, the area under the two types of curves (i.e. toughness) did not correlate as well.

Although more flow property information than just ductility may ultimately be gleaned from this test technique, it was initially evaluated on the basis of ductility alone. The shear punch plastic displacement to fracture was found to be the most useful feature of the test for this purpose; hence, it is compared to the total uniaxial tensile ductility of several materials in Figure 3.

A plot of shear punch plastic displacement to maximum load against material uniform elongation has similar features. Despite the sparsity of data, a definite empirical correlation can be seen to exist between punch displacement and material ductility. Moreover, from a solid physics standpoint the correlation should pass through the origin; that is, the punch plastic displacement to failure should be zero for a completely brittle material. Consequently, the punch displacement test should be very sensitive to ductility changes at low ductilities, a desirable situation for monitoring irradiation effects. However, the magnitude of this sensitivity is still uncertain with so few data.

As a result of these promising scoping experiments, the shear punch test is under continuing development. In particular, additional data are being added to the empirical correlation, theoretical (finite difference/finite element) analyses of shear punch test specimen deformation are planned, and considerations are being made to scale the test down to smaller specimen sizes.

The other ductility test which has been investigated is the bulge test. Again the basis for this test has been taken from sheet metal forming operations and testing [3-7]. The theory behind the test is relatively straightforward. By stretching a thin metal sheet over a spherical (or hemispherical) punch and lubricating the punch/sheet interface, a uniform pressure builds up between the punch and sheet. This in turn produces a state of balanced biaxial stress in the stretched sheet (in practice this is best approximated at the center of the sheet). Failure then proceeds under biaxial conditions, which in theory can be related to uniaxial failure. In any event, the strain to failure provides a measure of material ductility which in turn should be sensitive to microstructure. The advantage of this technique over the shear punch test is the simpler stress state produced near the fracture zone, which facilitates analysis; as a consequence of this a greater literature exists for biaxial failure ductility of metals.

The apparatus constructed to test this approach also consists of a simple two-piece die. Again a sheet metal sample is clamped between the die halves; however, the hole into which the material deforms is tapered to prevent failure at the fixed-position boundary. The die is mounted rigidly to the fixed crosshead of a 20 kip MTS testing machine; and a punch with a 0.5 inch diameter steel ball fixed to its end, is forced along a guide hole and into the test sheet by the MTS ram. The sheet then stretches over the ball and deforms into the tapered hole until it fails. A follower sheet of neoprene between the ball and the specimen was found to reduce interfacial friction and promote failure at the center of the sheet.

The amplified specimen compliance of this test precluded the use of the punch load-displacement curve to obtain mechanical property data on the specimen alone. Instead, a square grid of 0.002-inch-thick lines with a .010-inch spacing was placed on each specimen by a photo-etching - bluing technique specially developed for this test. Grid dimensions were then measured with a filar-eyepiece microscope. By comparing grid dimensions at the crack site before and after deformation, specimen strain to failure could thus be measured directly.

Again the materials described in Table 1 were tested by this technique. The grid was found to deform isotropically near the center of the bulge — i.e., the strains in the two principal grid directions were equal ($\varepsilon_1 = \varepsilon_2$) -- and the crack initiated and propagated from the center. The principal strains to failure ($\varepsilon_1^f = \varepsilon_2^f$) in each test were determined from grid measurements around the fracture initiation site. These data are plotted against the uniaxial tensile uniform strain (ε_U) for each material in Figure 4. Data extracted from curves reported by Keeler and Backofen [4] for similar tests are also shown in Figure 4. As can be seen, with the exception of annealed steel, the two data sets are in relatively good agreement with one another. Moreover, there is a systematic trend in the data. The bulge ductility is greater than or equal to

the uniform tensile ductility in all cases; and like the shear punch results, the bulge ductility is very sensitive to the uniform tensile ductility when the latter is small. A similar relationship was found between the biaxial and uniaxial fracture ductilities.

The difference in uniaxial and multiaxial ductilities is well documented and is the basis for the forming limit diagram in the sheet metal industry. [5] Moreover, the relationship between uniaxial and multiaxial ductilities has been a classic problem in plasticity theory. [7] And while some analytical relations correlate some data well, a general solution is still not in hand.

Nonetheless, an empirical relation between the ductilities is obvious; consequently, biaxial ductility can serve as well as uniaxial ductility as a radiation damage monitor. Moreover, a multiaxial ductility may be of more engineering significance than a uniaxial ductility. Finally, recent finite-element work has permitted considerable progress in developing a fundamental understanding of stress state effects on material ductility. [8] Consequently, work is ongoing to further the development of the bulge test. In particular, finite element modeling of the bulge deformation process is in progress, and plans for scaling down the specimen sire are being formulated.

4. Indentation Load Relaxation Tests

The instrumented microhardness test and the ductility tests described above can provide time-independent flow property information. However, time-dependent flow property information will also be useful from a viewpoint of monitoring both mechanical property and microstructural changes in a material during irradiation. Consequently, development of an indentation load relaxation test is under development to provide this time-dependent information.

The time-dependence of hardness at elevated temperatures (hot-hardness) has received considerable attention. [9-12] In addition, some work has been performed on indentation creep, the

time-dependent penetration of a material by a cylindrical punch; indentation creep results have been correlated with standard material creep properties.[13] However, a test which may have some advantages over the indentation creep for small specimen testing is an indentation load relaxation test. In contrast to standard creep tests, standard load-relaxation tests can provide a description of inelastic strain rate over a considerable stress range for a single test. Hence, it would seem by analogy that an indentation load relaxation test may provide considerably more time-dependent flow property data from a single penetration location than an indentation creep test.

An apparatus has been constructed to conduct both creep indentation and indentation load relaxation tests. The apparatus consists of a cage, which transmits a tensile load applied to its end plates as a compressive load between its two stage platens. The test specimen is mounted on the lower platen, and a cylindrical punch of variable diameter is fixed to the upper platen. A mechanical-electrical extensometer attached to the upper and lower platens monitors the punch displacement relative to the specimen surface; and, if desirable, a load cell can be placed in series with the load train to monitor load. The cage assembly can thus be used in either a standard creep frame or tensile testing machine.

Currently, an extensive test program is being performed on lead samples, since lead creeps readily at room temperature and room temperature testing precludes many testing difficulties. Standard tensile, creep and load relaxation tests have been performed to acquire baseline data. And both creep indentation and indentation load relaxation tests are currently being performed. Attempts will be made to correlate the data by equation-of-state and other techniques. In addition, specimen thickness effects are being evaluated empirically and analytically. Results will be reported in a future quarterly progress report.

5. Miniature Fracture Samples

A number of studies have been initiated on miniature fracture samples. Slow bend tests have been conducted on .5T, .2T and .1T bend bars *of* an A302B pressure vessel steel (for which considerable fracture toughness data have previously been generated [14]), and multiple specimen R-curves are being generated from the data. In addition, a program is being conducted on these sample geometries in which samples are bent to small fractions of the maximum load displacement, fractured at liquid nitrogen temperatures, and examined by SEM for evidence of microinitiation. The intent is to correlate microinitiation in large and small samples, and to use that information in calibrating a correlation model of fracture behavior. Results will be provided in a future quarterly.

In a related program, currently funded by EPRI, miniature Charpy V-notch specimens (1/3 standard dimensions) are being developed and tested to provide a means of tracking NDTT shifts in irradiated ferrous materials. Preliminary tests indicate that from these small samples a Charpy curve can be generated which looks much like one generated with standard Charpy specimens. A set of example curves for an A302B pressure vessel steel are shown in Figure 5; E is the measured impact energy, B the specimen width (10mm for CVN, 3.3mm for mini-CVN) and b is the ligament size (8mm for CVN and 2.64mm for mini-CVN). Again data are few and preliminary at this time, and will be reported in more detail in the future.

VI. REFERENCES

1. G.E. Lucas. et al., "Development of Instrumented Hardness Techniques," OAFS-QPR #5, DOE/ET-0065/5 (1979) 199.

2. G.E. Dieter, Mechanical Metallurgy, McGraw-Hill, New York (1976).

3. W.A. Backofen, Deformation Processing, Addison-Wesley, Reading, Mass. (1972).

4. S.P. Keeler and W.A. Backofen, Trans. ASM, 56 (1965) 25.

5. V.V. Hasek, "An Evaluation of the Applicability of Theoretical Analyses to the forming Limit Diagram," Fracture 1977, 2, ICF4, Waterloo, Canada (1977) 475.

6. S. Levy, et al., "Analysis of Sheet Metal Forming to Axisymmetric Shapes," ASTM-STP-647 (1978) 238.

7. A.S. Korhonen, J. Eng. Metls. and Tech., 100 (1978) 303.

8. V. Nagpal, et al., AFML-TR-79-4168 (1979).

9. F. Hargreaves, J. Inst. Metals, 39 (1928) 301.

10. E. Underwood, J. Inst. Metals, 88 (1960) 266.

11. T.O. Mulhearn and D. Tabor, J. Inst. Metals, 89 (1960) 7.

12. J. Gofferd and K. Whaler, Trans. Met. Soc. AIME, 215 (1964) 613.

13. S. Chu and J. Li, J. Mat. Sci., 12 (1977) 2200.

14. W. Server, W. Oldfield, "Nuclear Pressure Vessel Steel Data Base," EPRI-NP-933, Electric Power Research Institute (1978).

VII. FUTURE WORK

Work will continue on small specimen test development as indicated previously. Standardized ball-microhardness test procedures for TEM disc specimens are currently being investigated with unirradiated materials used in the RTNS-II program. Finite element and analytic models are being used to correlate uniaxial and multiaxial ductilities. Creep indentation tests and indentation load relaxation tests on lead will be completed shortly;

data correlation is already in progress. Finally, developmental work on miniature bend bars and Charpy specimens will continue.

VIII. PUBLICATIONS

1. P. Au, G.E. Lucas, W. Sheckherd, G.R. Odette, "Flow Property Measurements from Instrumental Hardness Tests," Proc. of the Third Int'l. Conference on Nondestructive Evaluation in the Nuclear Industry, ANS-ASM-ASNDT-INMM-ISIJ-GSNT, Salt Lake City, Utah (1980).

Table 1

Ductility Test Specimen Tensile Properties

Material Designation	0.2% Offset Yield Strength (ksi)	UTS (ksi)	Uniform Elongation (%)	Total Elongation (%)
BAR	44 ± 2	56 ± 1	23 ± 3	26 ± 4
BA1	37 ± 1	51 ± 2	20 ± 4	*
BA2	32 ± 2	52 ± 2	25 ± 2	*
SAR	106 ± 1	108 ± 1	.5 ± .05	1.7 ± 1
SA1	45 ± 1	51 ± 1	23 ± 2	33 ± 3
SA2	40 ± 2	47 ± 2	29 ± 1	40 ± 1
SSAR	161 ± 1	178 ± 2	1.5 ± .05	4.0 ± 5
SSA1	170 ± 4	185 ± 3	1.2 ± .05	3.0 ± .5

* Necking and fracture outside clip gage

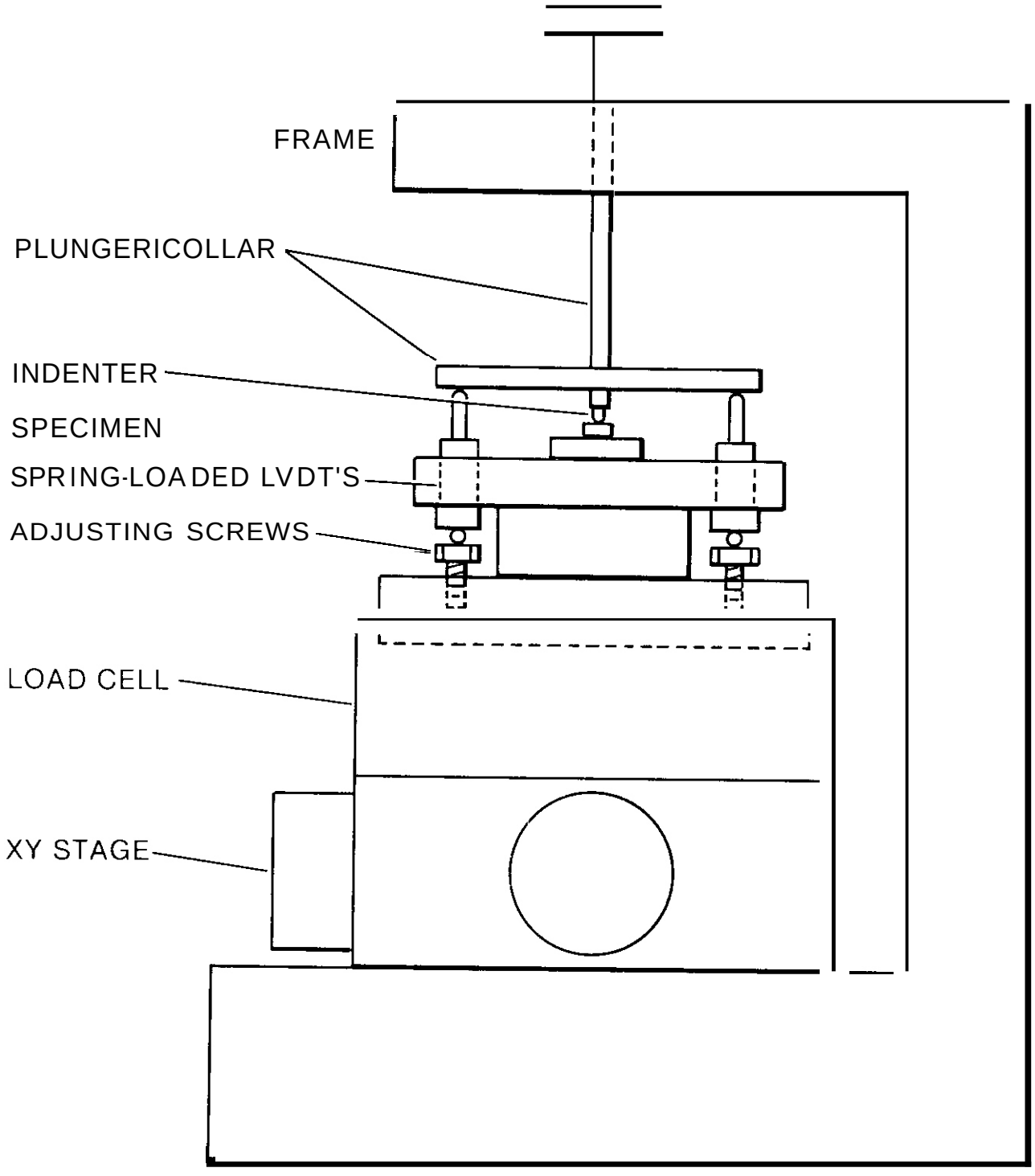

Figure 1. Schematic Diagram of Instrumented Microhardness Test Apparatus.

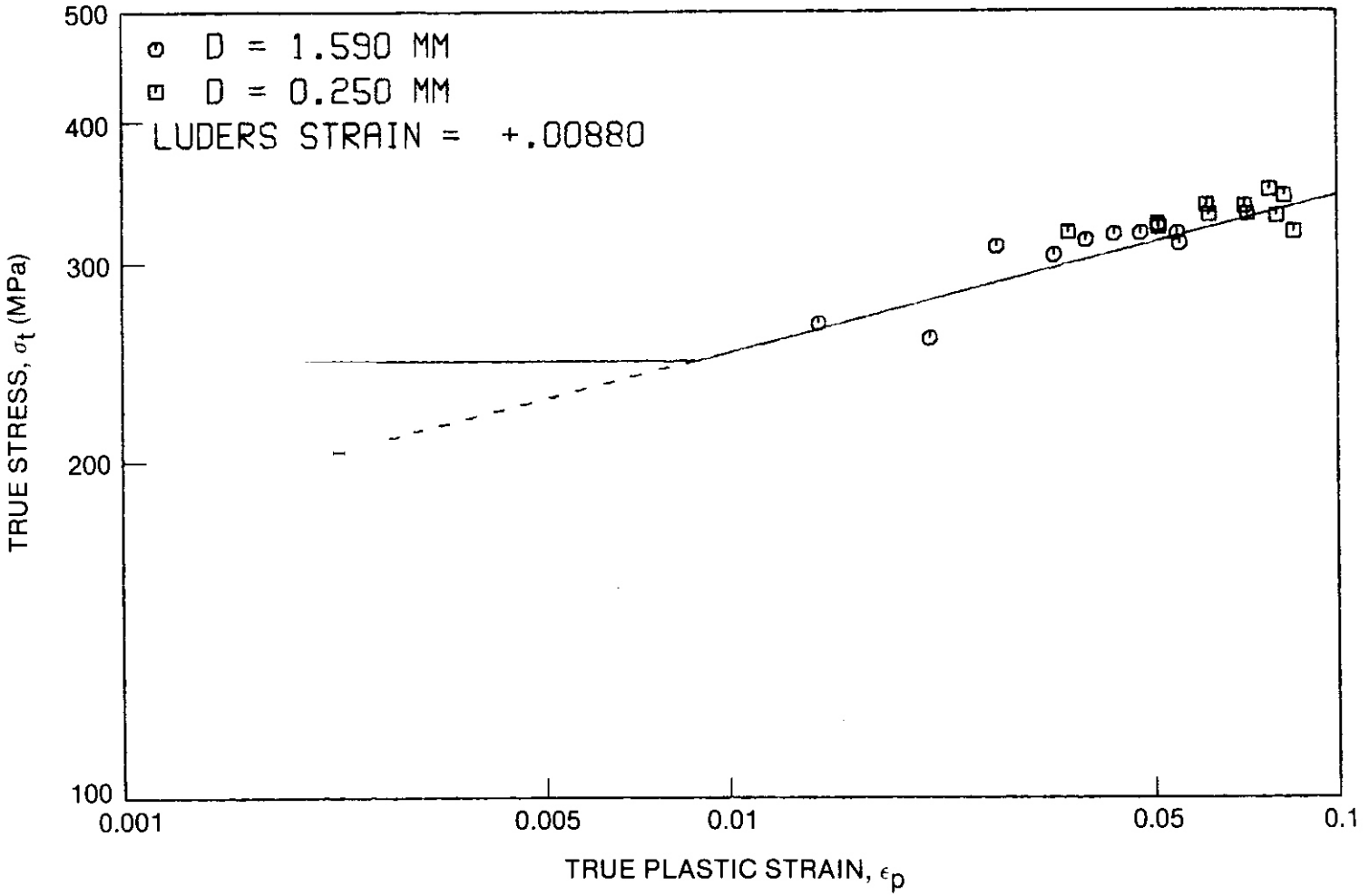

Figure 2 Comparison of Stress-Strain Data Derived From Ball Microhardness Tests with Tensile Stress-Strain Curve for a Cold-Rolled SAE 1015 Steel.

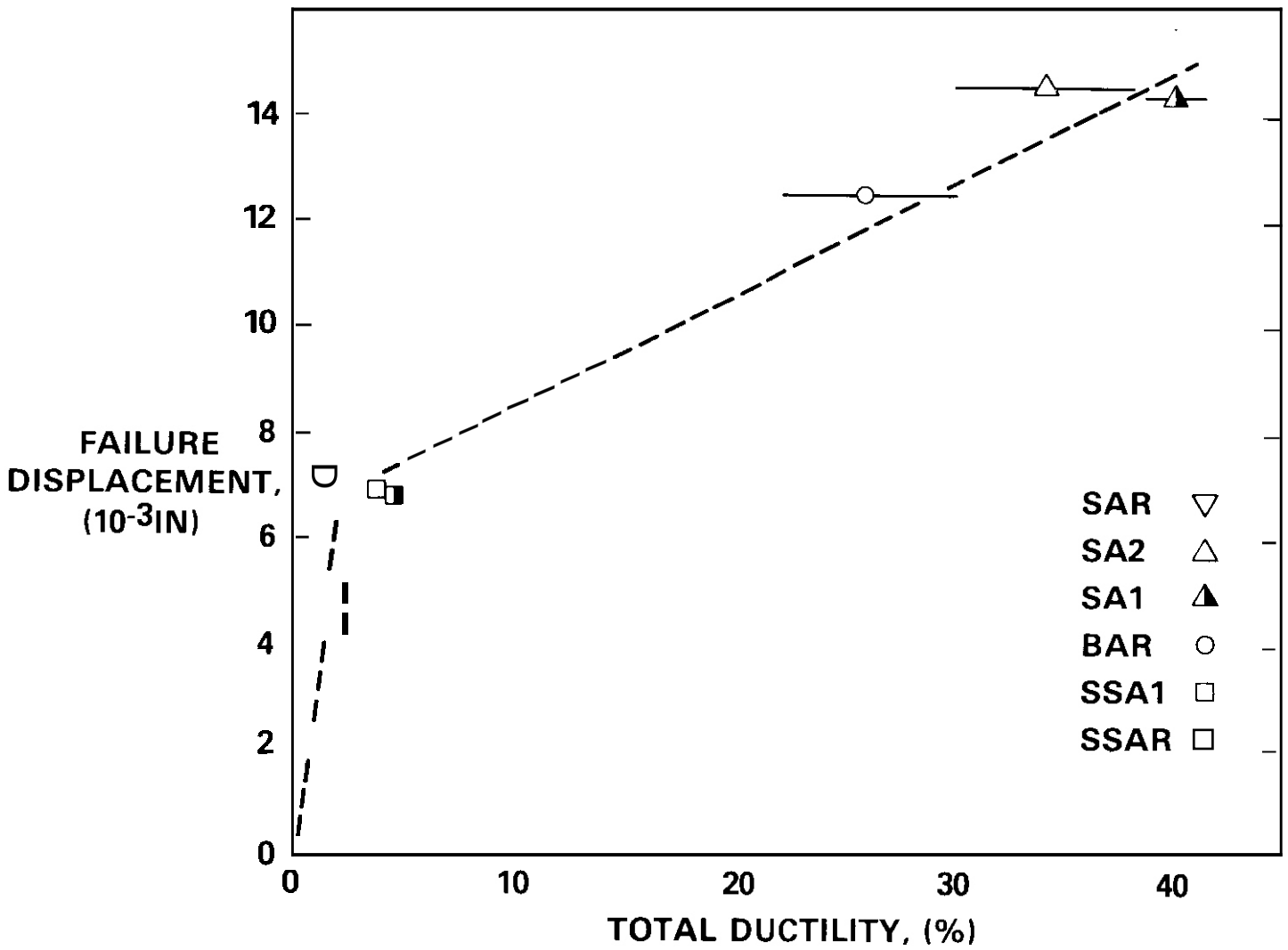

Figure 3. Variation of Shear Punch Displacement to Failure with Material Failure Ductility.

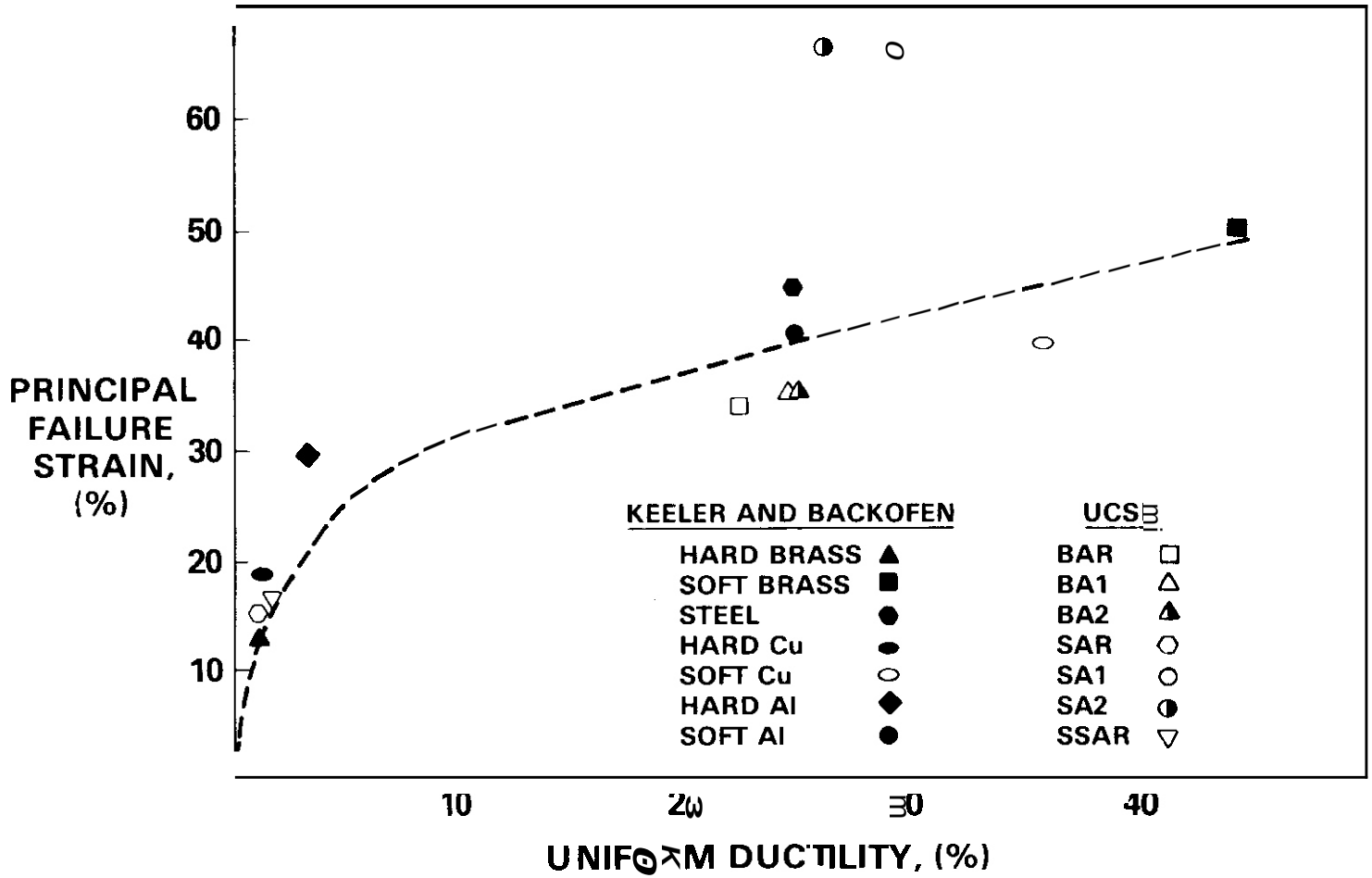

Figure 4 Variation of Material Uniform Ductility with Bulge Strain to Failure

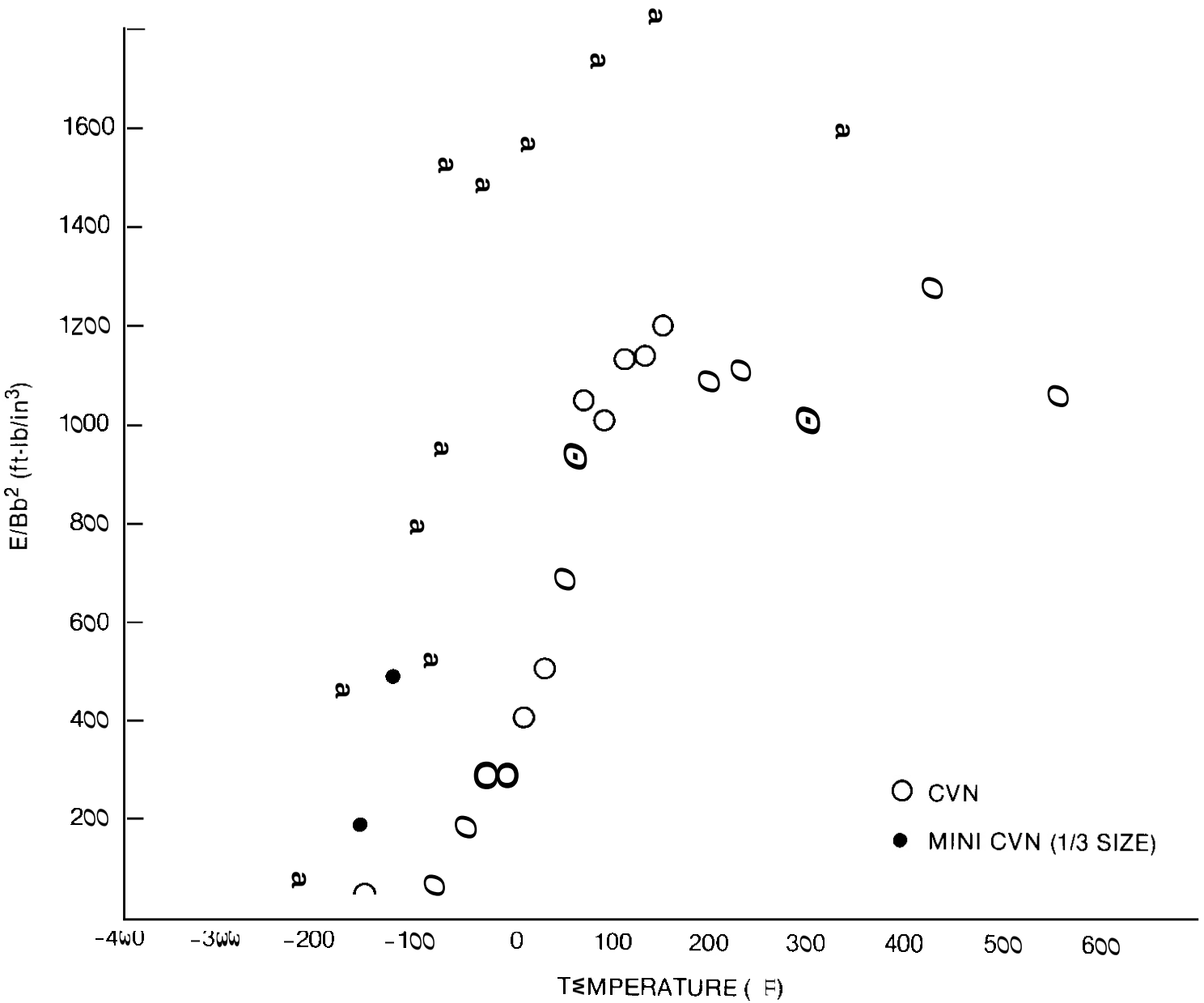

Figure 5. Comparison of Impact Energies Obtained with Standard and Miniature CVN Specimens for A302B Steel (EPRI Heat 4 A, Transverse Orientation).

I. PROGRAM

Title: Mechanical Properties
Principal Investigator: R. H. Jones
Affiliation: Pacific Northwest Laboratory

II. OBJECTIVE

1. Compare the leak rate of helium through small cracks in 316 SS stress rupture specimens to that predicted by gas flow theory using measured crack geometries.
2. Assess the importance of such cracking on a tokamak fusion reactor and the ability of nondestructive analysis techniques to identify and locate these microcracks in a vacuum first wall.

III. RELEVANT DAFS AND ADIP TASKS/SUBTASKS

DAFS	II.C.8	Effects of Helium and Displacements on Fracture
	II.C.12	Effects of Cycling on Flow and Fracture
ADIP	1.A.2.3	Develop Test Approaches and Test Matrices for Obtaining Critical Property Data
	1.B.9	Stress-Rupture Properties of Austenitic Alloys

IV. SUMMARY

Thin-walled 316 SS stress rupture specimens with through wall microcracks have been characterized using scanning electron microscopy and optical metallography. Using the measured crack dimensions, the leak rate was predicted using both viscous and molecular gas flow theories and found to be in good agreement with the measured leak rate. If the critical amount of helium necessary to contaminate a tokamak reactor is assumed to be on the order of 50% of the deuterium and tritium concentration in the plasma, then the critical crack dimensions can be estimated from gas flow theory. The results of this analysis show that through wall microcracks less than 100 microns in size may be sufficient to cause plasma contamination and

reactor shutdown. Such microcracks are similar to those observed after stress rupture tests.

V. ACCOMPLISHMENTS AND STATUS

A. Critical Flaw Size Determination - S. M. Bruemmer

1. Introduction

Plasma contamination by impurities may be a primary limitation in the useful operation of tokamak fusion reactors. Integrity of the vacuum first wall is critical since it separates the magnetically confined plasma from the liquid or gaseous coolant. This boundary must remain structurally sound under the radiation and chemical environment which will be aggravated by cyclic stresses and temperatures accompanying the reactor burn-refueling cycle. Failure of this vacuum boundary may result from small, through wall cracks which allow the leakage of a sufficient amount of coolant to contaminate the plasma during the period of one burn cycle.

2. Experimental Details

Small, through wall cracks in 316 SS tube were obtained from stress rupture tests at 650°C in PNL's helium gas loop. These stress rupture experiments are being conducted for DOE as part of the Gas-Cooled Fast Reactor program. The test specimens are thin-walled (0.5-mm) 316 SS tube with a volume displacement pin to minimize the volume of the internal pressurization gas (He) and thus limit any crack propagation after the initial failure. Leak rate measurements were made by encapsulating the specimen and monitoring the external pressure increase with a baratron over a range of internal pressures at room temperature. The external and internal surfaces were then examined using scanning electron microscopy, the major cracks identified, and through wall cracks characterized by optical metallography.

3. Crack Characterization and Leak Rate Correlation

Through wall cracks in two stress rupture specimens were examined. The outer (OD) surface of the tube exhibited several cracks localized in a single area while the interior (ID) surface had a high density of small cracks covering most of the ID surface of the tube (Figure 1). In order to estimate the effective crack dimensions controlling the leak rate, the major cracks on the OD surface were measured through the wall using optical metallography. An example of this is shown in Figure 2a-2C for several depths through the wall. The minimum crack dimensions were estimated from this analysis and are listed in Table I along with the measured and predicted leak rate of helium. The predicted leak rate was calculated from equations for the flow of gases through orifices by inputting the observed crack geometries. The crack length was taken to be slightly larger than the tube width (~15%) due to the tortuous crack path as illustrated schematically in Figure 2d.

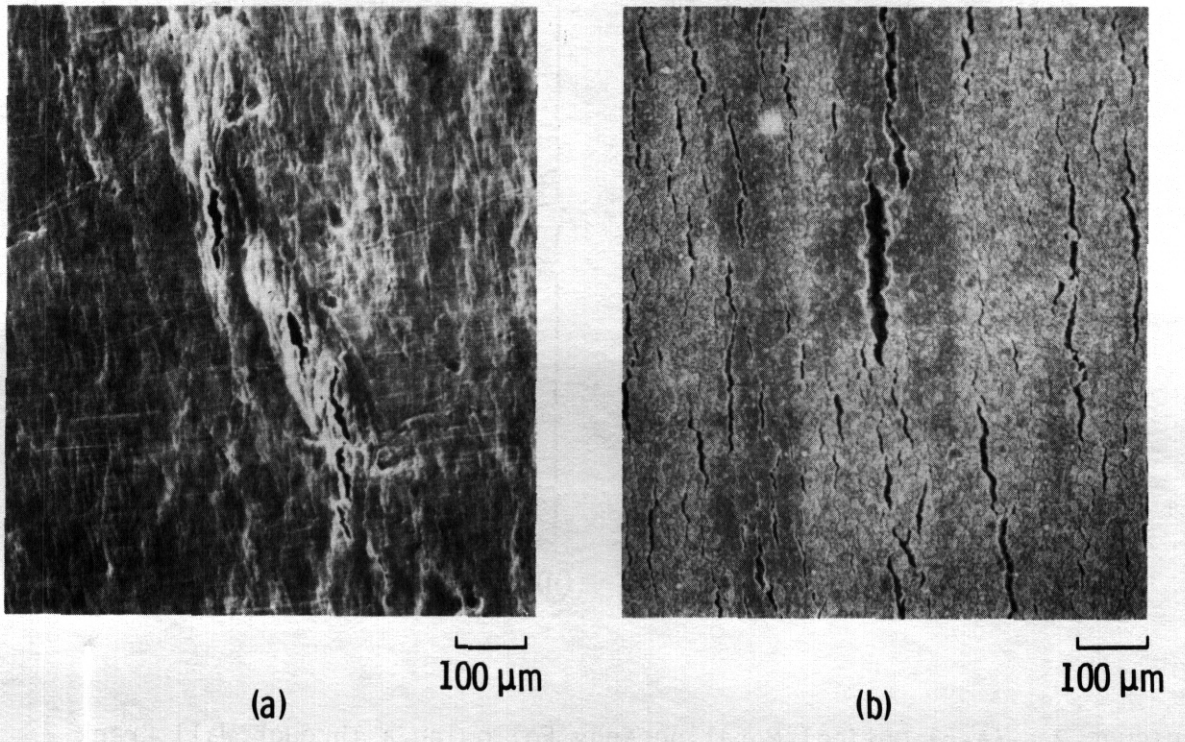

FIGURE 1. Scanning Electron Micrographs of (a) OD Surface and (b) ID Surface at Region of Through Wall Cracks (100 X)

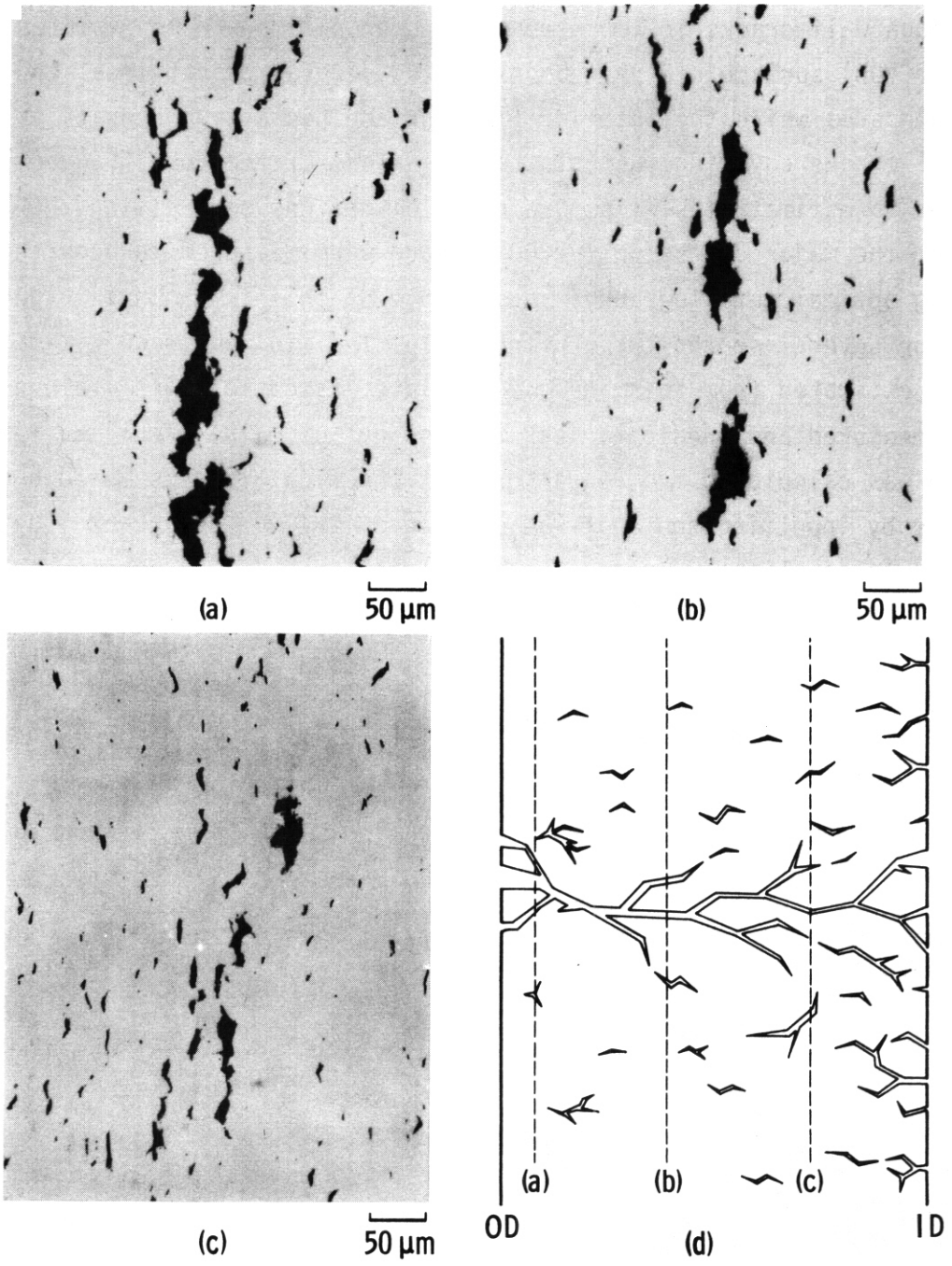

FIGURE 2. (a-c) Optical Metallography Following a Through Wall Crack Through Stress Rupture Specimen S-23; (d) Schematic Illustrating the Cracking Path Through the Thin Wall Tube

TABLE 1. Leak Rate Correlation: Prediction vs. Experiment

Specimen	Crack Dimensions (μm) Length	Width	Opening	Calculated Leak Rate (moles He/sec) Viscous Flow	Molecular Flow	Measured Leak Rate (moles He/sec)
S-23	290	100	15	5.5×10^{-6}	1.3×10^{-6}	$0.8\text{-}1 \times 10^{-6}$
S-4	290	190	35	1.1×10^{-4}	1.3×10^{-5}	$0.7\text{-}1.5 \times 10^{-4}$

The leak rate was calculated for conditions of viscous flow where the mean free path of the gas is controlled by intermolecular collisions with the crack walls.* Viscous flow will predominate on the coolant side of the wall while molecular flow may occur at the vacuum side of the crack; however, it is expected that viscous flow will dominate the leak rate of helium through a crack in a vacuum first wall. For the conditions of this study, the predicted leak rates are in approximate agreement with that obtained experimentally considering the undertainties in the crack dimensions. It is interesting to note that viscous flow theory more accurately predicts the leak rate for Samples S-4 with the larger crack size while the converse is true for the molecular flow theory. However, although consistent, it may only be fortuitous since only two specimens were examined. In general, gas flow theory does appear to give a reasonable indication of the through wall leak rate if the crack dimensions are known.

---

* The equations used to calculate the flow rate were:

for viscous flow

$$Q = 0.26\ Y\ \frac{a^2 b^2}{\ell}\left(\frac{P_1 + P_2}{2}\right)(P_2 - P_1)\text{, torr-liters/sec}$$

where Q is the flow rate and Y is a function of a/b. The remaining variables are defined in Figure 3.

for molecular flow

$$Q = 2/3\ \frac{a^2 b^2}{(a+b)\ell}\ (T/M)^{1/2}(P_2 - P_1)\text{, torr-liters/sec}$$

where T is the temperature in °K and M is the molecular weight of the gas.

4. Application to an Operating Fusion Reactor

4.1 Critical Crack Size

A critical crack in the vacuum first wall of a tokamak reactor may be defined as one which allows a critical amount of coolant to enter and contaminate the plasma during the period of a single burn cycle. For the purposes of this study, this critical amount (of helium) is arbitrarily selected as being 50% of the deuterium and tritium concentration in the plasma. Since this defines the critical leak rate, the crack dimensions can be calculated using gas flow theory. The results of this prediction is shown in Figure 3. The through wall crack is assumed to be similar to the test specimens of this study with a crack length of 1.15 times the vacuum wall thickness (0.254 cm) and a crack opening of 15 μm or 35 μm. If a long burn period is employed (5,000 sec), the critical crack size for a single through wall crack would be on the order of 60 μm x 35 μm or 300 μm x 15 μm (considering viscous flow). Such cracks are comparable to those shown in Figures 1 and 2, which were produced by stress rupture tests at 650°C. It is possible that similar cracks may form readily under the cyclic stress or temperature conditions of the first wall. These cracks are extremely small and may be difficult to detect for repair work.

VI. REFERENCES

None.

VII. FUTURE WORK

The present work was completed using discretionary funds. No additional tests are planned within the existing program. The possibility of future work in this area in cooperation with non-destructive analysis researchers is being investigated.

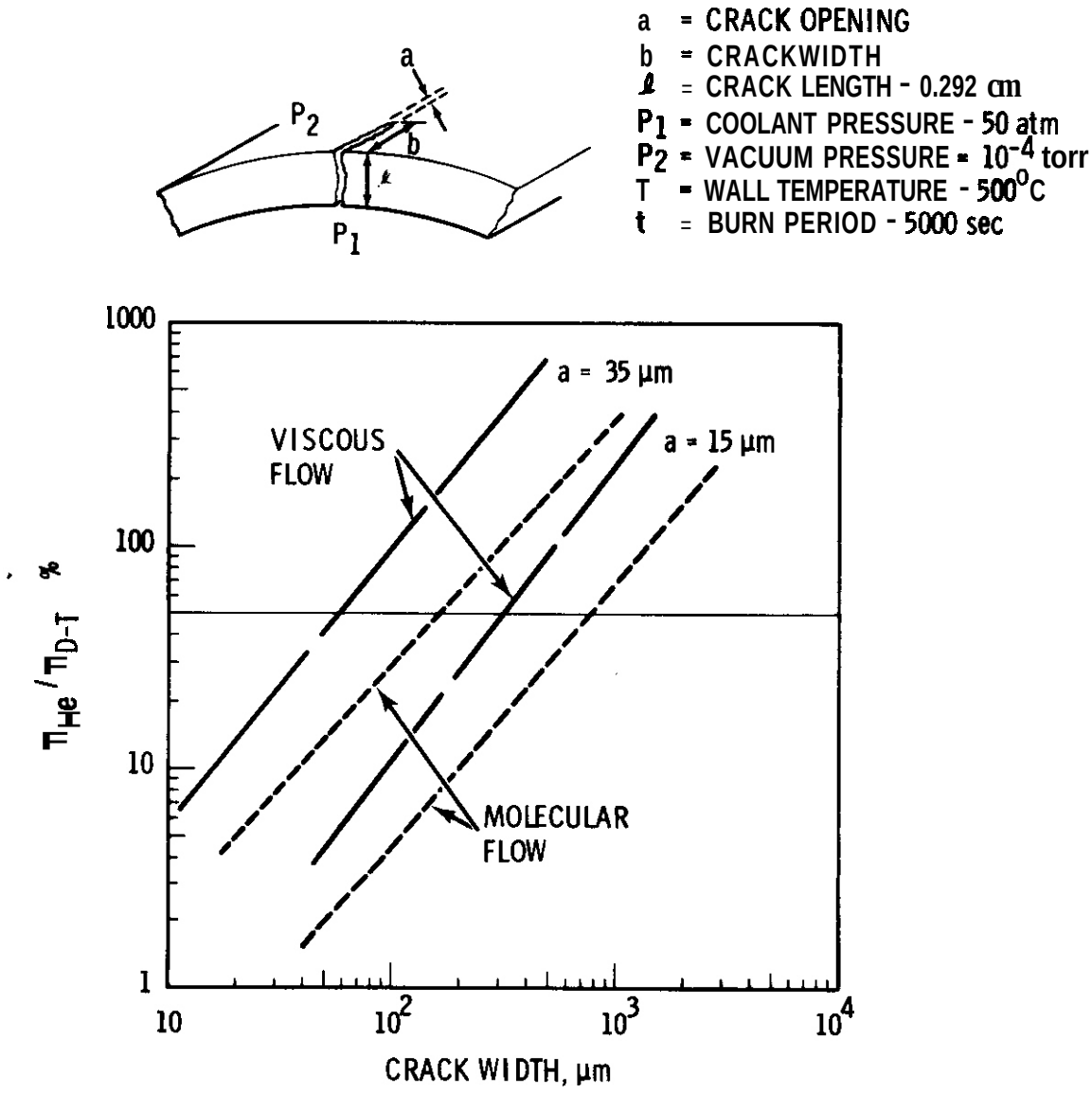

FIGURE 3. Predicted Helium Accumulation in the Plasma as a Function of the Through Wall Crack Width for Viscous and Molecular Flow for Two Crack Openings

CHAPTER 4

CORRELATION METHODOLOGY

I. PROGRAM

Title: Irradiation Response of Materials

Principal Investigators: S. Wood, J. A. Spitznagel and W. J. Choyke

Affiliation: Westinghouse Research and Development Center

II. OBJECTIVE

The objective of this work is to assess the phenomenology and mechanisms of microstructural evolution in materials exposed to simultaneous helium injection and creation of atomic displacement damage by a second ion beam.

III. RELEVANT DAFS PROGRAM TASK/SUBTASK

SUBTASK II.C.1, II.C.2, II.C.3, II.C.5, II.C.9, II.C.18

IV. SUMMARY

Conparison *of* cavity microstructures for pre- and post-anneal dual ion bombarded specimens of Ti-modified 316 SS suggests that this material could have gosd microstructural stability if subjected to thermal spikes during reactor operation. A second set of dual ion experiments on aged 316 SS has been completed and specimen evaluation is in progress. Preliminary results indicate qualitative agreement with previous data.

V. ACCOMPLISHMENTS AND STATUS

A. Annealing Experiments on Ti-Modified 316 SS

The Ti-modified austenitic SS are of particular interest for fusion applications because of the precipitation of the MC carbide phase and concommitant reduction in swelling which can occur during irradiation[1,2]. A further question arises concerning the stability *of* cavity microstructures

in this type of material during a thermal spike in the reactor cycle. With this in mind, some annealing studies have been initiated to investigate the changes in cavity size and other microstructural components compared to the as-bombarded condition. Figures 1 and 2 show TEM micrographs obtained from two specimens originally bombarded with the dual ion beams at 600°C to ~2.5 dpa and an appm He/dpa ratio of 70:1 utilizing damage rates of ~2.4 x 10^{-5} dpa/s and ~10^{-4} dpa/s, respectively. The lower damage rate specimen was subsequently annealed at 900°C for 0.5h while the other was annealed at the same temperature for 2h.

In the as-bombarded state, both samples exhibited a fairly low number density of several hundred angstrom cavities (Figures 1a and 2a) with a dislocation structure which contained a large faulted loop component (Figures 1b and 2b). There was no evidence of significant MC precipitation, but the relatively low swelling leads one to suspect that some localized helium trapping mechanism is operative and that small MC clusters may be present. After annealing, it is apparent that shrinkage of the original cavities and precipitation of coarse carbide ($M_{23}C_6$) have occurred in both specimens (Figures 1c and 2c). Furthermore, the visible cavity number density has increased, suggesting growth of non-visible bubbles present in the as-bombarded material. The principal change in the dislocation structure (Figures 1d and 2d) is the absence of faulted loops due to loop growth and unfaulting during the anneal. There is some evidence for MC precipitation during annealing (Figure 2d, in particular), but additional dark field microscopy is in progress to further elucidate this point.

A most important result of this preliminary annealing experiment is that, contrary to post-bombardment annealing effects observed in 304 SS(3), the overall size of the cavities in this Ti-modified 316 SS was reduced by the post-bombardment thermal treatment. This suggests that the material should show good microstructural stability, with respect to possible thermal fluctuations, in the anticipated fusion environment. Quantification of the cavity microstructures observed before and after the anneal is in progress.

B. Continuation of Dual-Ion Experiments on Aged 316 SS

A second set of aged 316 SS specimens were obtained from Argonne National Laboratory for dual-ion bombardment at the High Energy Ion Bombardment Facility at the University of Pittsburgh. This material, from the MFE heat, was given a 50% cold reduction, recrystallized by annealing at 1050°C for 0.5h and subsequently aged at 800°C for 10h at ANL. The primary objectives of the experiments are to evaluate the effects of aging and intergranular face-centered cubic Cr-rich carbide ($M_{23}C_6$) particles on microstructural evolution, and to compare microstructural results with those from similar experiments performed at ANL and Pacific Northwest Laboratory (in addition to the first data set obtained at HEIBS).

Oual bombardments were performed at 600, 650 and 700°C (±2°C) with an appm He to dpa ratio of 15:1 and a damage rate of ~4 x 10^{-4} dpa/s at a fluence of ~10 dpa. Experimental parameters were adjusted to permit a direct overlap with an experiment currently being performed at ANL.

Specimen evaluation is still in progress and microstructural data will be reported later. Preliminary transmission electron microscopy results indicate that cavity, precipitate and dislocation components of the microstructure are qualitatively similar to those observed previously in this material[4].

VI. REFERENCES

1. P. J. Maziasz and E. E. Bloom, AOIP Quarterly Report, DOE/ET/0058/1, August 1978.

2. S. Wood, J. A. Spitznagel and W. J. Choyke, OAFS Quarterly Report DOE/ER-0046/3, November 1980.

3. J. A. Spitznagel, unpublished work.

4. S. Wood, J. A. Spitznagel and W. J. Choyke, DAFS Quarterly Report, DOE/ET-0065/6, July 1979.

VII. FUTURE WORK

Analysis of the final experiments on the aged 316 SS will be completed and correlated with data from ANL and PNL. No additional dual-ion experiments will be performed. Balance of contract effort will concentrate on more in-depth analysis of helium migration and trapping effects and microchemical changes in previously bombarded SA, CW and aged 316 SS and Ti-modified 316 SS.

VIII. PUBLICATIONS

S. Wood, J. A. Spitznagel, W. J. Choyke, N. J. Doyle, J. N. McGruer and J. R. Townsend, "Maximum Equilibrium Bubble Size Determinations in Dual Ion Bombarded 316 SS," submitted to Scripta Metallurgica, December 1980.

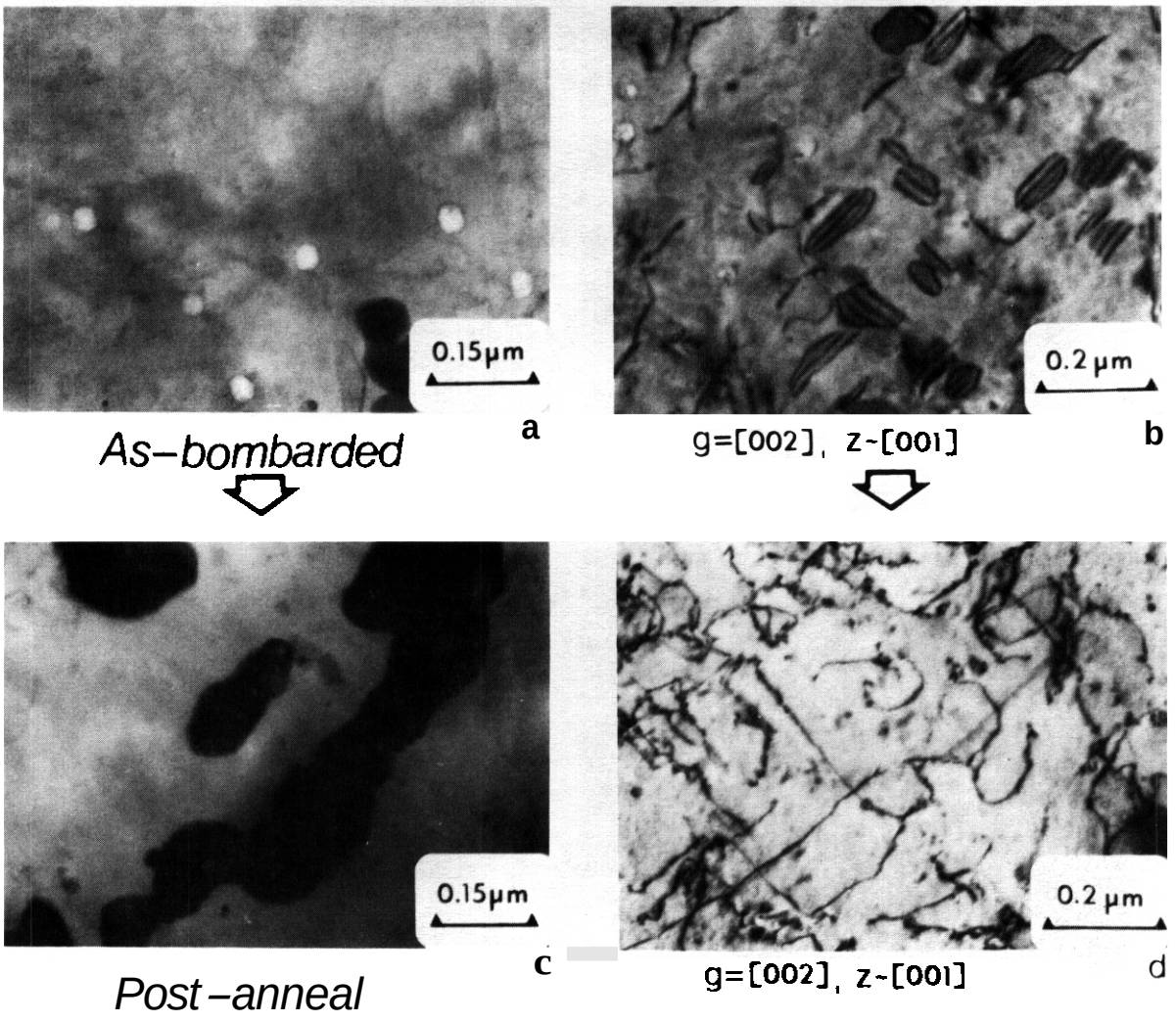

Fig. 1

Microstructures developed in 316 SS + Ti after dual-ion bombardment at 600°C to ~2.5 dpa (with a damage rate of ~2.4 x 10^{-5} dpa/s and an appm He/dpa ratio of 70:1). Micrographs c and d were obtained after a Post-bombardment anneal at 900°C for 0.5h.

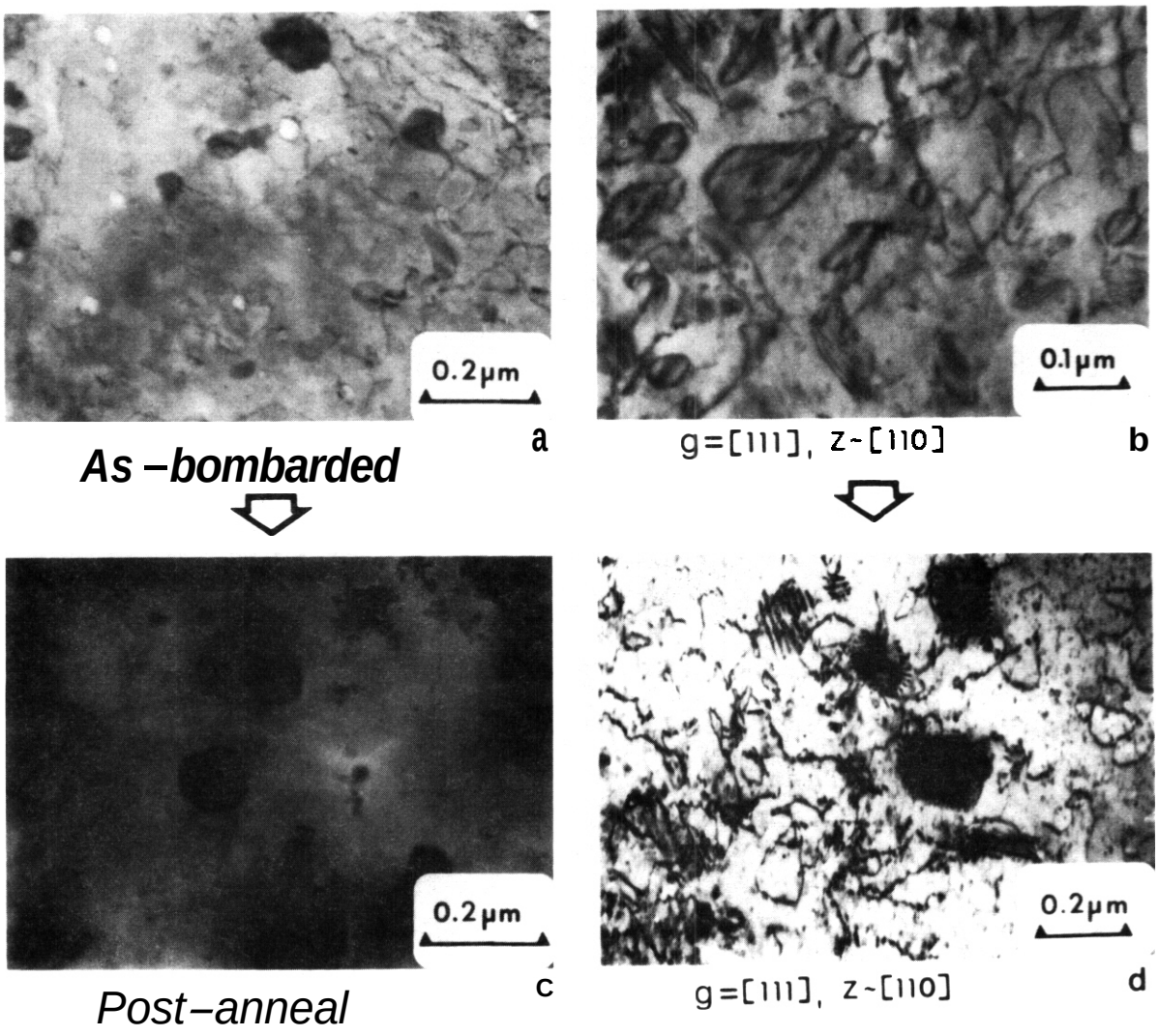

Fig, 2

Microstructures developed in 316 SS + Ti after bombardment at 600°C to ~2.5 dpa with a damage rate of 10^{-4} dpa/s and an appm He/dpa ratio of 70:1. Micrographs c and d were obtained after a post-bombordment anneal ot 900°C for 2h.

I. PROGRAM

Title: Irradiation Effects Analysis (AKJ)
Principal Investigator: D. G. Doran
Affiliation: Hanford Engineering Development Laboratory

II. OBJECTIVE

To determine the effects of neutron energy spectra on the microchemical and microstructural development in a cold-worked type 316 steel irradiated to high neutron fluences.

III. RELEVANT DAFS PROGRAM PLAN TASK/SUBTASK

Task II.C.l.l Phase Stability Mechanism Experiments
Task II.C.2.2 Fast-spectrum/mixed spectrum correlations for Fe-Ni-Cr alloys

IV. SUMMARY

Preliminary examination of 00 heat specimens of AISI 316 irradiated in EBR-II to about 70 dpa has shown that the microstructural development is consistent with the measured immersion density changes and also the trends observed in other heats of this alloy. The rate of helium generation is also consistent with previous measurements.

V. ACCOMPLISHMENTS AND STATUS

A. Microstructural Development of 20% Cold-Worked 316 Irradiated in EBR-II - H. R. Brager and F. A. Garner (HEDL)

1. Introduction

In a previous report it was shown that there were several large

problems to be overcome before a statistically significant swelling equation for AISI 316 stainless steel could be developed for fusion reactor applications.[1] A primary problem is that there are very little data from different reactors on the comparative swelling response of a single heat of steel. This distinction is very important since the heat-to-heat variation of AISI 316 has been found to be as important as any other variable in the determination of thisalloy's response to irradiation.[2]

In the study of the influence of helium on microstructural development the only data on a single heat of AISI 316 was derived from the DO heat of steel irradiated in EBR-II and HFIR.[1] All available data for this heat are reproduced in Figures 1-4. Surprisingly the data in Figures 3 and 4 which are from the **HFIR** reactor, fall on or near the curves determined by the EBR-II data, even though there is two orders of magnitude difference in the helium levels generated by these two reactors. This suggests that at high displacement levels the role of helium in determining the total amount of swelling may not be as large as previously expected, particularly

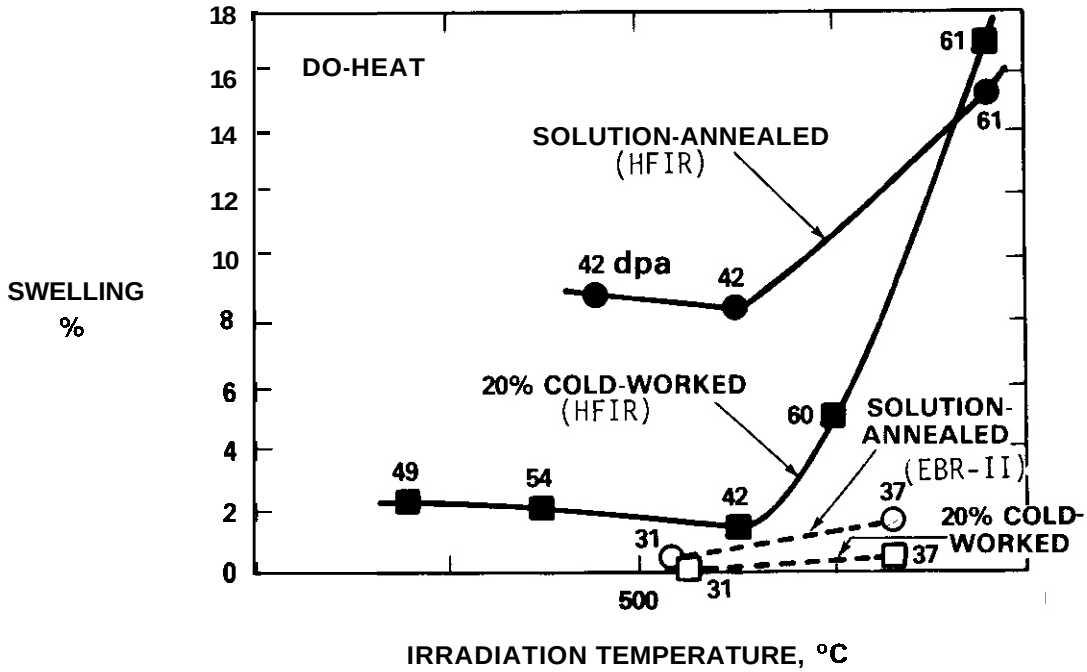

FIGURE 1. Swelling of Both 20% Cold-Worked and Annealed AISI 316 (DO-Heat) Irradiated in HFIR and EBR-II.[5]

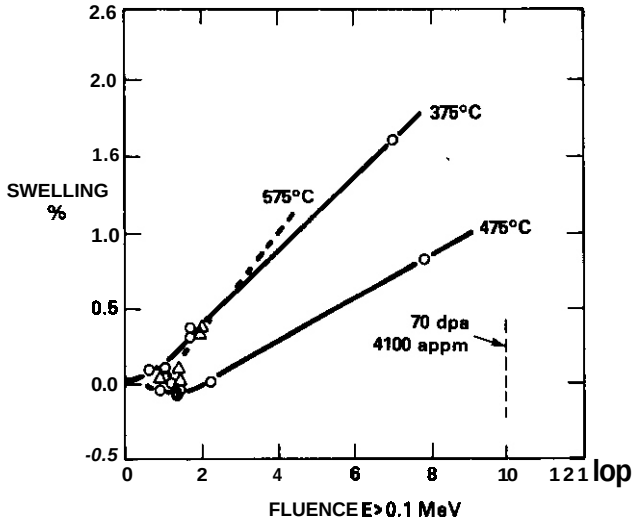

FIGURE 2. Swelling of 20% Cold-Worked AISI 316 (DO-Heat) Irradiated in HFIR.[6]

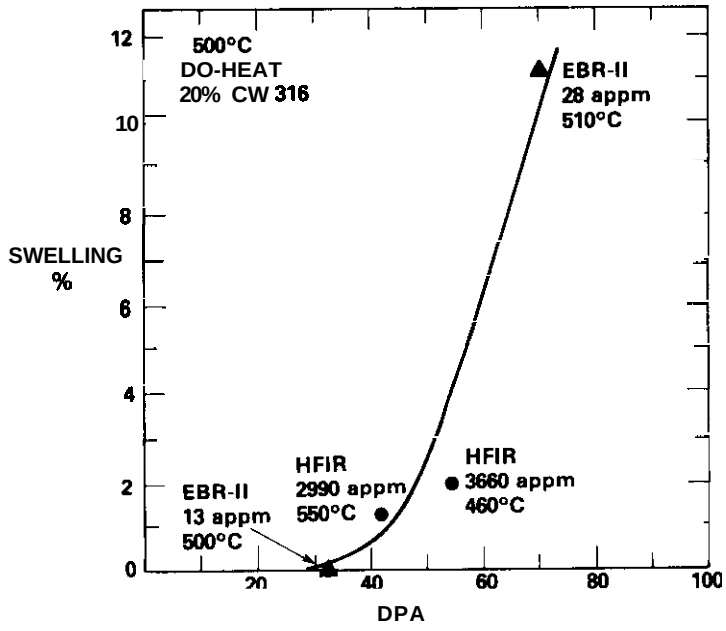

FIGURE 3. Comparison of Swelling Data on 20% Cold-Worked 00-Heat at ~500°C.[1]

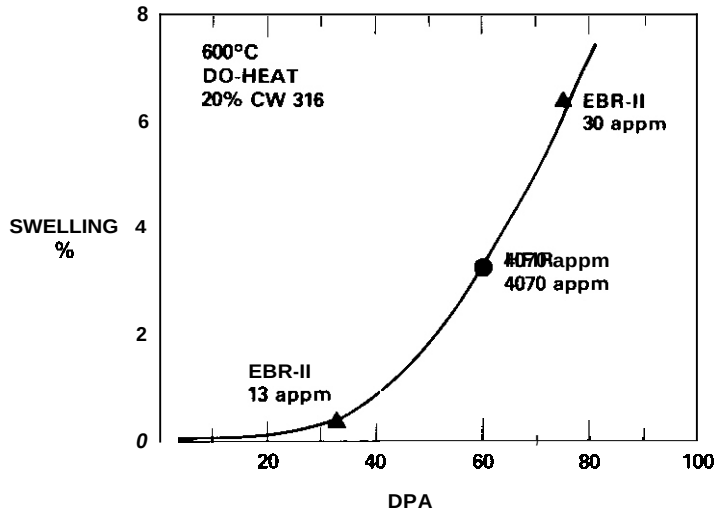

FIGURE 4. Comparison of Swelling Data on 20% Cold-Worked DO-Heat at ~600°C.(1)

at temperatures where the steel is known to swell with relative ease.

In an attempt to assess the validity of this conclusion, a series of examinations have been initiated, using previously reported (3) experimental techniques.

2. Determination of Helium Concentrations in DO-Heat Irradiated in EBR-II

One specimen irradiated to about 70 dpa in EBR-II at 510°C was analyzed by Dr. H. Farrar at Rockwell International in Canoga Park, CA. Duplicate determinations showed the helium concentration to be approximately 37 atomic parts per million, slightly larger than shown in Figure 3 but in fairly good agreement with the previously published production rate of 0.5 appm/dpa for 316 stainless steel irradiated in EBR-II.(4)

3. Microscopic Examination of DO-Heat Irradiated in EBR-II

It is anticipated that the microstructures developed in DO-heat during irradiation will be examined for materials irradiated in the 500-600°C

range in both HFIR and EBR-II. Preliminary results shown in Table 1 indicate that the large density changes observed in this steel after EBR-II irradiation are caused primarily by irradiation-induced voids. Typical micrographs are shown in Figures 5 and 6. A surprising feature of these specimens is the

TABLE 1

MICROSTRUCTURAL MEASUREMENTS: 20% COLD-WORKED 00-HEAT IRRADIATED IN EBR-II

Irradiation Temperature (°C)	Fluence [n/cm^2 (E >0.1 MeV)]	(dpa)	Void Diameter Å	Voids Number Density (voids/cm^3)	Void Volume (%)	Immersion Density Change $(-\frac{\Delta\rho}{\rho})(\%)$
510	13.8×10^{22}	69	~1100	1.4×10^{14}	~10%	9.9
620	15.0×10^{22}	75	~1200	8×10^{13}	~7%	6.4

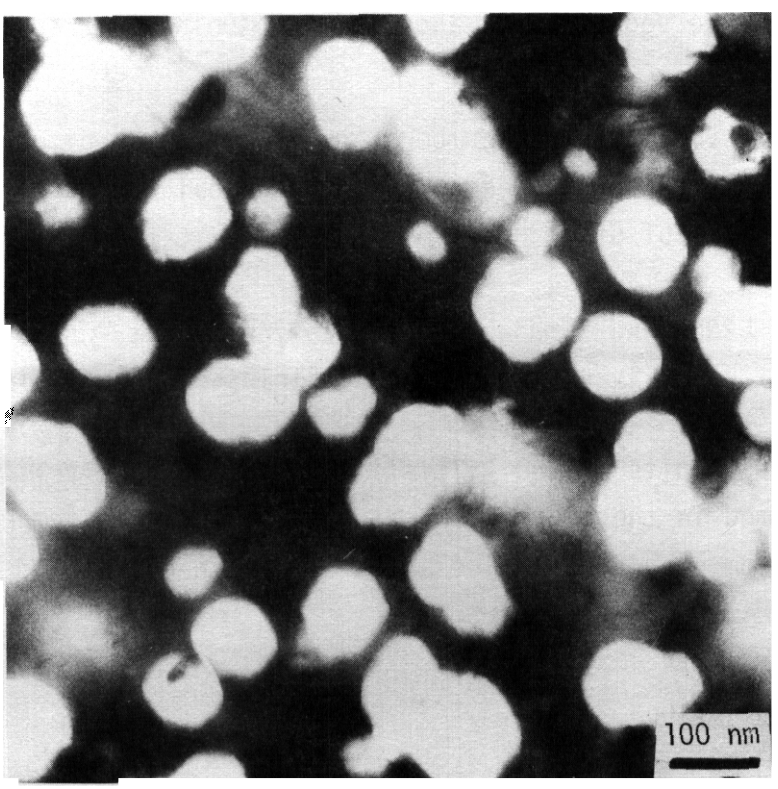

FIGURE 5. Voids Observed at 510°C and 69 dpa in 00-Heat Irradiated in EBR-II.

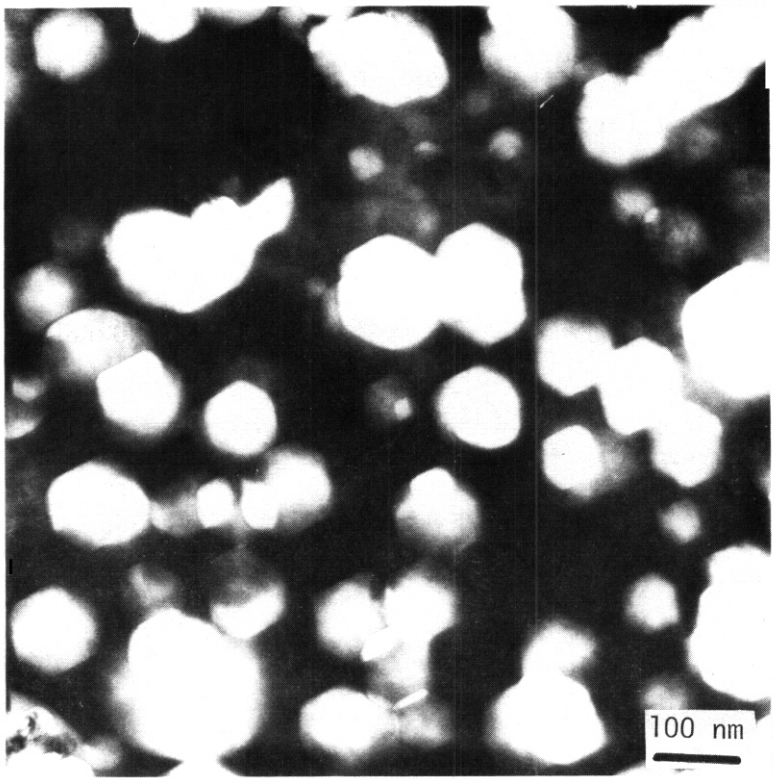

FIGURE 6. Voids Observed at 620°C and 75 dpa in DO-Heat Irradiated in EBR-II.

similarity of both void size and number density in the specimens irradiated at different temperatures. A greater difference would be expected based on previous examinations of other heats of steel.

At 620°C and 75 dpa the dislocation density was 2 x 10^{10} cm^{-2}, comparable to that normally observed in 316 stainless steel at this high fluence.

The results of the initial microchemical analysis indicate that precipitates formed in these specimens at their calculated temperatures are those expected from previous studies and are rich in nickel and silicon as expected.

4. Conclusions

Preliminary examination of DO-heat specimens of AISI 316 SS

irradiated in EBR-II to about 70 dpa has shown that the microstructural development is consistent with the measured immersion density change and with trends observed in other heats of this alloy. The rate of helium generation is also consistent with previous measurements.

VI. REFERENCES

1. F. A. Garner, P. J. Maziasz, and W. G. Wolfer, "Development of a Swelling Equation for 20% Cold-Worked 316 in a Fusion Device," DAFS Quarterly Report DOE/ER-0046/3, p. 159.

2. F. A. Garner, "The Microchemical Evolution of Irradiated Stainless Steels," Proceedings of AIME Symposium on Irradiation Phase Stability, Pittsburgh, PA, October 5-9, 1980, (in press), HEDL-SA-2159.

3. H. R. Brager and F. A. Garner, "Analysis of Radiation-Induced Microchemical Evolution in 300 Series Stainless Steels," Proceedings of AIME Symposium on Advanced Techniques for the Characterization of Irradiated Materials, Las Vegas, NV, February 1980, (in press), HEDL-SA-1883.

4. R. L. Simons, "Helium Production in Fast Breeder Reactor Out-of-Core Structural Components," in Effects of Radiation on Structural Materials, ASTM STP 683, J. A. Sprague and David Kramer (Eds), American Society for Testing and Materials, 1979, p. 365-379.

5. P. J. Maziasz, F. W. Wiffen, and E. E. Bloom, "Swelling and Microstructural Changes in Type 316 Stainless Steel Irradiated Under Simulated CTR Conditions," ORNL/TM-5396.

6. M. L. Grossbeck and P. J. Maziasz, "The Swelling of 20% Cold-Worked Type 316 Stainless Steel Irradiated in HFIR to Helium Levels of 200-3700 appm," ADIP Quarterly Report DOE/ET-0058/1, August 1978, p. 82.

VII. FUTURE WORK

The analysis of the high fluence specimens will continue. P. J. Maziasz of ORNL will participate injoint examination of the microstructures of specimens irradiated in both EBR-II and HFIR.

I. PROGRAM

Title: Irradiation Effects Analysis (AKJ)
Principal Invesigator: D. G. Doran
Affiliation: Hanford Engineering Development Laboratory

II. OBJECTIVE

The objective of this effort is to identify the role of each major element in the microchemical evolution of AISI 316 and the dependence of that role on preirradiation treatment and parameters such as neutron energy and flux, temperature and stress.

III. RELEVANT DAFS PROGRAM PLAN TASK/SUBTASK

Task II.C.2.4 Modeling

IV. SUMMARY

It is proposed that the primary role of cold work on the swelling of AISI 316 is to distribute the element carbon throughout the alloy matrix and increase the apparent solubility of carbon by binding it in the stress-field of the dislocation core. The resultant decrease in supersaturation and activity of carbon leads to a decrease in the rate of phase formation which preceeds swelling. A model developed to describe this phenomenon predicts that all carbon present in 20% cold-worked AISI 316 of nominal specification will be initially in bound-solution at all irradiation temperatures.

V. ACCOMPLISHMENTS AND STATUS

A. The Influence of Dislocation Density and Radiation on Carbon Activity and Phase Development in AISI 316 - F. A. Garner (HEDL) and W. G. Wolfer (U. of Wisc.)

1. Introduction

In a recent paper it was noted that the roles of carbon and cold-work appear to be interrelated.[1] The available data indicate that cold-work suppresses swelling at all temperatures in AISI 316[2,3] and that the role of cold-work lies in the retardation of radiation-induced precipitation and microchemical evolution. Out-of-reactor, the normal role of cold-work in this steel is to accelerate the phase evolution rather than to retard it, however.[4] Any model developed to explain the role of cold-work must successfully address this apparent contradiction.

The model must also explain the role of carbon on the swelling of this alloy. Even though cold-work retards swelling at all temperatures, carbon reverses its role with temperature. At low temperatures, the addition of carbon depresses swelling in AISI 316,[5,6,7] primarily by extending the incubation period as shown in Figure 1. At temperatures between 500 and 550°C, however, carbon begins to increase swelling as shown in Figure 2. As Figure 3 shows, the effect of carbon in increasing swelling at high temperature is visible in a variety of thermal-mechanical starting conditions and exhibits a synergism with other interstitial solutes such as nitrogen.[8] The role of carbon on phase development appears to be different in the low and high temperature regimes[1] and is currently being investigated in more depth. One expression of the changing role of carbon with temperature is its role in determining the relative height of the two swelling peaks usually observed in annealed 316. This is schematically illustrated in Figure 4.

In this report the relationship of cold-work and carbon solubility during irradiation will be addressed. The additional influence of radiation-produced vacancies on carbon activity will also be considered. The role of carbon on phase stability will be addressed in later work.

2. Solubility of Carbon in Austenitic Stainless Steels

AISI 316 contains about 0.04 weight percent of carbon. This amount of carbon is soluble in the austenitic phase above a temperature of about 1100°C, and it presence reflects the high solubility in the liquid phase. At lower temperatures, however, this amount of carbon is in supersaturation,

and it tends to precipitate in the form of carbides such as $M_{23}C_6$ and M_7C_3. The rate *of* precipitation in the absence of irradiation depends on the tine, the temperature, and the level of cold-work, according to the famililar T-T-P plots. One role of cold-work is to provide favorable nucleation sites for the carbide precipitates. This leads to a reduction in the incubation time for carbide precipitation compared to that of the annealed material.

As mentioned previously, cold-work appears to retard phase evolution during irradiation. It is proposed here that the dense, dynamic and mobile dislocation network maintained by irradiation leads to a reduction in the driving force for precipitation. This occurs as a result of the binding of carbon atoms in the stress-field of dislocations, as described below.

3. Solute Adsorption in Dislocation Fields

The mechanical interaction energy $U(r,\phi)$ between a misfitting solute atom and a dislocation results in a non-uniform solute distribution given by

$$C(r,\phi) = C_o \exp(U/kT) \qquad (1)$$

Here, C_o and C are the atom fractions of solute in equilibrium far and close to the dislocation, respectively. The interaction energy for an isotropic solute inclusion is given by

$$U = \frac{A \sin(\phi)}{r} \qquad (2)$$

in a linear isotropic elastic medium. The dependence on ϕ reflects the fact that carbon tends to be attracted only to the tensile side of the dislocation core.

$$A = \frac{Gb}{3\pi} \frac{1+\nu}{1-\nu} v, \qquad (3)$$

where G is the shear modulus, b the Burger vector, ν is Poisson's ratio, and v the relaxation volume or the partial molar volume of the solute.

Equation (1) is valid as long as the local solute concentration $C(r,\phi)$, does not exceed the number of available solute sites in the host lattice. If we assume that carbon occupies the octahedral interstitial sites in the fcc structure of austenitic steel, then there is one solute site per host atom. Accordingly, C can not exceed the value of one. The region of complete occupation of all available solute sites can be determined from Equation (1) by setting C = 1. This defines the radial distance $r_0(\phi)$ from the dislocation which marks the boundary of the fully occupied solute region. With Equation (2) we find

$$\frac{A/kT}{(1/C_0)} \sin\phi \qquad \text{for } 0 < \phi < \pi \tag{4}$$

if $A > 0$.

The total atom fraction of solutes trapped in the saturated region of dislocations is then given by

$$N_0 = \rho \int_0^{\pi} d\phi \int_0^{r_0(\phi)} r\,dr$$

$$= 1/4\ \pi\ \rho\ [A/kT \cdot \ln\ (1/C_0)]^2 \tag{5}$$

where ρ is the dislocation density.

To evaluate Equation (5), the relaxation volume of carbon in the austenitic matrix is needed. This can be obtained from lattice parameter measurements on austenites with varying carbon content. According to Hume-Rothery,[9] the lattice parameter is given by

$$a = (0.3564 + 0.076\ C) \qquad \text{in nm.} \tag{6}$$

In order to determine the relaxation volume v one can relate it to the change in lattice constant with carbon addition according to the relationship

$$\frac{v}{\Omega} \equiv 3\ \frac{1}{a}\ \frac{da}{dC}. \tag{7}$$

Therefore from Equations (6) and (7) we obtain

$$v/\Omega = 0.64$$

where $\Omega = 1.132 \times 10^{-29}\ m^3$ is the atomic volume of the solvent atoms.

Using the values $\nu = 0.3$, $\mu = 10$ Mpa, we obtain

$$N_o = 5.11 \times 10^{-16}\ \rho\ [1000/T \ln (1/C_o)]^2 \qquad (8)$$

for the atom fraction of carbon atoms bound in the dislocation cores.

Beyond the saturated region, carbon atoms are still attracted to the dislocation region, but the concentration remains below saturation. This additional trapping in the remote stress field has been evaluated by Hirth and Carnahan[10] for the case of hydrogen as an interstitial solute in bcc iron. They concluded that the enhancement of the hydrogen concentration in the remote stress field is only significant for dislocation densities above $10^{15}\ m^{-2}$ and for very low hydrogen contents of the order of 10^{-8} atomic fraction. For the present analysis, we assume that we may therefore neglect this additional contribution for the case of carbon.

4. Effect of Dislocations on Carbon Solubility

The solubility of carbon in austenite has been determined experimentally by Rosenberg and Irish[11] and by Tuma et al.[12,13] It is defined as the carbon concentration at which the chemical potential of carbon in solution becomes equal to the chemical potential of carbon in $M_{23}C_6$. Tuma et al. have developed the following equation to fit the experimental results. If N_C and N_{Ni} are the atomic fractions of carbon and nickel, the maximum atom fraction of carbon in solution is given by

$$\log N_C = 2.93 - 4.0\ N_{Ni} + (4500\ N_{Ni} - 6800)/T \qquad (9)$$

where T is the abolute temperature. The form of this equation is suggested by thermodynamic considerations. As a result, it can be extrapolated beyond the temperature range of 700°C to 1200°C where the data were obtained. Figure

5 shows the predictions of Equation (9) for the solubility of carbon as a function of temperature and nickel content of the matrix. The horizontal dashed line represents the actual carbon concentration (0.04 wt%) in AISI 316 stainless steel prototypic of that used in U. S. Fast Flux Test Reactor. It is evident that in the 300-700°C temperature range for breeder reactor operation, the carbon supersaturation is very high and provides a strong driving force for carbide precipitation.

The effect of a high dislocation density on the solubility can now be determined with Equation (8) when $N_c(T)$ is substituted for C_o. The results are given in Table 1 together with the matrix solubility N_c for a ternary alloy comparable in composition to that of AISI 316.

Table 1
Solubility of Carbon in Fe - 18%Cr - 14%Ni (in Atom Fractions)
With Different Dislocation Densities

T,°C	N_c	N_o = 10^{12} m^{-2}	N_o = 10^{14} m^{-2}
300	4.0×10^{-9}	$4.2 \times$	4.2×10^{-4}
400	1.6×10^{-7}	$4.6 \times$	4.6×10^{-4}
500	$2.4 \times$	$5.1 \times$	5.1×10^{-4}
600	2.0×10^{-5}	5.7×10^{-6}	5.7×10^{-4}
700	1.1×10^{-4}	$6.5 \times$	6.5×10^{-4}
800	4.2×10^{-4}	7.3×10^{-6}	7.3×10^{-4}

It is seen that the apparent carbon solubility in heavily cold-worked materials is substantially higher than the solubility of the undislocated matrix. It should be noted that the network dislocation density of AISI 316 has been found to be $\geq 3 \times 10^{15}$ m^{-2} prior to irradiation and $6 \pm 3 \times 10^{14}$ m^{-2} after irradiation at all temperatures in the breeder reactor regime. At temperatures below ~500°C the Frank loop contribution to the dislocation density is on the same order or larger than that of the network dislocations. Therefore it can be seen that the initial bound carbon concentration in irradiated cold-worked AISI 316 is essentially that of the base alloy at all temperatures.

5. Discussion

Carbide precipitation depends critically on the supersaturation ratio. Based on the enhanced carbon solubility in cold-worked material, one could conclude that precipitation is delayed by cold-working rather than accelerated as observed out-of-reactor. However, there are two mitigating factors. First, carbon is locally enriched near dislocation cores. Second, the strain field provides a preferred nucleation site where the nucleation barrier energy is substantially reduced. Readily available carbon in close vicinity to a favorable nucleation site is the reason why carbide precipitation commences earlier in cold-worked materials compared to annealed materials.

However, for nucleation of carbides *to* take place near a dislocation it must be sessile for the period of the incubation. Under irradiation, the dislocations continue to climb, dragging along the carbon atmosphere. Under these dynamic conditions, formation of carbide precipitates is impaired, and precipitation at static sites becomes the controlling mechanism.

Under these conditions, the supersaturation formed by the ratio of actual carbon content divided by the apparent solubility is the driving force for carbide nucleation. This ratio is substantially less than the supersaturation ratio formed with the solubility N_c of Equation (9).

There is one test that can be made of the hypothesis underlying this model. Such a mechanism would cease to produce increases in the incubation period of swelling with increasing cold-work if the starting dislocation density saturated. As shown in Figure 6, swelling is not influenced by cold-work levels above 30% in AISI 316[14] and the dislocation density of AISI 316 also saturates at this cold-work level.[15]

If the primary role of cold-work on swelling is to redistribute the small carbon clusters that form upon cooling of annealed steel and then to decrease carbon's tendency to precipitate, what about other elements? The lesser interstitial elements such as phosphorus and nitrogen are known to affect carbon activity[1] and may also be adsorbed on dislocations. The substitutional element silicon is also known to strongly affect swelling but it has recently been shown that the effect of cold-work on swelling occurs in alloys bearing carbon but not silicon.[16] Silicon acts on swelling

primarily through its influence on the diffusion on vacancies and interstitials.[16,17]

If this model is correct, it is fair to ask in what manner will the carbon-dislocation interaction be observed in the swelling behavior? It is anticipated that the interaction will serve primarily to delay the phase evolution and therefore to delay the swelling as shown in Figures 1 and 7.

An additional effect of radiation is the change of the carbon diffusivity. Without radiation carbon diffuses interstitially and, therefore, at a much faster rate than vacancies. In the presence of the radiation-produced vacancies, however, carbon diffusion is reduced because of trapping in the vacancies. This mechanism has been proposed by Damask and coworkers[18,19] to explain the results of low-temperature irradiations in iron.

The reduction of carbon diffusivity thus depends on the vacancy concentration. Figure 8 shows the calculated vacancy concentration for fast reactor irradiations as a function of temperature for two dislocation densities. It is seen that the vacancy concentration is very high at low irradiation temperatures, and independent of the dislocation density. The vacancy concentration decreases rapidly with temperature, and becomes equal to the thermal vacancy concentration above 790°C.

Based on this behavior, it is expected that radiation strongly reduces carbon mobility through the matrix at low irradiation temperatures. However, this phenomenon decreases rapidly with increasing temperature, and the effect becomes negligible above 500°C. A more quantitative assessment requires a mechanistic model of carbon trapping in mobile vacancies.

6. Conclusions

It is proposed that the primary role of cold-work on the swelling of AISI 316 is to distribute the element carbon throughout the alloy matrix and increase its apparent solubility by binding it in the stress-field of the dislocation core. The resultant decrease in supersaturation and activity of carbon leads to a decrease in the rate of phase formation. Such phase formation has been shown to be the necessary precursor to swelling. A model developed to describe this phenomenon predicts that all carbon present

in AISI 316 of nominal specification will initially be in bound-solution at all irradiation temoeratures.

VI. REFERENCES

1. F. A. Garner, "The Microchemical Evolution of Irradiated Stainless Steels," HEDL-SA-2159, Symposium on Irradiation Phase Stability, Pittsburgh, PA, October 5-9, 1980 (in press).

2. H. R. Brager and F. A. Garner, "Dependence of Void Formation on Phase Stability in Neutron-Irradiated Type 316 Stainless Steel," Effects of Radiation on Structural Materials, ASTM STP 683, J. A. Sprague and D. Kramer (Eds), ASTM (1979), pp. 207-232.

3. H. R. Brager, F. A. Garner, E. R. Gilbert, J. E. Flinn, W. G. Wolfer, W. K. Appleby, and E. E. Bloom, in "Radiation Effects in Breeder Reactor Structural Materials," M. L. Bleiberg and J. W. Bennett (Eds), the Metallurgical Socity of the American Institute of Mining, Metallurgical and Petroleum Engineers (1977), pp. 727-755.

4. B. Weiss and R. Stickler, Met. Trans., 8 (1973) 851. Also J. E. Spruiell et al., Met. Trans., 4 (1973) 1533.

5. J. I. Bramman, C. Brown, J. S. Watkin, C. Cawthorne, E. J. Fulton, P. J. Barton and E. A. Little, "Void Swelling and Microstructural Changes in Fuel Pin Cladding and Unstressed Specimens Irradiated in DFR," ibid Ref. 3.

6. J. F. Bates, "Irradiation-Induced Swelling Variations Resulting from Compositional Modifications on Type 316 Stainless Steel," ASTM STP 570 (1975), pp 379-387.

7. J. L. Boutard, G. Brun, J. Lehman, J. L. Seran and J. M. Dupouy, "Swelling of 316 Stainless Steel," Proc. Sym. on Irradiation Behavior of Metallic Materials for Fast Reactor Core Components, Ajaccio, Corsica, June 5-7, 1979.

8. J. F. Bates, R. W. Powell and E. R. Gilbert, "Reduction of Irradiation-Induced Creep and Swelling by Compositional Modifications," ASTM 10th International Symposium on Materials, ASTM STP 725, 0. Kramer, H. R. Brager, J. S. Perrin (Eds) ASTM (in press).

9. W. Hume-Rothery, "The Structure of Alloys of Iron," Pergamon Press, Oxford, 1966, p. 137.

10. J. P. Hirth and B. Carnahan, "Hydrogen Adsorption at Dislocations and Cracks in Iron," Acta Met. 26 (1978), pp. 1795-1803.

11. S. J. Rosenberg and C. R. Irish, "Solubility of Carbon in 18 Percent Chromium - 10 Percent Nickel Austenite". J. Res. Nat. Bur. Standards 48 (1952) pp. 40-48.

12. H. Tuma, P. Groebner and K. Leobl; Archive Fuer Eisenheuttenwesen 40 (1969), pp. 727-731.

13. H. Tuma, M. Vyklicky and K. Loebl; Archive Fuer Eisenheuttenwesen 41 (1970), PP.

14. K. Uematsu, et. al., "Swelling Behavior of Cold-Worked Type 316 Stainless Steel," ibid Ref. 3, p. 571.

15. K. D. Challenger and T. Lauritzen, "Effect of the Degree of Cold Work on the Irradiation-Induced Swelling of Type 316 Stainless Steel, ASTM STP 570, 1975, p. 388.

16. H. R. Brager and F. A. Garner, "Radiation-Induced Evolution of the Austenite Matrix in Silicon-Modified AISI 316 Alloys," ibid Ref. 1.

17. F. A. Garner and W. G. Wolfer, "The Effect of Solute Additions on Void Nucleation," HEDL-SA-2155, submitted to J. Nuclear Materials. Also DOE/ET-0065/8, p. 71, and DOE/ET-0046-1, p. 149.

18. H. Wagenblast and A. C. Damask, "Kinetics of Carbon Precipitation in Irradiated Iron," J. Phys. Chem. Solids 23 (1962), 221-227.

19. F. E. Fujita and A. C. Damask, "Kinetics of Carbon Precipitation in Irradiated Iron--11. Electrical Resistivity Measurements," Acta Met. 12 (1964), 331-339.

20. E. E. Bloom, J. O. Stiegler, A. F. Rowcliffe and J. M. Leitnaker, Scripta Met. 10 (1976), 303.

VII. FUTURE WORK

The model will be expanded to cover the influence *of* Frank loops and also carbon levels higher than 0.04 weight percent. An experimental program involving alloys already irradiated in EBR-II or ORR will be defined and initiated to provide input to the modeling effort.

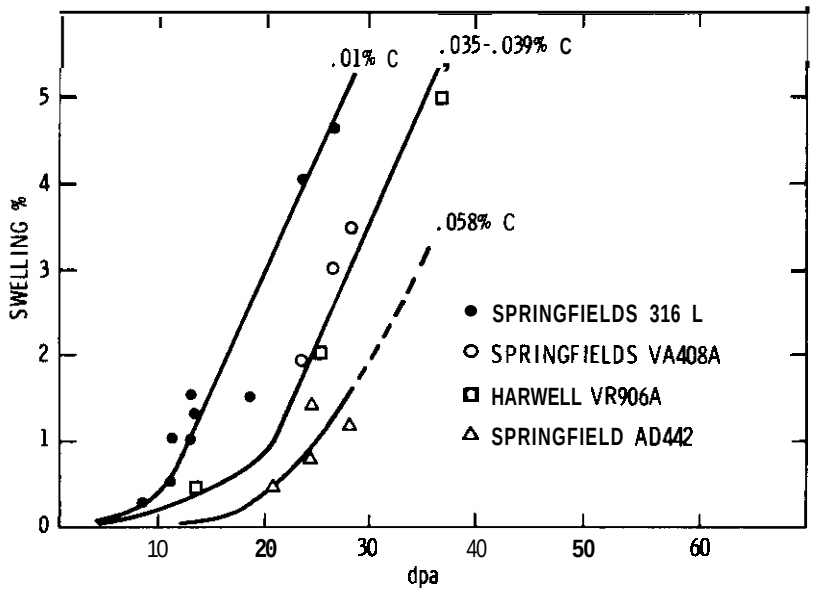

FIGURE 1. Carbon Prolongs the Incubation Period of Swelling at Low Temperatures.[5]

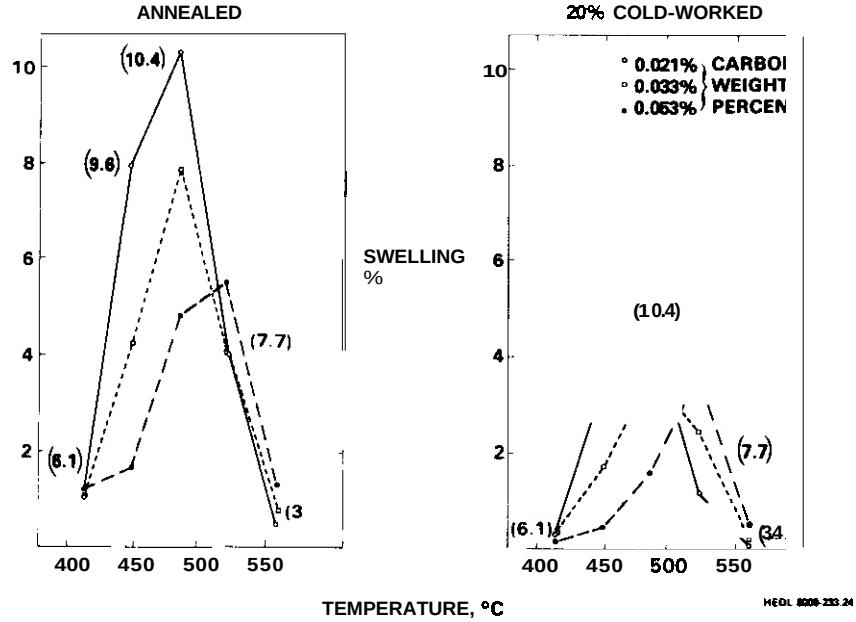

FIGURE 2. The Role of Carbon Shifts with Increasing Temperature, as Observed in Both Cold-Worked and Annealed Steel.[7] The numbers in parentheses are the fluence levels of each datum in 10^{22} n/cm^2 (E >0.1 MeV).

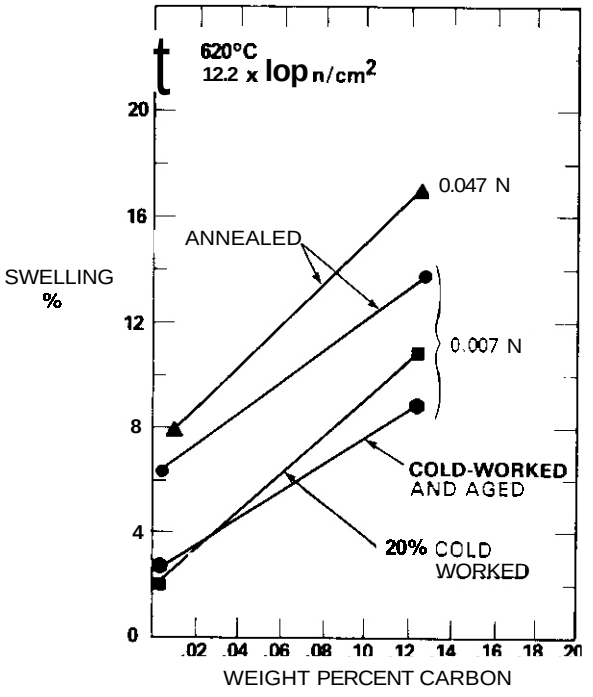

THE ROLE OF CARBON REVERSES WITH TEMPERATURE AROUND 520°C.

SWELLING INCREASES WITH CARBON AT HIGH TEMPERATURES

FIGURE 3. Swelling Increases with Carbon Level at High Temperatures for all Thermal-Mechanical Starting Conditions and Nitrogen Levels Tested.(8)

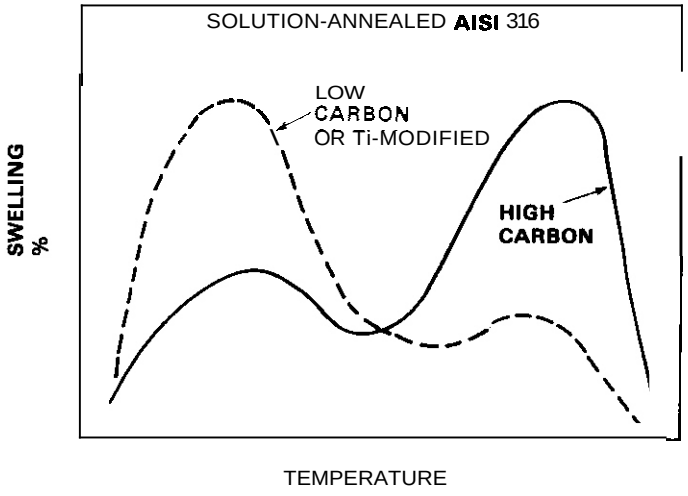

- CARBON LEVEL MODIFIES RELATIVE HEIGHT OF TWO PEAKS
- LOW CARBON AND Ti-MODIFIED STEELS EXHIBIT SIMILAR BEHAVIOR
- LOW TEMPERATURE SWELLING PEAK IN Ti-MODIFIED ALLOY DUE TO REDUCTION OF FREE CARBON 7

FIGURE 4. Schematic Representation of Dependency of Swelling in Annealed Fuel Pins on Free Carbon Level.(1)

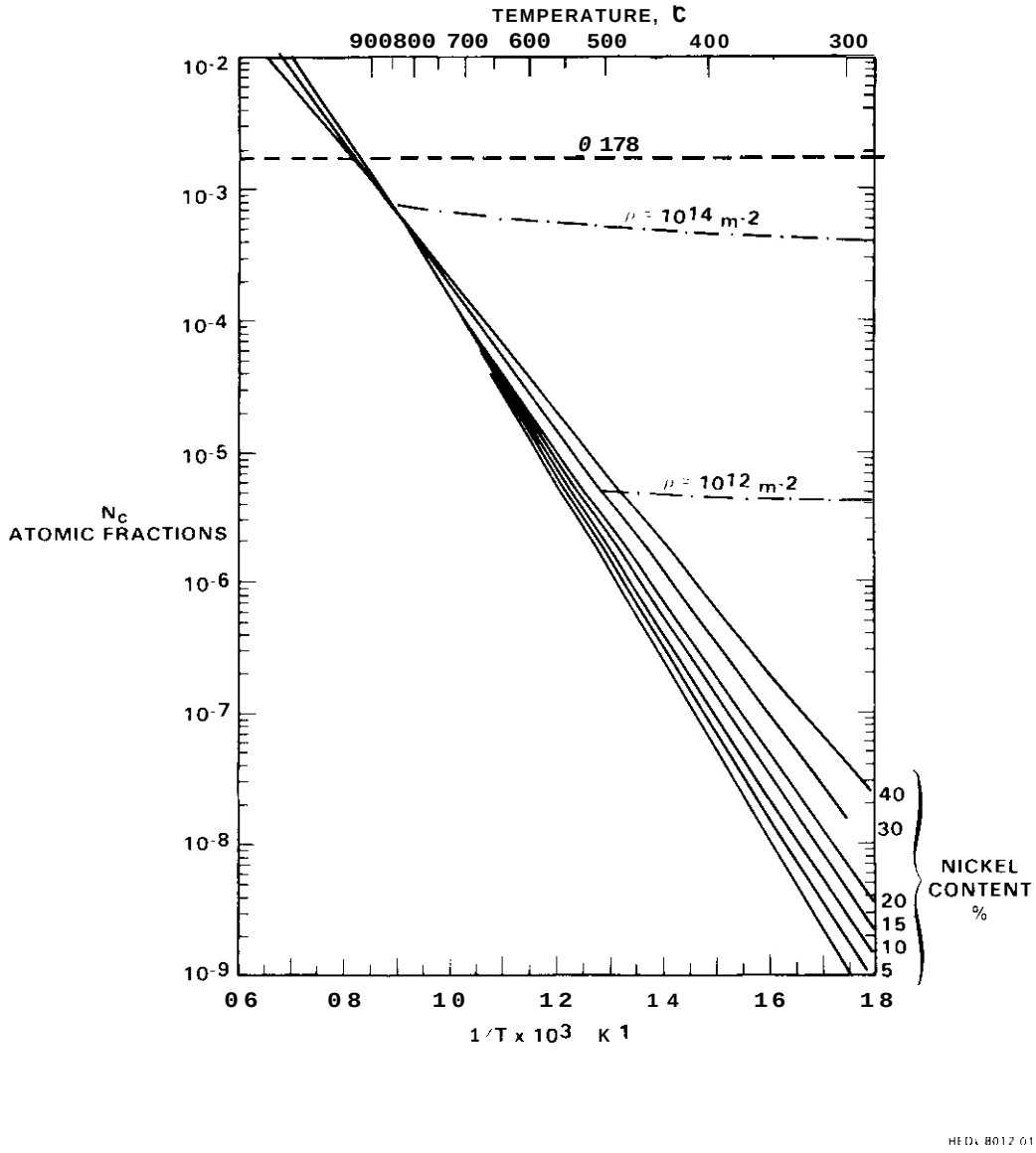

FIGURE 5. Effect of Nickel Level and Dislocation Density on the Temperature-Dependent Solubility of Carbon in Austenite. The horizontal line at 0.178 is the total atomic carbon level at 0.04 weight percent.

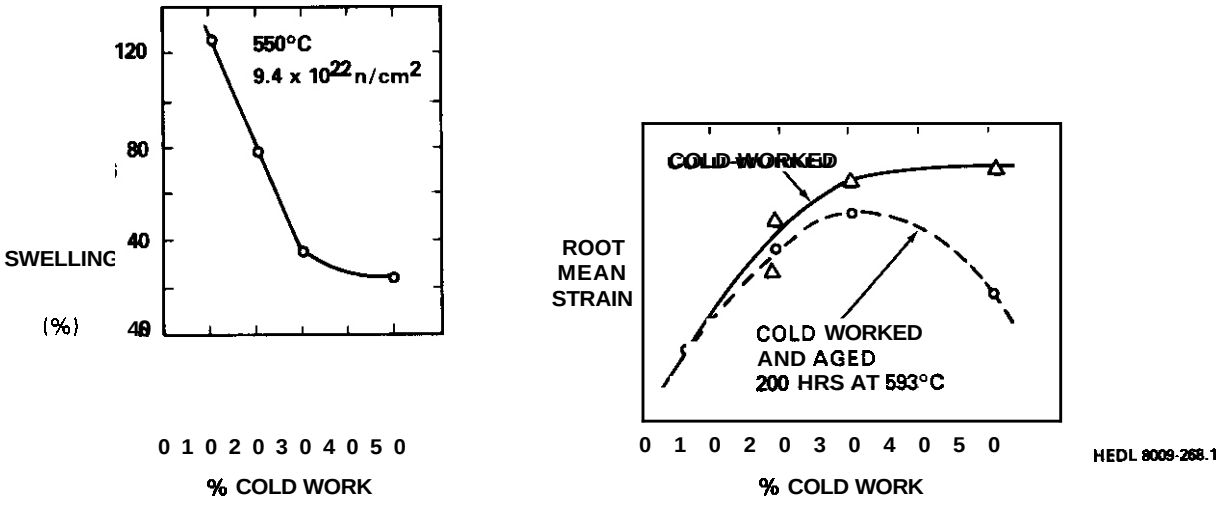

FIGURE 6. The Dependence of Swelling[14] and Dislocation Density[15] (Measured by Root Mean Strain) in AISI 316.

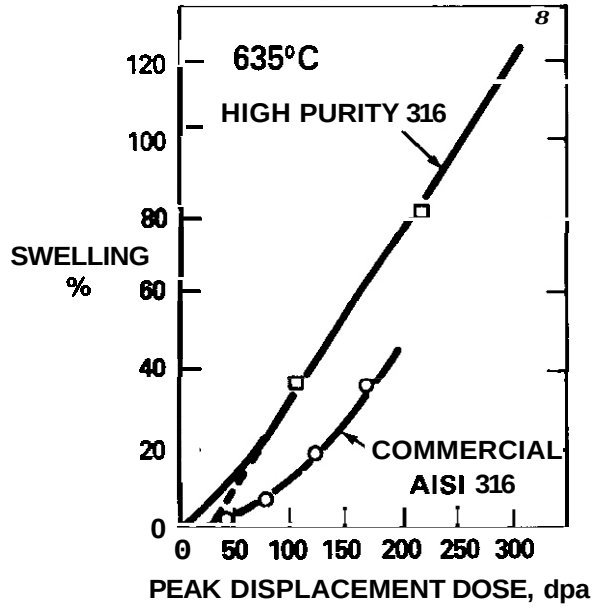

FIGURE 7. The Effect of Solute on Swelling of AISI 316 Observed in 5 MeV Ni^+ Ion Irradiation (Step-Height Measurements). The high purity steel has very small levels of carbon, nitrogen and silicon compared to the commercial steel.

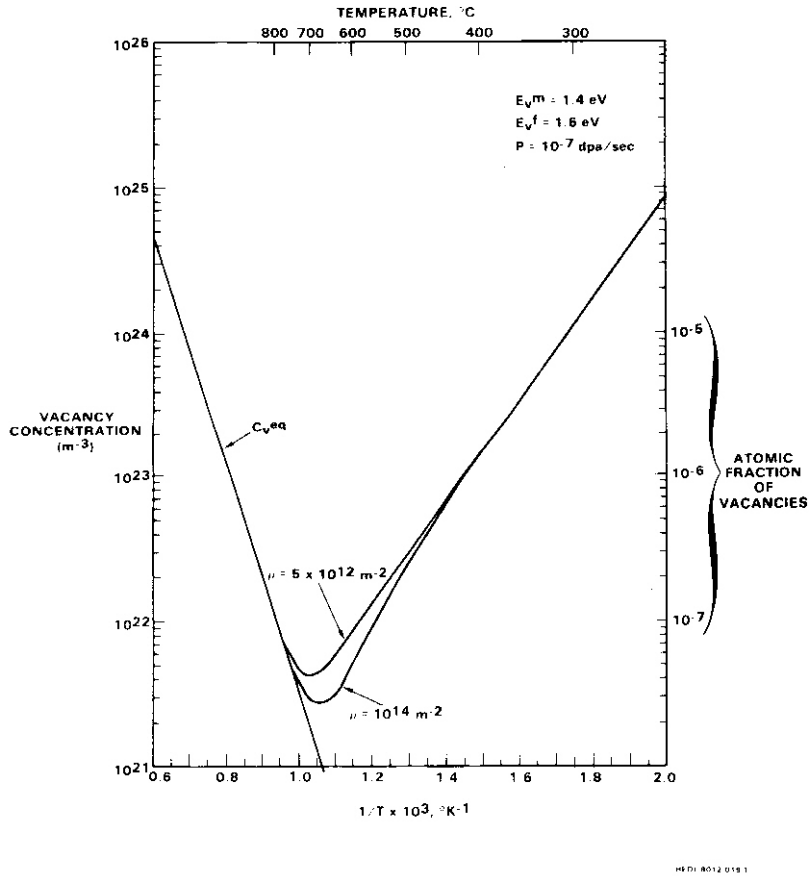

FIGURE *8.* The Calculated Dependence of the Vacancy Concentration on Temperature and Dislocation Density.

I. PROGRAM

Title: Irradiation Effects Analysis (AKJ)
Principal Investigator: D. G. Doran
Affiliation: Hanford Engineering Development Laboratory

II. OBJECTIVE

The objective of this effort is to identify the effects of applied and internal stresses on radiation-induced dimensional changes in metals.

III. RELEVANT OAFS PROGRAM PLAN TASK/SUBTASK

TASK II.C.2.1 Effects of Material Parameters on Microstructure
TASK II.C.2.4 Modeling

IV. SUMMARY

Data are now available which definitively show that stress plays a major role in the development of radiation-induced void growth in AISI 316 and many other alloys. Some earlier experiments which came to the opposite conclusion are shown to have investigated stress levels which inadvertantly cold-worked the material. Stress-affected swelling spans the entire temperature range in fast reactor irradiations and accelerates with increasing irradiation temperature. It also appears to operate in all alloy starting conditions investigated. Two major microstructural mechanisms appear to be causing the enhancement of swelling, which for tensile stresses is manifested primarily as a decrease in the incubation period. These mechanisms are stress-induced changes in the interstitial capture efficiency of voids and stress-induced changes in the vacancy emission rate of various microstructural components. There also appears to be an enhancement of intermetallic phase formation with applied stress and this is shown to increase swelling by accelerating the microchemical evolution that precedes void growth at high temperature. This latter consideration complicates the extrapolation of

these data to compressive stress states.

This paper is based on research conducted primarily in the U.S. Breeder Reactor Program and will be published in the proceedings of the ASTM meeting on "Effects of Irradiation on Materials," held in Savannah, GA. It forms the basis for additional fusion-related studies now in progress.

V. ACCOMPLISHMENTS AND STATUS

A. Stress-Enhanced Swelling of Metals During Irradiation -- F. A. Garner and E. R. Gilbert (HEDL) and D. L. Porter (ANL-WEST)

1. Introduction

The radiation-induced void swelling phenomenon has been found to be sensitive to a large variety of material and environmental variables. Until recently, however, the abundance of these variables has obscured the unequivocal identification of stress as an important parameter. Although the Frank loops formed during irradiation were found to be sensitive to the applied stress state,[1-3] various investigations *of* the effects of stress on void growth have been contradictory in their findings.[1,4-7]

A substantial amount of data is now available which definitively shows that stress plays a major role in the onset and rate *of* void growth in AISI 316 stainless steel in a variety of metallurgical conditions. A more limited set *of* data on AISI 304L and a number of other commercial alloys suggests that stress probably affects void growth in all alloys subject to swelling. The insight gained in this study allows, with hindsight, an understanding of the apparent discrepancies between these results and those of earlier studies. The parametric dependence of the stress-enhanced swelling phenomenon also provides important clues as to the identity and nature of themicrostructural mechanisms producing the enhancement of swelling, and thus provides some guidance on how to extrapolate the data derived from experiments involving tensile loads to those conducted under compressive 1oads.

2. Experimental Details

The data were derived from measurementsofthe changes in diameter, length and density of thin-walled pressurized tubes immersed in static sodium at elevated temperatures and irradiated in the EBR-II reactor. The pressurizing gas, either pure helium or argon-1%helium, produced in the tube wall a biaxial tensile stress state. Two types of tubes were used. The first was relatively short, ranging from 2.2 to 2.8 cm, and was incorporated into subcapsules maintained at relatively constant temperature. These are described in detail elsewhere.[8] The second type of tube was much longer (1.02 m) and was maintained throughout its length at either 400 or 500°C.[9] The longer tubes provide data at constant stress but varying displacement rate and neutron fluence along their length. The smaller tubes are considered to produce data at constant displacement rate and neutron fluence. Companion irradiations in one capsule of several tubes at different pressures provide information on the stress dependence of the swelling and irradiation creep phenomena.

The small tubes were irradiated in several irradiation experiments designated the P-1, P-2, P-5, AA-II and AA-VIII tests. The P-2 and P-5 tests employed thermocouple measurement of temperature while the AA-II and AA-VIII tests involved the use of thermal expansion devices. The P-1 test had no direct measurement *of* irradiation temperatures, which were estimated from heat transfer calculations.

Since irradiation creep will not contribute to length changes of such tubes, additional data on the density change can be inferred from length changes of those tubes which were not sacrificed for cutting and immersion density measurements but returned for further irradiation. The magnitude of stress-free swelling can also be derived from diameter measurements of pressurized capsules. Changes in diameter of pressurized tubes contain both creep and swelling-induced strains.

3. Alloy Descriptions

Nominal compositions of the alloys investigated in this study are given in Table 1. The majority of the data are derived from the "N-lot" (V87210) heat and the NICE-lot (K81581) heat. The former has been used throughout as a reference heat for the U.S. Breeder Program and the latter heat is the standard creep experiment material and is a heat prototypic of that used to construct the first core of the Fast Test Reactor. As shown elsewhere, these heats in the 20% cold-worked condition exhibit substantially different incubation periods prior to the onset of steady-state swelling, but possess similar steady-state swelling rates,[10] while the small tube experiments concentrated on the 20% cold-worked condition. Also included was AISI 316, the larger tube experiments were constructed from the same heat of steel as N-lot but in the 10% cold-worked condition and also N-lot steel which was initially 20% cold-worked, then aged for 24 hours at 482°C to nucleate precipitates, air quenched, and finally fully aged at 704°C for 216 hours, followed by another air quench. This latter heat is designated as heat-treat D (HTD) in subsequent discussions. All other alloys investigated in this study were irradiated as short tubes.

TABLE 1

NOMINAL ALLOY COMPOSITION IN WEIGHT PERCENT

Description	Fe	Ni	Cr	Mo	W	Nb	Si	Mn	Zr	Ti	Al	C	B	Other
AISI 316	55	13.5	17.5	2.5	-	-	0.6	1.75	-	-	-	.05	0.001	
M-813	39	35	18	4.0	-	-	-	-	0.1	2.25	1.4	.08	0.005	
Ninionic PE16	34	43.5	16.5	3.3	-	-	0.15	0.1	-	1.2	1.2	.05		1.0Co
Inconel X-750	6.75	73	15	-	-	0.85	0.3	0.7	-	2.5	0.8	.04	-	0.05Cu

4. Results

Typical results of the short-tube experiments on 20% cold-worked AISI 316 are shown in Figures 1-3. All of the data sets show significant enhancement of density change with increasing stress. The density change data are plotted vs. the hydrostatic stress present in the tube wall in anticipation of the physical model to be employed in the model description. (The hydrostatic stress in these specimens is one-half of the hoop stress.) Note that the density change measurements include strain contributions from both voids and phase-related density changes. The latter lead to densification at most fluences and temperatures [11] but, with one exception discussed later, are too small to account for any enhancement by stress of the density changes observed. Note also that the steepness of the curves increases with temperature.

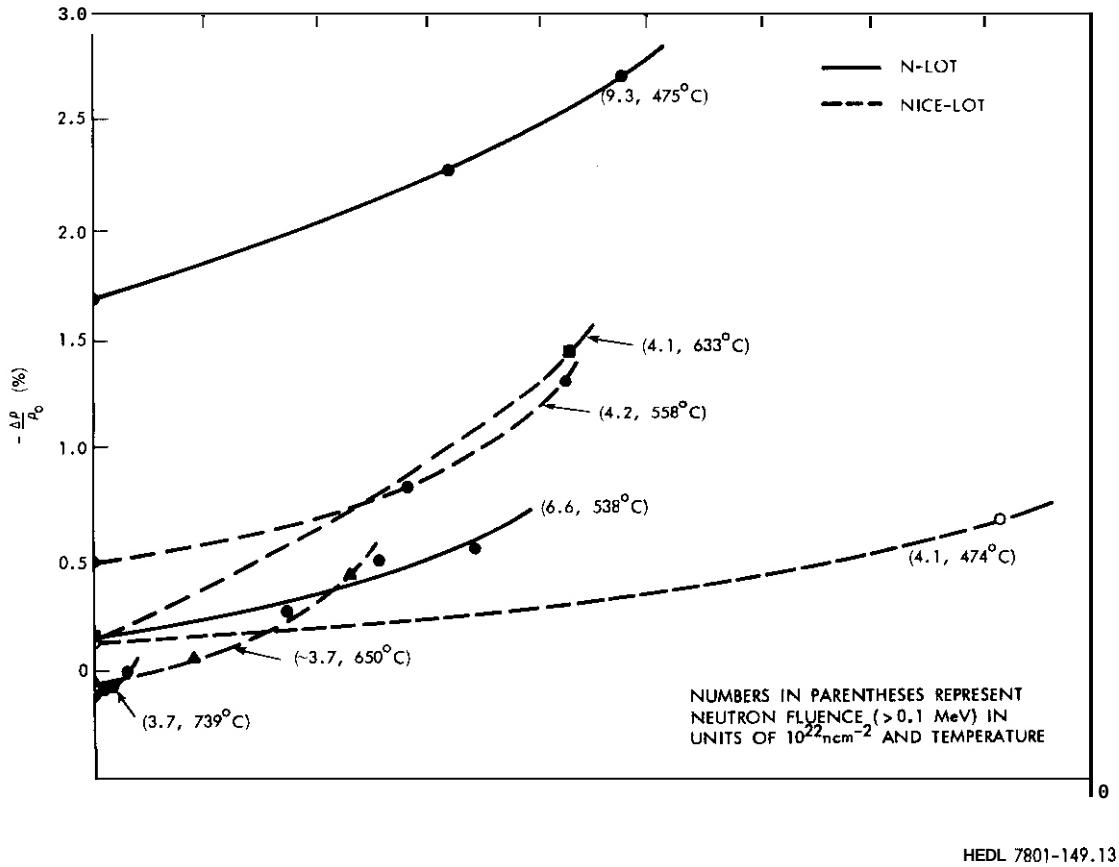

HEDL 7801-149.13

FIGURE 1. The Dependence of Neutron-Induced Density Changes in 20% Cold-Worked Stainless Steel on Hydrostatic Stress, Temperature and Neutron Fluence. These data form the basis of the curves shown in Figures 12 and 13.

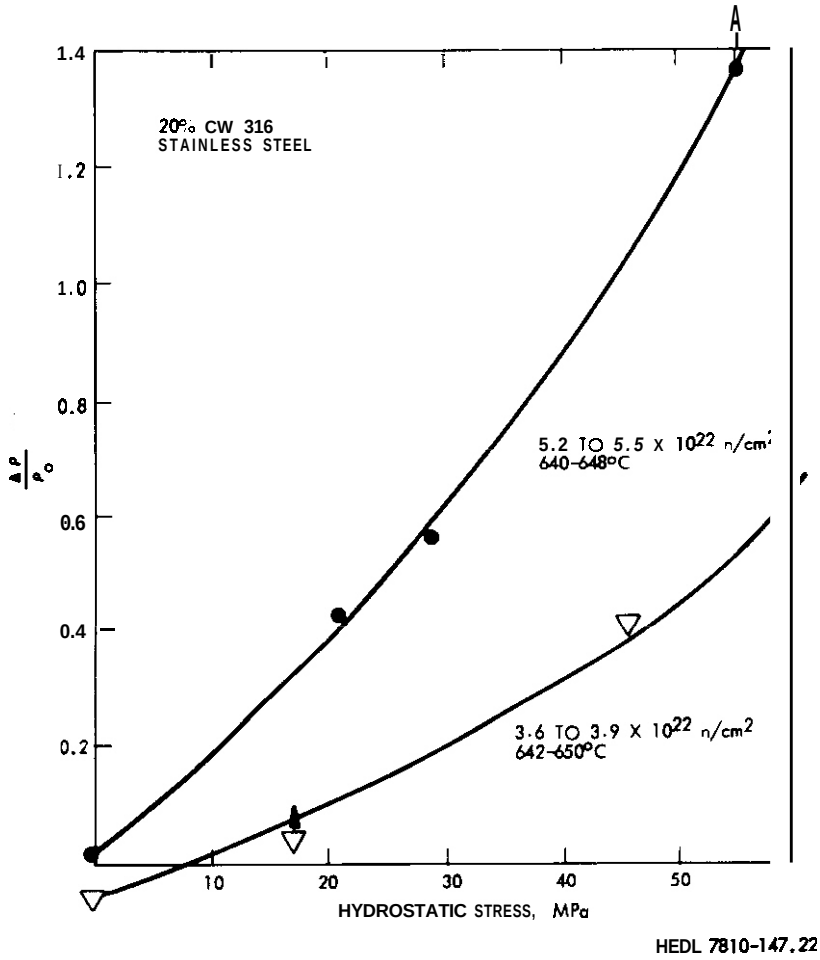

FIGURE 2. The Dependence of Radiation-Induced Density Change at Approximately 650°C in 20% Cold-Worked Stainless Steel on Hydrostatic Stress and Fluence. Several of these data points were included in Figure 1. The arrows represent the expected magnitude and direction of movement of each data point when normalized to the peak fluence in each data suhset.

Figure 4 contains some additional data derived from length change measurements. The N-lot specimen which was cold worked to only 5% exhibited an increase in swelling with stress until the material was subjected to a stress above the proportional elastic limit (PEL), whereupon swelling fell due to a preirradiation increase in specimen deformation (cold working by any method is known to reduce swelling). A similar behavior was observed in irradiations of annealed N-lot steel earlier.[4] The PEL increases with cold-work level and decreases with increasing temperature [12] but was not exceeded in the short tube experiments for the 20% cold-worked material.

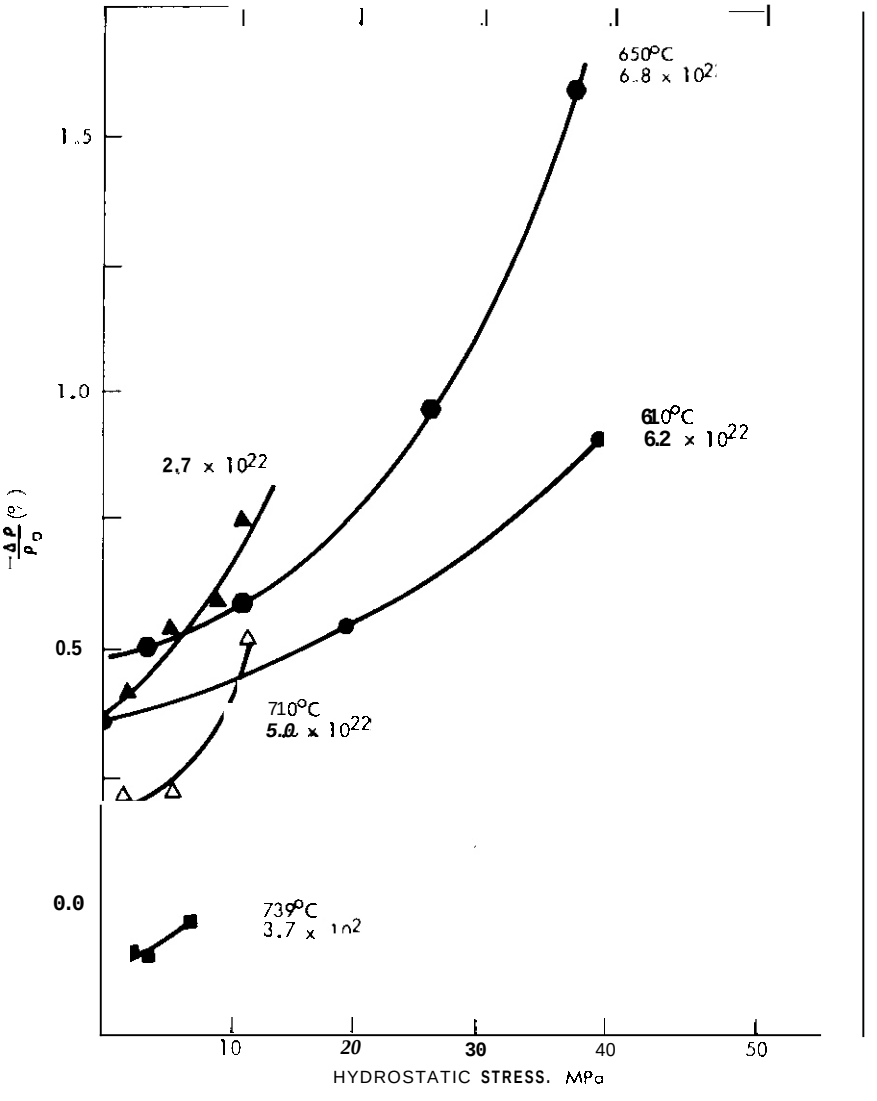

FIGURE 3. Additional Stress-Affected Swelling of the NICE-Lot Heat of 20% Cold-Worked 316 Stainless Steel From the P-2 Experiment.

Although the data in Figures 1-4 signal an unequivocal effect of stress on swelling, they do not indicate whether the stress affects the incubation period, the steady-state swelling rate, or both. The long tube experiments indicate, however, that stress affects primarily the incubation period of the 10%cold-worked and HTD conditions as shown in Figures 5-7. While the data in these figures do not preclude a stress effect on the swelling rate, analysis of the data in Figures 1-4 indicates that only a

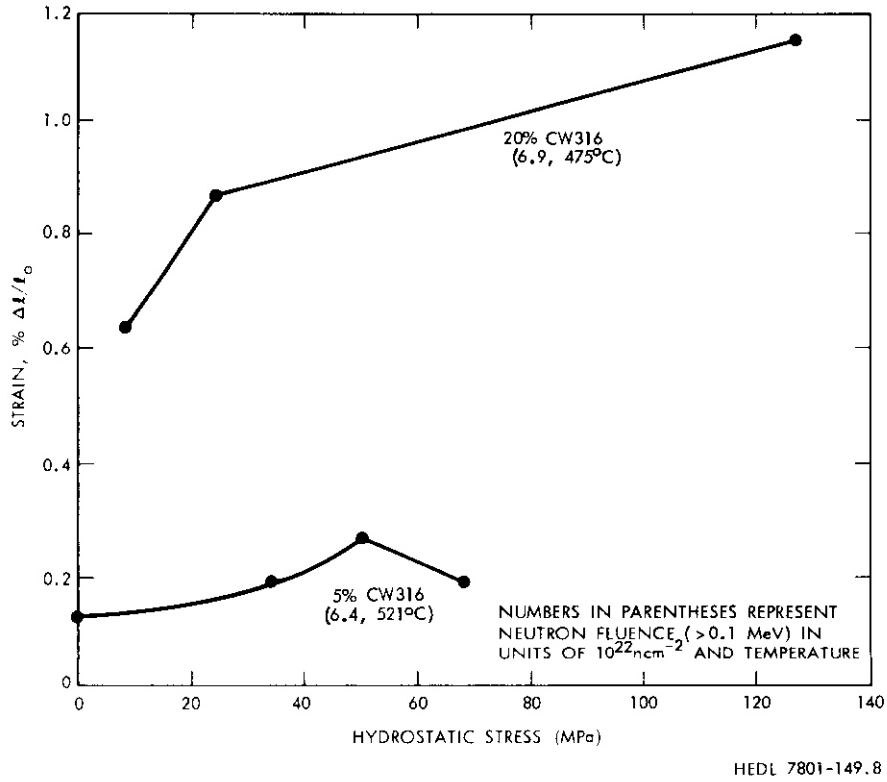

FIGURE 4. Length Changes of N-Lot Pressurized Tubes Irradiated in EBR-II.

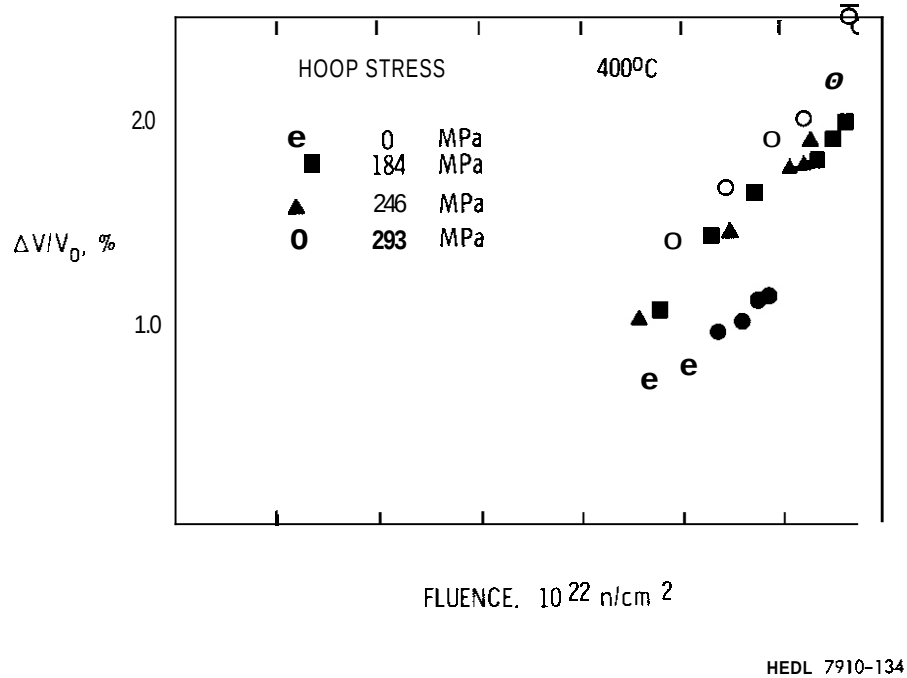

FIGURE 5. Stress-Affected Swelling Observed at 400°C in Long-Tube Capsules Constructed From 10% Cold-Worked 316. Note that the steady-state swelling rates appear to be independent of the stress level.

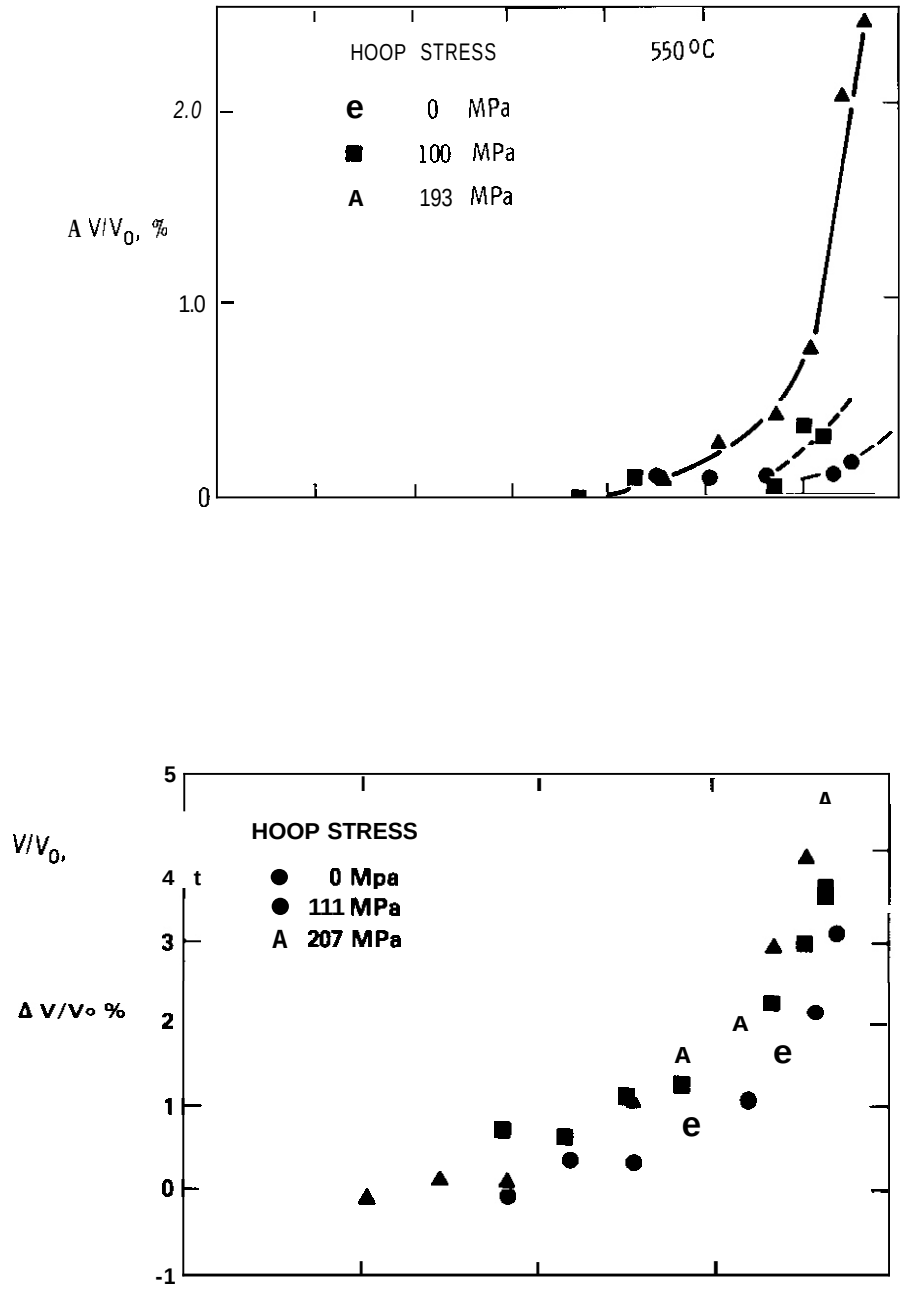

FIGURE 7. Stress-Affected Swelling Observed at 500°C in Long-Tube Capsules Constructed From HTD 316.

model based on incubation behavior can describe the data satisfactorily. Note in Figure 4 that the PEL was probably exceeded for the 10% cold-worked material at 400°C but not at 550°C due to the lower stress levels employed. At 400°C the effect of stress on swelling can be observed at 246-293 MPa even for the inadvertantly cold-worked material.

Table 2 shows that stress-enhanced swelling is a general characteristic of many alloys as long as they are subject to swelling. With the

TABLE 2

IMMERSION DENSITY DATA FROM THE AA-II AND AA-VIII EXPERIMENTS

Alloy*	Temperature (°C)	Fluence 10^{22} n/cm^2 (E >0.1 MeV)	Hoop Stress (MPa)	$-\Delta\rho/\rho_o$ (%)
STA PE16	547	2	0	- .02
STA PE16	547	2	167.3	+ .12
ST PE16	547	2	0	- .60
ST PE16	547	2	167.3	- .12
STA M-813	547	2	0	- .17
STA M-813	547	2	167.3	+ .27
STA 706	547	2	0	- .09
STA 706	547	2	167.3	- .09
ST 706	547	2	0	- .79
ST 706	547	2	167.3	- .91
STA A286**	650	5	0	0.10
	650	5	13.8	0.13
	650	5	55.2	0.17
STA A286**	730	5	0	0.57
	730	5	6.9	0.66
	730	5	13.8	0.74

* STA = Solution treated and aged.
ST = Solution treated only.
CW = 20% cold worked
AU = Solution treated, cold worked and aged.

**This data obtained from the AA-VIII experiment.

exception of Inconel 706, which resists swelling at the fluences investigated, all alloys listed exhibit enhanced swelling. Note that most alloys densify prior to the initiation of void swelling. Figures 8-10 show evidence that the enhancement process observed in several alloys at low fluence continues at higher fluences. Once again the enhancement occurs for a variety of metallurgical starting conditions.

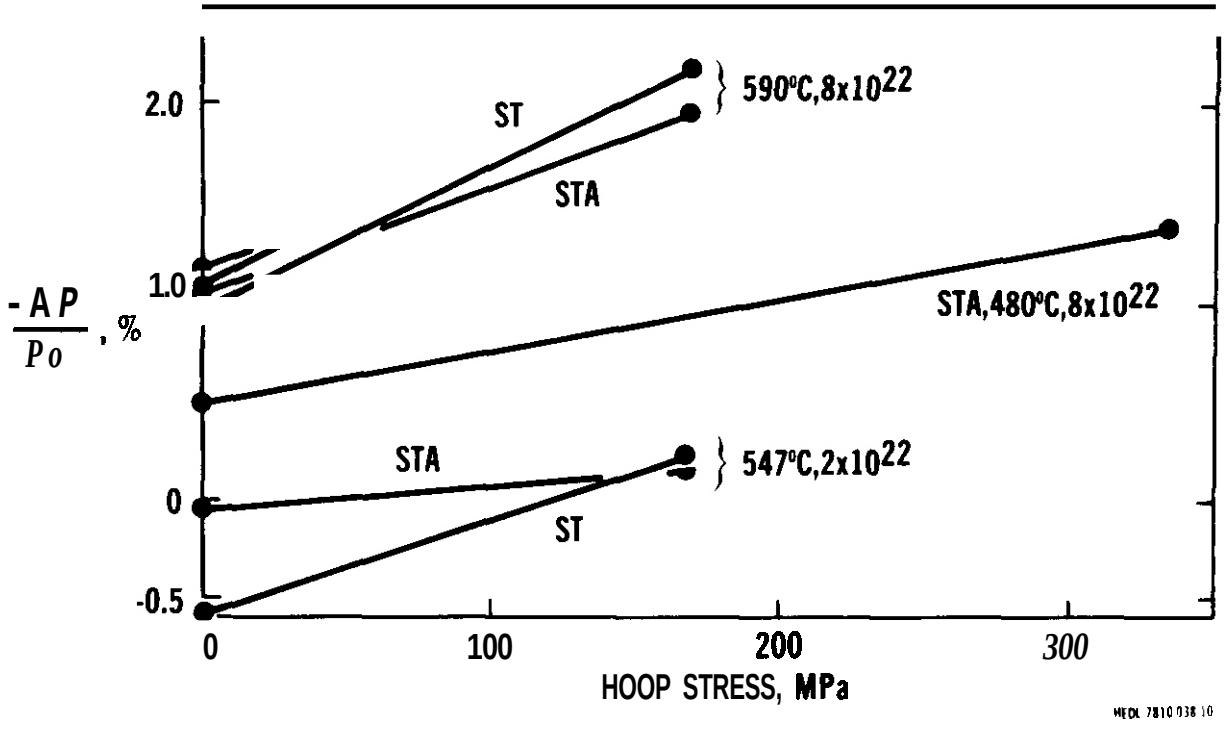

FIGURE 8. Stress-Enhancement of Swelling Observed in Nimonic PE16 in Both the Solution-Treated and Solution-Treated-and-Aged Condition.

5. Discussion

In an upcoming paper, the full details of the data analysis and swelling correlation development for 20% cold-worked AISI 316 will be presented. In this report it will suffice to show that the trend shown in Figures 5-7 was confirmed by independent analyses of the data shown in Figures 1-3. In other words, the primary effect of stress is manifested in the incubation period and not the steady-state swelling rate. This explains why an earlier experiment showed that, once stress had exerted its influence on swelling, removal of the stress during subsequent additional irradiation did

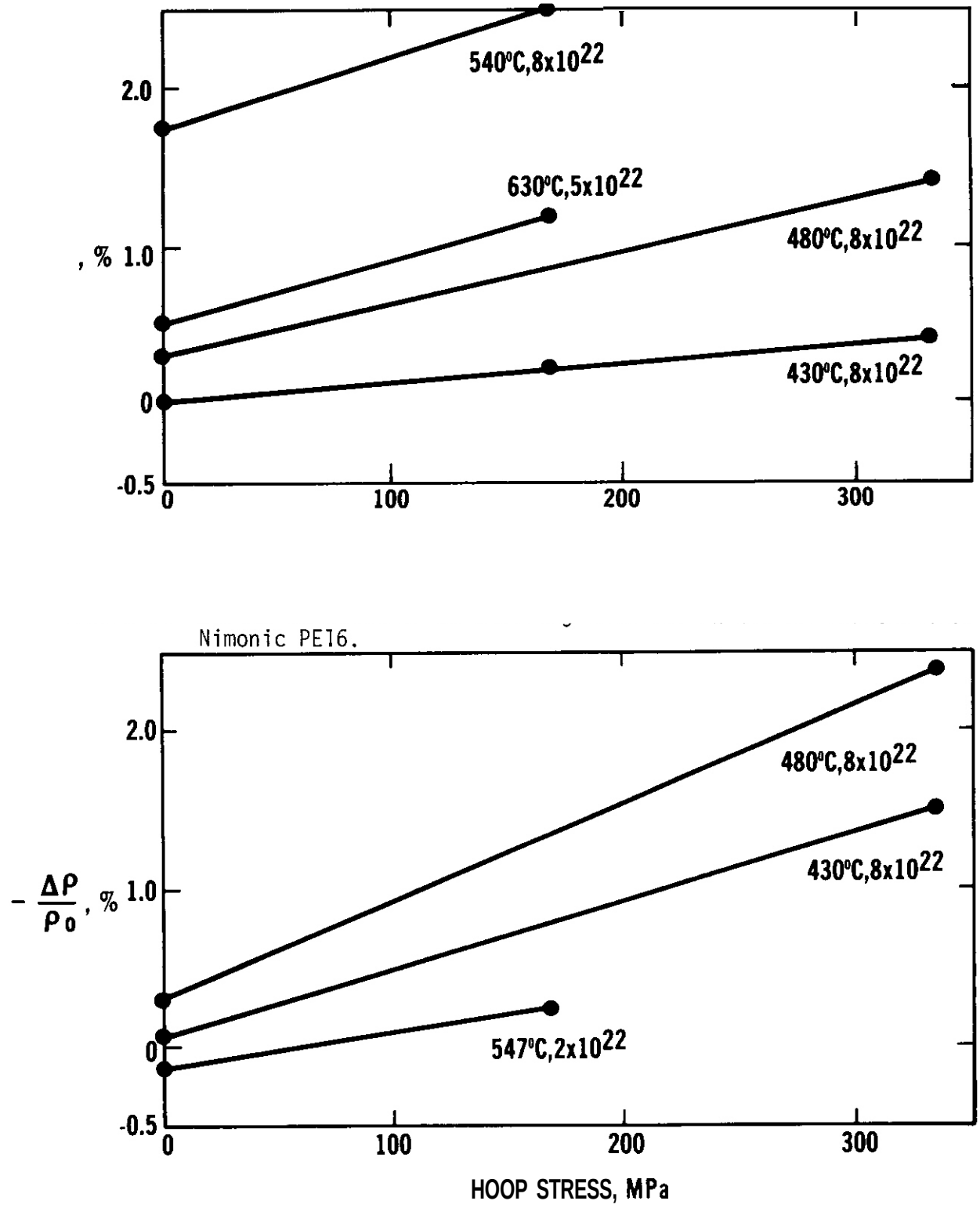

FIGURE 10. Stress-Enhancement of Swelling Observed in the Solution-Treated and-Aged Condition of M813.

not lead to a decrease in the swelling rate.[13]

As shown in Figure 11, there are two approaches traditionally employed in the empirical modeling of stress effects on swelling. Stress is assumed to operate on either the incubation parameter τ or the steady-state swelling rate R according to the relations:[14-15]

$$R(T, \sigma_H) = R_o(T)(1 + p\sigma_H) \quad (1)$$

$$\tau(T, \sigma_H) = \tau_o(T) - q(T)\sigma_H \quad (2)$$

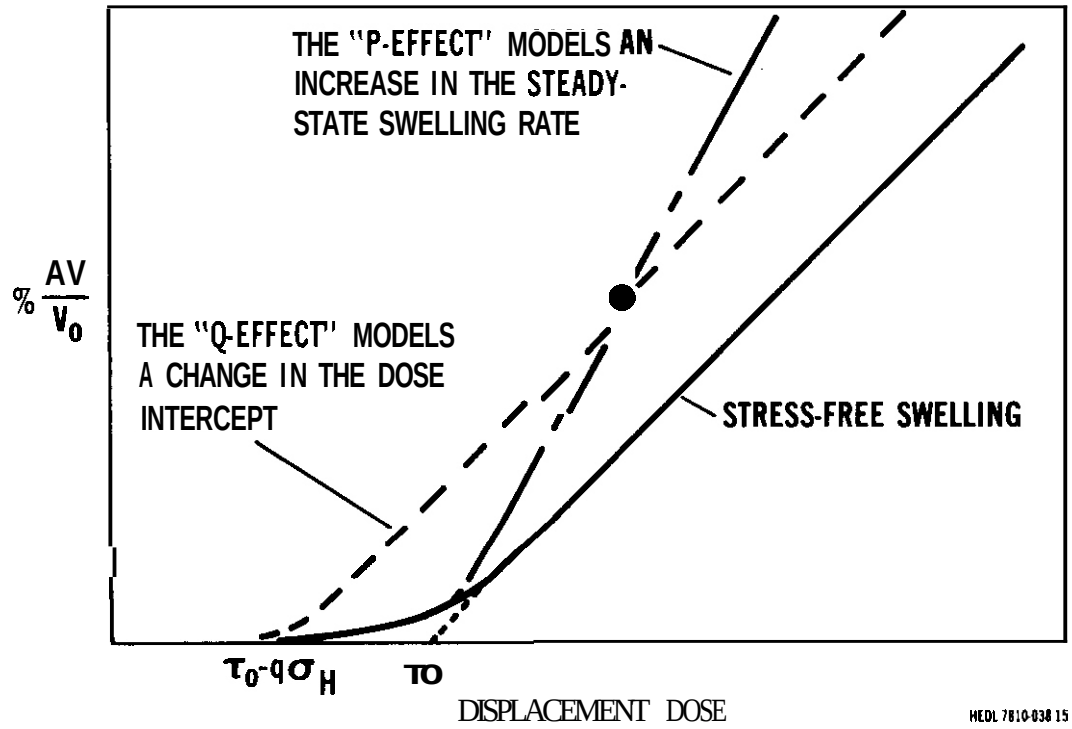

FIGURE 11. Schematic Representation of the Proposed Models of Stress-Enhanced Swelling.

where σ_H is the hydrostatic stress, T is the temperature and the subscript on R and τ refers to the stress-free values. Both p and q were assumed to be dependent on temperature. The analysis shows not only that the p-approach will not lead to a consistent correlation, but that the q-approach yields values of q(T) that are essentially independent of heat identity in the

temperature range where the data for each heat overlap. This is quite surprising since the stress-free incubation parameters are quite different for the two heats of steel. As shown in Figure 12, however, the incubation

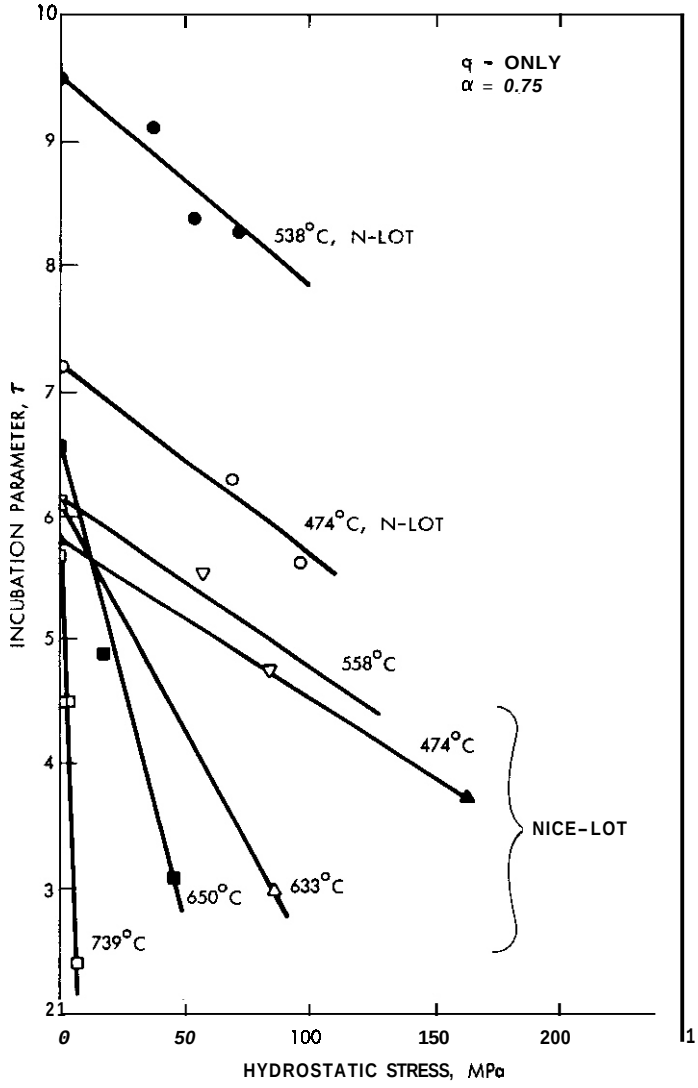

FIGURE 12. Values of Incubation Parameter $\tau(T,\sigma_H)$ Required to Fit Data of Figure 1 Assuming That a q-Approach is Sufficient to Model the Enhancement by Stress of Swelling of AISI 316 in the 20% Cold-Worked Condition.

parameters $\tau(T,\sigma_H)$ derived from some of the short tubes exhibit progressively steeper slopes (q) with increasing temperature. Note from Figure 13 that the effect of stress is essentially constant at low irradiation temperature and

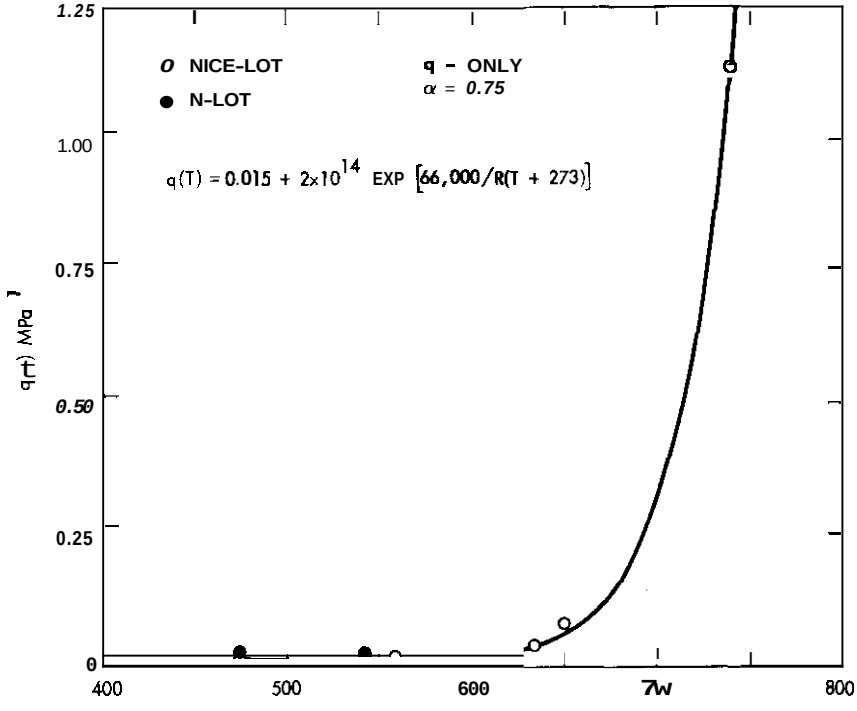

then accelerates sharply above 600°C. Analysis of the long-tube data on 10%cold-work material yields q(T) values in close agreement with the correlation shown in Figure 13.

From the behavior of q(T) with temperature, it is inferred that more than one physical mechanism is operating. Whereas most previous stress-affected swelling positions (both theoretical and empirical) postulated that stress could only affect swelling at relatively high temperature, the low temperature regime exhibits a stress-effect with little or no temperature dependence. It has been demonstrated that such a result could arise from stress-induced changes in the interstitial capture efficiency of voids.(16) This mechanism is only weakly dependent on temperature and is of the appropriate magnitude to account for the enhancement of void nucleation observed in previously published data at 500°C.(1) It was also shown that the evolution of Frank loops is affected by stress and that this leads

to an acceleration of the radiation-induced microstructure. This mechanism would tend to accelerate swelling by shortening the incubation period and would also exhibit a weak dependence on temperature.[1,16] This mechanism is not expected to be important in cold-worked steel, however, since the pre-irradiation dislocation microstructure exists at levels comparable to that produced by radiation.

In the high-temperature regime the derived activation energies are on the order of the self-diffusion energy. This is consistent with the often-predicted high temperature swelling mechanism,[17-18] sometimes referred to as "breakaway swelling." This mechanism arises because stress can affect those microstructural components which can do work against the applied stress by emitting vacancies and climbing, thus changing the equilibrium vacancy concentration at dislocations, particularly for small voids. This reduces the rate of vacancy flow from small voids to dislocations, thereby increasing the stability of voids against dissolution. In the results shown here, however, breakaway swelling did not occur, nor would it be expected to occur for a phenomenon associated only with incubation behavior. Note, however, that the data in Figure 3 were not available at the time that the analysis shown in Figure 13 was completed and that the data at 739°C (Figure 3) appear to foreshadow the onset of break-away swelling at very low stresses. To investigate this possibility microstructural examinations were conducted on these specimens. It was found that the swelling observed was not caused by voidage or microcracks (associated with the very large creep strains in these high temperature specimens) but arose from an enhancement by stress of the rate of formation of intermetallic phases. These phases form at relatively high temperatures and lead to a new dilation of the steel which is small and saturable. Below 700°C the intermetallic contribution is expected to be small. Other phases such as γ' [3] and carbosilicides [19-20] that form at low temperatures have been found to be insensitive to applied stress.

This latter phenomenon poses some problems in extrapolation of these data to other stress states. Since the appropriate stress parameter for the other three mechanisms is the hydrostatic stress,[16] one would

predict that compressive stresses would extend the incubation period and reduce swelling. If stress accelerates the development of intermetallic phases, it will also accelerate the onset of the infiltration-exchange process which governs the swelling behavior in the temperature regime where these phases form.[19-20] It is quite possible that these phases are accelerated by the shear stresses inherent in the biaxial stress state. Stress-affected swelling correlations based on such a possibility would then be of a different form:

$$\tau(T,\sigma) = \tau_o(T) - q_1(T)\sigma_H - q_2(T)|\sigma_{eq}| \qquad (3)$$

where σ_{eq} is the equivalent stress

It appears, therefore, that the effect of stress on swelling is a transient one, which is not repeated when the stress is removed. Stress is therefore a variable of only second-order importance when compared to the microchemical segregation processes which dominate the incubation behavior of AISI 316.[19-20] This point of view is confirmed by the data of Flinn[21] which shows that, when the stress-free incubation period is relatively short as in annealed AISI 304L, the application of moderate stress does not change incubation substantially, but can accelerate the curvature of the swelling correlation at higher stress levels. Such an explanation requires that a microchemical evolution be proceeding in 304L steel in a manner comparable to that occurring in 316 stainless steel. Porter[22] has recently shown that acceleration of swelling of the 304L alloy is coincident with a substantial microchemical evolution, although the details of the phase development are quite different in the two alloys.

The apparent inconsistency of earlier conclusions concerning stress-affected swelling can now be addressed in terms of the insight gained in this study. Most studies based on fuel pin cladding have been inconclusive, primarily because the irradiation conditions are either too complicated or poorly defined to allow a definitive statement of the role of stress. Fuel pins generally operate with low initial levels of stress

that increase with fluence due to accumulating fission gas pressure; thus the stress becomes large only after void incubation is over. The data of Flinn, McVay and Walters shown in Figure 14 fall into this category.[6] (It should also be noted that the capsule and cladding material are different heats of steel and the large difference in swelling behavior at 530°C probably reflects the large differences in their respective manganese and nickel levels.) When the stresses are large due to fuel-clad interaction, the stress levels are relatively indeterminate.

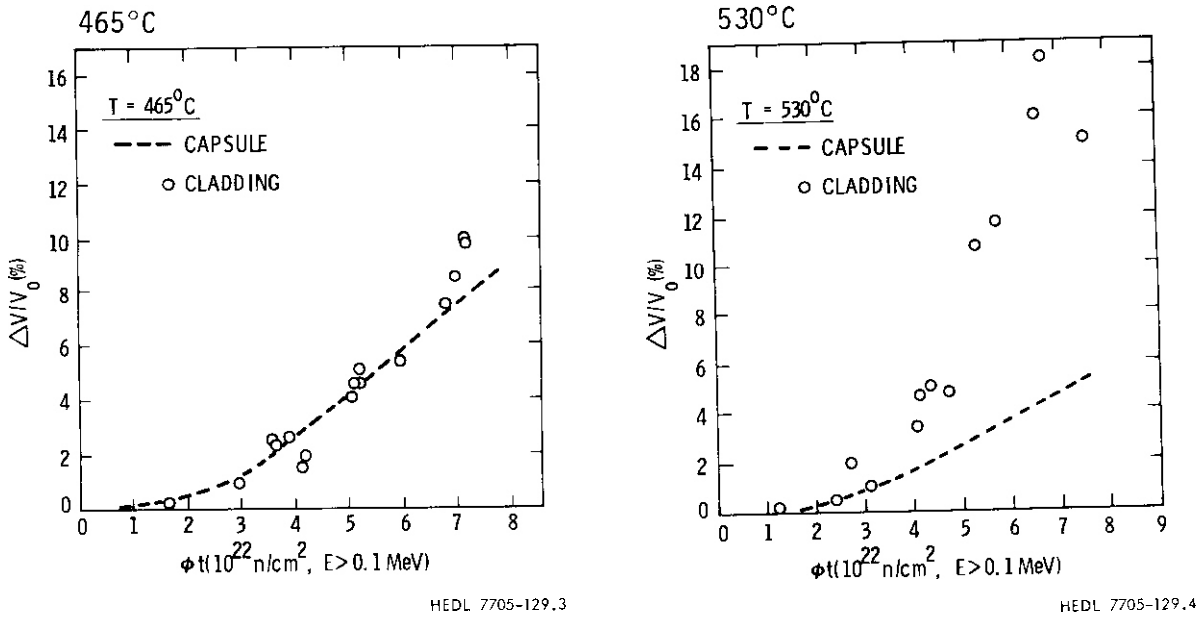

FIGURE 14. Swelling Observed in Type 304L Stainless Steel Capsule and Cladding Material at 465 and 530°C.[6] The apparent effect of stress on the swelling rate is due not only to the fact that the stress operating on the cladding is very low at fluences where voids are formed but also that two different heats of steel with significant differences in composition were employed to construct the capsule and cladding.

The data of Dupouy, Lehman and Boutard[5] shown in Figure 15 are in agreement with our results in that the effect of stress on swelling is visible but small at temperatures below 510°C, however. Note that in agreement with this study and that of Bates and Gilbert,[4] the effect of stress on swelling operates on both annealed and cold-worked steel. The data of Bergman and coworkers[23] are judged to be inconclusive.

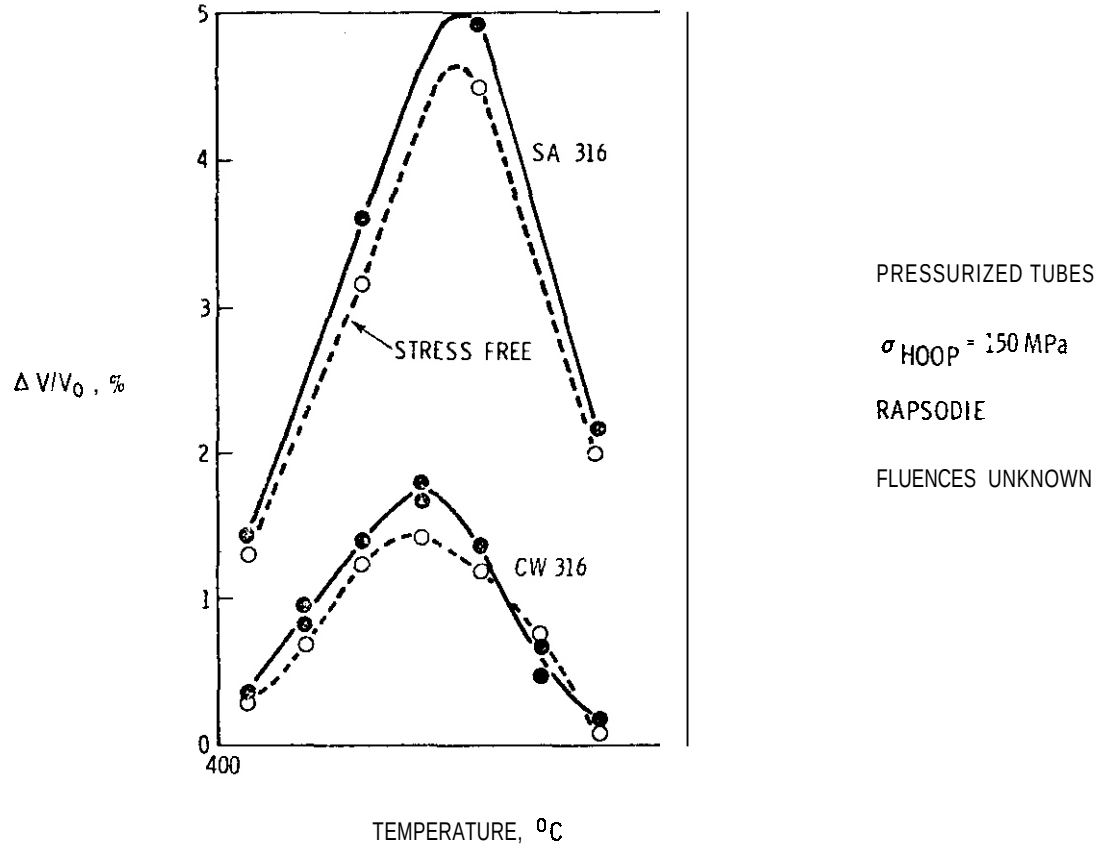

FIGURE 15. Stress-Affected Swelling of AISI 316 Observed in the Rapsodie Reactor [5] at 150 MPa. The swelling peaks due to a flux profile across the reactor.

The two earliest data sets on stress-effects lead various researchers to the conclusion that such a phenomenon did not exist. [6-7] Those data sets are shown in Figures 16 and 17. In fact it appears that stress may actually decrease swelling somewhat. With hindsight it is now possible to reconcile these inconsistencies. Solution-annealed 304L has a very short stress-free incubation period and the irradiation temperatures in these studies were very low. This makes it difficult to observe an incubation-related phenomenon. More importantly, however, the single stress level investigated was in excess of the proportional elastic limit of the material. [12] In other words, these curves compare annealed and cold-worked steel.

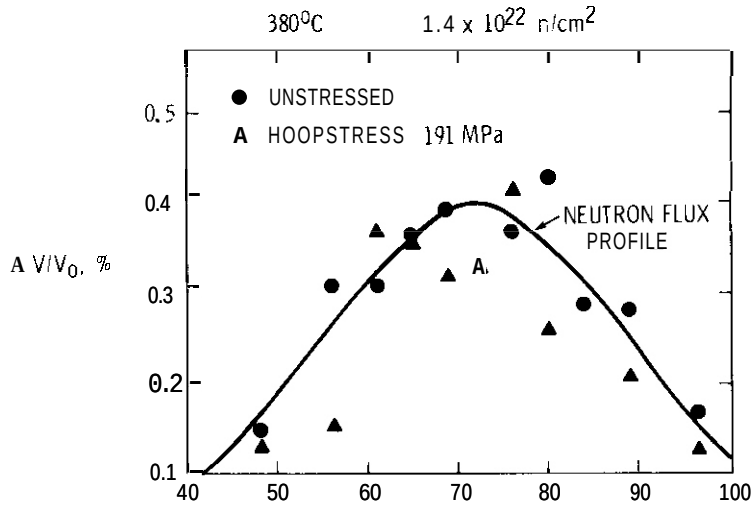

FIGURE 16. Swelling Observed in 304L Creep Capsules Irradiated to 1.4 x 10^{22} n/cm^2 at 380°C.(7)

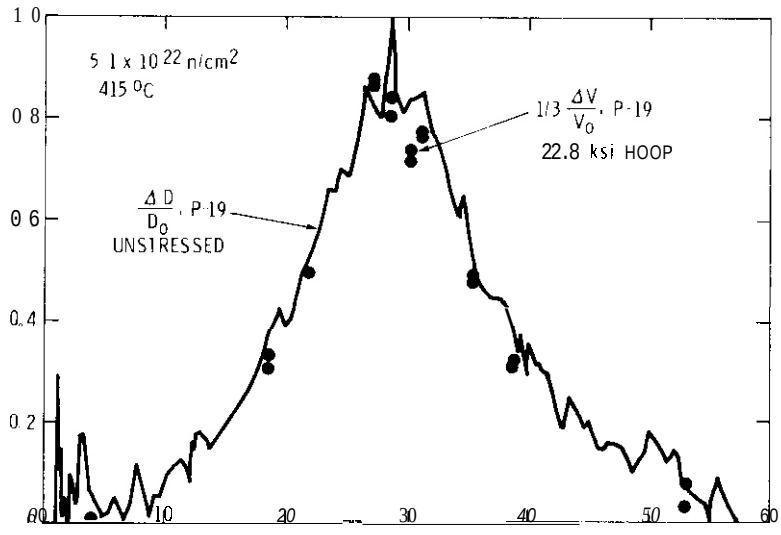

FIGURE 17. Swelling Observed in 304L Creep Capsule Irradiated to 5.1 x 10^{22} n/cm^2 at 415°C.(6)

6. Conclusions

The primary effect of applied tensile stress on swelling appears to be a decrease in the incubation period preceding the onset of steady-state swelling. Stress-affected swelling appears to occur in all alloys and alloy starting conditions which are subject to swelling, although it is difficult to observe in materials with short incubation periods, particularly at low temperature. Levels of stress which exceed the yield stress of the alloy at the irradiation temperature lead to inadvertant cold working, which also can obscure the effect of stress on swelling. Stress-affected swelling spans the entire temperature range applicable to fast reactors but it appears that more than one mechanism is involved, one which dominates at relatively low temperature and another which controls at higher temperatures. Although the influence of stress is greatest at higher temperatures, it appears that other phenomena such as stress-affected precipitation may also be reflected in the density change data attemperaturesabove 700°C. Until the factors which control stress-affected precipitation of intermetallics and the subsequent acceleration of the microchemical evolution are fully understood, extrapolation of these data to compressive stress states is fraught with uncertainty.

VI. REFERENCES

1. H. R. Brager, F. A. Garner and G. L. Guthrie, J. Nucl. Mat., 66, 301-321, 1977.

2. F. A. Garner and W. G. Wolfer, Transactions, American Nuc. Soc., 1978, p. 144.

3. D. S. Gelles, F. A. Garner and H. R. Brager, "Frank Loop Formation in Irradiated Metals in Response to Applied and Internal Stresses," Effects of Radiation on Materials, ASMT STP 725, D. Kramer, H. R. Brager and J. S. Perrin (Eds) ASTM (in press).

4. J. F. Bates and E. R. Gilbert, J. Nucl. Mat., 59, p. 96, 1975.

5. J. L. Boutard. G. Brun, J. Lehman, J. L. Seran and J. M. Dupouy, "Swelling of 316 Stainless Steel," Proceedings of Inter. Conf. on Irradiation Behavior of Metallic Materials for Fast Reactor Compo-&, June 1979, in press.

6. J. E. Flinn, G. L. McVay and L. C. Walters, J. Nucl. Mat., 65, p. 210-213, 1977.

7. L. C. Walters and J. E. Flinn, J. Nucl. Mat., 52, 1974, p. 112-114.

8. M. M. Paxton, B. A. Chin, E. R. Gilbert and R. E. Nygren, J. Nucl. Mat., 80, 1979, p. 144-151.

9. G. L. McVay, R. E. Einziger, G. L. Hoffman and L. C. Walters, J. Nucl. Mat., 78, 1978, 201-209.

10. J. F. Bates and M. K. Korenko, "Empirical Development of Irradiation-Induced Swelling Design Equations," Nuclear Technology, 48, 1980, p. 303.

11. F. A. Garner, W. V. Cummings, J. F. Bates and E. R. Gilbert, "Densification-Induced Strains in 20% Cold-Worked 316 Stainless Steel During Neutron Irradiation," HEDL-TME 78-9, November 1971.

12. J. M. Steichen, "High Strain Rate Mechanical Properties of Types 304 and 316 Stainless Steel," HEOL-TME 71-164, November 1971.

13. J. E. Flinn and T. A. Kenfield, Workshop for Correlation of Neutron and Charged Particle Damage, Oak Ridge, TN, June 8-9, 1976, CONF-76-673.

14. W. G. Wolfer, M. Ashkin and A. Boltax, "Creep and Swelling Deformation in Structural Materials During Fast-Neutron Irradition," Properties of Reactor Structural Alloys After Neutron or Particle Irradiation, ASTM STP 570, American Society for Testing and Materials, 1975, pp. 233-258.

15. R. A. Weiner and A. Boltax, J. Nucl. Mat., 68, p. 141, 1977.

16. F. A. Garner, W. G. Wolfer and H. R. Brager, "A Reassessment of the Role of Stress in Development of Radiation-Induced Microstructure," ASTM STP 683, p. 160-183.

17. F. A. Garner, W. G. Wolfer, A. Biancheria and A. Boltax, "The Effect of Stress on Radiation Induced Void Growth," Proceedings, Inter. Conf. on Radiation-Induced Voids in Metals, Albany, NY, 1971, p. 841.

18. A. O. Brailsford and R. Bullough, J. Nucl. Mat., 69 and 70, 424, 1978.

19. H. R. Brager and F. A. Garner, "Analysis of Radiation-Induced Microchemical Evolution in 300 Series Stainless Steels," Proc. Symposium on Advanced Techniques-for the Characterization of Irradiated Materials, Las Vegas, NV, March 1980, in press, also HEDL-SA-1883.

20. H.R. Brager and F. A. Garner, "Microchemical Evolution of Neutron Irradiated 316 Stainless Steel," ibid ref. 3.

21. J. E. Flinn, M. M. Hall, Jr. and L. C. Walters, "Influence of In-Reactor History on the Swelling of Type 304L Stainless Steel Fast Reactor Fuel Cladding, submitted to J. Nucl. Mat.

22. D. L. Porter and E. L. Wood, "Ferrite Formation in Neutron-Irradiated Type 304 Stainless Steel, J. Nucl. Mat., 83, p. 90, 1979.

23. H. J. Bergmann, G. Knoblauch, D. Haas and K. Herschbach, "Examinations of Swelling and Irradiation Creep on the Austenitic Stainless Steel Nr. 1.4981 CW," ibid. ref. 5.

VII. FUTURE WORK

This effort will continue as additional data and insight become available. The application of these data to compressive and cyclic stress states will be considered.

I. PROGRAM

Title: Effects of Irradiation on Fusion Reactor Materials
Principal Investigators: F. V. Nolfi, Jr. and A. P. L. Turner
Affiliation: Argonne National Laboratory

II. OBJECTIVE

The objective of this work is to determine the microstructural evolution, during irradiation, of first-wall materials with special emphasis on the effects of helium production, displacement damage and rates, and temperature.

III. RELEVANT DAFS PROGRAM PLAN TASK/SUBTASK

SUBTASK II.C.2.1 Mobility, Distribution, and Bubble Nucleation

IV. SUMMARY

The dose and temperature dependence of cavity formation in a 9Cr-1Mo ferritic alloy irradiated simultaneously with Ni^+ and He^+ has been studied with TEM. Comparison is made to parallel experiments on He-preinjected and Ni^+ ion-irradiated material. For dual-ion irradiation, both intergranular and intragranular cavities formed at all temperatures (450-600°C) and doses (5-25 dpa) investigated. The size of the intergranular cavities increased with increasing temperature, while the size of intragranular cavities decreased. In preinjected samples, cavities formed only at the lowest (450°C) irradiation temperature. For 450°C single-ion irradiation and for 450 and 550°C dual-ion irradiation, there was a correlation between subgrain size and maximum cavity size, suggesting that the boundaries of the small (typically ~ 0.5 μm) subgrains act as the primary defect sink.

V. ACCOMPLISHMENTS AND STATUS

A. Dose and Temperature Dependence of Cavity Formation in Single and Dual-Ion Irradiated 9Cr-1Mo Ferritic Alloy

-- G. Ayrault

1. Introduction

A major question in the irradiation response of candidate fusion reactor structural materials is the influence of concurrent displacement damage and helium production. Dual-ion irradiation, using heavy ions for damage production and helium ions to simulate gas production by transmutation events, provides a means of investigating such effects in the absence of a high energy neutron source.

This report presents preliminary results on the dose and temperature dependenceof cavity formation in preinjected single-ion and dual-ion irradiated samples of a 9Cr-1Mo ferritic alloy.

2. Sample Preparation

The material used in this study was from heat no. CE-3177 of a 9Cr-1Mo ferritic alloy developed by Combustion Engineering; the composition is shown in Table 1. The as-received material was in the form of 0.010-in. sheet, and had been previously tempered for 1 hour at 760°C to yield a tempered martensite structure. Discs 3mm in diameter were punched from the sheet and electropolished prior to irradiation.

Table 1. Alloy composition (wt. %)

C	Mn	Si	S	P	Cr	Mo	V	W	Nb	Ti	Ni
0.087	0.44	0.17	0.01	0.012	9.50	0.78	0.14	0.48	0.11	0.04	0.08

Following irradiation in the ANL Dual-Ion Irradiation Facility, the samples were electrochemically sectioned to a depth of 4500 Å (peak damage was at 5500 Å) in a perchloric acid ethanol solution at -60°C, and then backthinned to perforation in a jet polisher with a perchloric acid, methanol, ethylene glycol monobutyl ether solution at -20°C. A problem encountered in the sample preparation was that during the backthinning, carbide precipitates tended to fall out of the samples, leaving holes which caused the jet polisher to shut off prematurely, at a stage where the samples were too thick for TEM inspection. Further polishing, using manual instead of automatic control of the jet polisher, generally yielded high quality foils.

3. Irradiation Conditions

In both the dose dependence and temperature dependence studies, two sets of samples were irradiated. One set of samples was preinjected with 15 appm ^{3}He and single-ion irradiated with 3.0 MeV $^{58}Ni^{+}$. The other set was dual-ion irradiated with 3.0 MeV $^{58}Ni^{+}$ and 0.83 MeV degraded $^{3}He^{+}$ at a helium injection rate of 15:1, appm He:dpa. The dose dependence samples were irradiated at 500°C, which was expected to be near the peak swelling temperature for our 4×10^{-3} dpa $\cdot$ s^{-1} dose rate, based on other ion irradiations of ferritic alloys;[1,2] the doses were 5, 10 and 25 dpa for both the single- and dual-ion irradiations. In the temperature dependence study all samples were irradiated to a 25 dpa dose at 450, 500, 550 and 600°C at a 3×10^{-3} dpa $\cdot$ s^{-1} dose rate.

4. Preirradiation Microstructure

The most prominent microstructural feature in both unirradiated (Fig. 1a) and irradiated (Fig. 1b) samples was the small (typically ~ 0.5 μm) subgrain size. Moire' fringe patterns at low-angle subgrain boundaries were very common — all images contained a number of subgrains, and careful inspection showed moire' fringes on one or several

boundaries in almost every micrograph, e.g. see Fig. 2a and Fig. 4 b, c and d. The intergranular dislocation density was generally quite low — many subgrains in strong contrast showed no dislocation contrast at all — however, this was often obscured by much higher dislocation densities at subgrain boundaries lying at small angles to the foil surface. This made the dislocation density appear very inhomogeneous in some images.

Another feature common to all samples was the presence of spheroidal carbides. These ranged from ~ 0.05 to 0.2 μm in diameter, and most were clearly located at subgrain boundaries. In fact, all the carbides may have been located at subgrain boundaries, even though some appeared to be intragranular because not all boundaries were visible, particularly those nearly parallel to the foil surface. The carbides were identified as $M_{23}C_6$ from diffraction patterns. Small (typically ~ 150 Å) intragranular precipitates were visible in some grains, but have not yet been identified, e.g. see Fig. 4d. Unlike the large intergranular $M_{23}C_6$, the small intragranular precipitates were not visible in absorption contrast; since visibility conditions have not been established it is not yet clear how high the precipitate density actually was.

We emphasize that for both unirradiated and irradiated samples it is very difficult to define a "typical" microstructure, particularly in high magnification micrographs. The small subgrain sizes made it very difficult to achieve consistent diffraction conditions. In addition, the microstructure tended to vary depending on subgrain size, and the appearance of nominally similar microstructures could vary depending on the orientations of subgrain boundaries. The high magnification micrographs (Figs. 2, 3 and 4) included in this report were selected to emphasize particular points, mainly the cavity formation behavior, but are not intended as "typical" micrographs.

5. Dose Dependence

Samples that were dual-ion irradiated at 500°C to 5, 10 and 25 dpa all exhibited some cavity formation (Fig. 2.) The cavities observed in each sample ranged in size from a dose-dependent maximum (~ 35 Å at 5 dpa, ~ 70 Å at 10 dpa and ~ 90 Å at 25 dpa), down to a practical resolution limit of ~ 20 Å ; it is quite likely that smaller cavities are also present. Preferential formation of cavities at dislocations within grains, and also at subgrain boundaries and the surfaces of $M_{23}C_6$ precipitates, was observed at all doses. Cavities at boundaries were generally higher in number density and smaller than those within grains, and difficult to see in Fig. 2, except in the 25 dpa sample (Fig. 2c.) As the cavity size increased with dose, so did the apparent cavity number density. This may be due to the growth of small cavities into the visible range, and therefore does not necessarily reflect continued cavity nucleation beyond the lowest (5 dpa) dose.

The total cavity volume observed in these samples was within a range where all cavities may have been equilibrium or overpressured helium bubbles. An interesting feature of the cavity distribution is that there was a correlation between maximum cavity size and subgrain size - the largest subgrains usually contained the largest cavities and many small subgrains apparently contained no cavities at all. Also, the largest cavities tended to be located near the centers of grains. Thus, if the cavities are indeed helium bubbles, it appears that the subgrain boundaries act as a dominant sink for the helium. Within grains, dislocations also act as sinks, and Lower densities of larger cavities are formed.

In samples which were preinjected and single-ion irradiated to doses of 5, 10 and 25 dpa at 500°C, no cavities were observed. The irradiation microstructure was otherwise similar to the dual-ion microstructure.

6. Temperature Dependence

The temperature dependence study described below represents a second step in our investigation of cavity formation in single- and dual-ion irradiated ferritic alloys. The irradiations were performed after the dose-dependence samples had been inspected in TEM; it was thought that the very low swelling observed in the dose dependence experiment might be due to the 500°C irradiation temperature falling outside the rapid swelling regime for this alloy. Although the swelling remained low at all temperatures (450-600°C), our surmise proved correct, but in a surprising way. Based on other ion irradiation studies,[1,2] we expected that if 500°C was not near the peak swelling temperature, that higher temperatures would produce greater swelling. In fact, there was no swelling increase at higher temperatures (550 and 600°C), but there was an increase at 450°C, which is a very low temperature for swelling under ion irradiation.

A 500°C dual-ion sample (Fig. 3b) was included in the temperature dependence study as an internal check on the consistency of our irradiation conditions. The microstructure was essentially the same as it was in the 500°C, 25 dpa sample from the dose dependence study, with a maximum cavity size of ~ 90 Å in large subgrains, and preferential formation of smaller cavities at subgrain boundaries, as noted previously in section 5. In the 450°C dual-ion sample (Fig. 3a) cavities as large as 150 Å in diameter (the largest found in any sample) were present in large subgrains, in addition to smaller cavities at subgrain boundaries, like those found in the 500°C sample. The intragranular cavity number density appeared to be higher at 450°C, but this may have been due to greater cavity visibility resulting from a larger mean cavity size.

In the 550°C dual-ion sample (Fig. 3c,) the maximum cavity size (~ 608) was smaller than at 500°C, but the cavities at boundaries were about the same size and were generally larger than the cavities at boundaries in the 450 and 500°C samples. In the 600°C dual-ion sample

(Fig. 3d,) the largest cavities (~ 80 Å) were located at boundaries, and intragranular cavities were smaller than those in lower temperature samples. Thus, in the temperature range 450-600°C, a consistent trend toward increases in the size of intergranular cavities and decreases in the size of intragranular cavities was observed.

In helium preinjected and single-ion irradiated samples (Fig. 4,) no cavities were observed in samples' irradiated at 500, 550 or 600°C (Figs. 4b, c and d respectively,) but cavities did form in the 450°C sample (Fig. 4a.) The maximum cavity size (~ 120Å) was smaller than in the 450°C dual-ion sample (~ 150Å) , and small cavities at grain boundaries were apparently absent. However, the formation of the largest cavities in the largest subgrains paralleled the behavior of large cavities under 450°C dual-ion irradiation. The observation of cavities in a single-ion irradiated sample is important since it indicates that the increased cavity size at low temperature is not simply a peculiarity of helium bubble formation, but rather it reflects an unusually low temperature for maximum void swelling. Future irradiations will have to be performed at even lower temperature to define the location of the swelling peak in this material.

7. Discussion

Ferritic alloys are generally considered to be highly resistant to void swelling, but the mechanism for this suppression is not yet understood. This makes irradiation damage studies covering a wide variety of irradiation conditions particularly important, in order to provide assurance that the unknown suppression mechanisms will not be easily bypassed, and also, it is hoped, to identify these mechanisms. Our first concern, at the outset of this study, was that helium bubble formation might bypass a swelling suppression mechanism which was strongly dependent upon suppression of cavity nucleation; the helium bubbles would presumably provide stable void nuclei for subsequent rapid growth.

In this study, rapid growth did not occur, although observable and presumably stable cavities were present in all dual-ion irradiated samples. However, the sluggish cavity growth may have been aided by the high density of subgrain boundaries acting as the primary (and unbiased) sinks for irradiation-induced vacancies and interstitials. Such a swelling suppression mechanism was proposed by Singh[3] to explain a correlation between small grain size and low swelling in a series of austenitic alloys whose grain sizes were controlled by dispersions of aluminum oxide particles; for grain sizes <0.7 μm, swelling was very strongly suppressed. Based on this study, a similar suppression would be expected in the ferritic alloy under study here, since the subgrain size is typically ~ 0.5 μm. The operation of such a mechanism is consistent with our observation, in 450 and 500°C dual-ion and 450°C single-ion samples, of a correlation between subgrain size and cavity size, and the tendency for large cavities to form near the centers of grains. This mechanism also provides at least a partial explanation for the unusually low peak swelling temperatures under both single- and dual-ion irradiation for the following reason: with decreasing temperature the density of radiation-induced dislocations increases, thus decreasing the dominance of the unbiased grain boundary sinks over the biased intragranular dislocation sinks. We would therefore expect swelling suppression due to grain boundaries to be more effective at higher temperatures, and this would therefore cause a downward shift of the peak swelling temperature. It will be interesting to see if this correlation between void swelling and grain size persists in other ferritic alloys with tempered martensite structure.

VI. REFERENCES

1. W. G. Johnston, T. Lauritzen, J. H. Rosolowski and A. M. Turkalo, Report No. 76CRD019 (General Electric Corporate Ressearch and Development, Schenectady, 1976).

2. F. A. Smidt, Jr., P. R. Malmberg, J. A. Sprague and J. E. Westmoreland, ASTM STP 611 (American Society for Testing and Materials, Philadelphia, 1976), p. 227.

3. B. N. Singh, Phil. Mag. 29, 25 (1974).

VII. FUTURE WORK

Samples of undoped and Ni-doped HT-9 and 9Cr-1Mo ferritic alloys are scheduled for single- and dual-ion irradiation in the near future. This study will concentrate upon the temperature dependence of cavity formation in HT-9 (heat XAA-3587), HT9 + 2%Ni (heat XAA-3589), 9Cr-1Mo (heat XA-3590) and 9Cr-1Mo + 2%Ni (heat XA-3591); these heats were prepared by Combustion Engineering. In addition to providing data on the swelling resistance of HT-9, and heat-to-heat variations in 9Cr-1Mo alloys, this study should provide insight into the influence of nickel additions on swelling resistance, and support current reactor irradiation studies on the same materials; in reactor studies the nickel additions provide transmutant helium, whereas for dual-ion irradiation, helium levels are independent of nickel content.

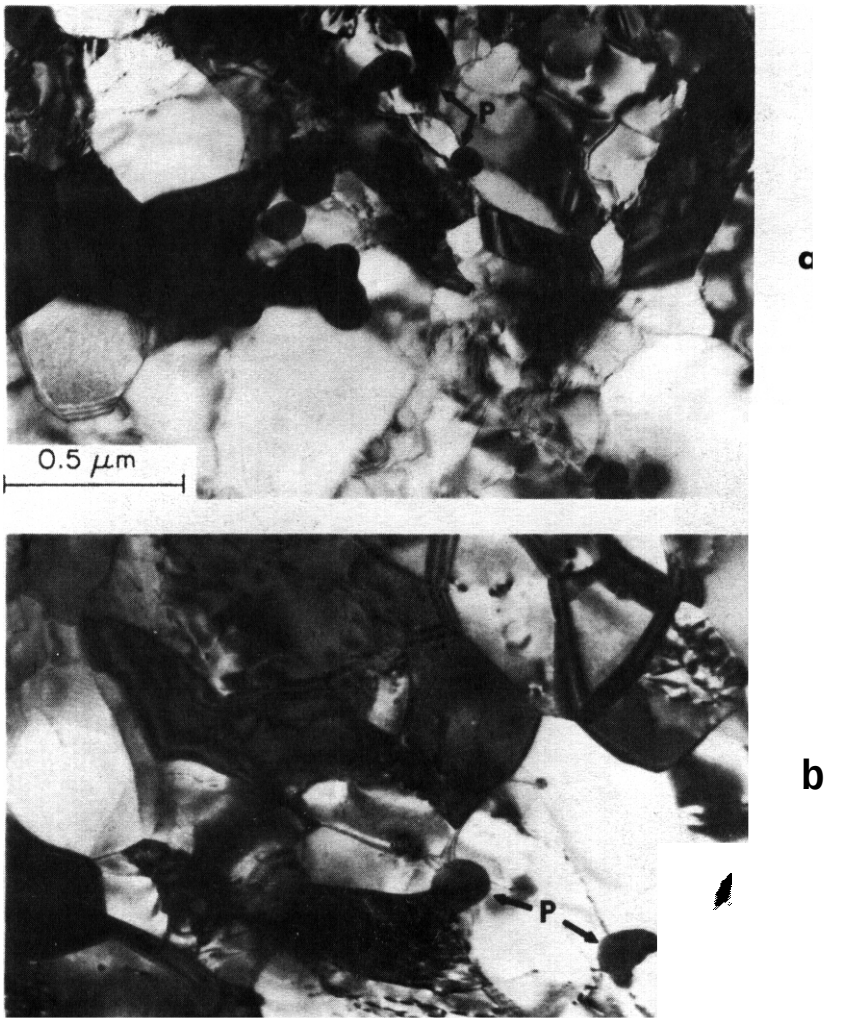

Figure 1 Micrographs showing the subgrain and precipitate structures in 9Cr-1Mo ferritic alloy. The spheroidal precipitates labeled "P" are $M_{23}C_6$. (a) Unirradiated control sample from a 550°C irradiation and (b) sample dual-ion irradiated at 550°C to 25 dpa at 3 x 10^{-3} dpa • s^{-1} with 15:1, appm He:dpa.

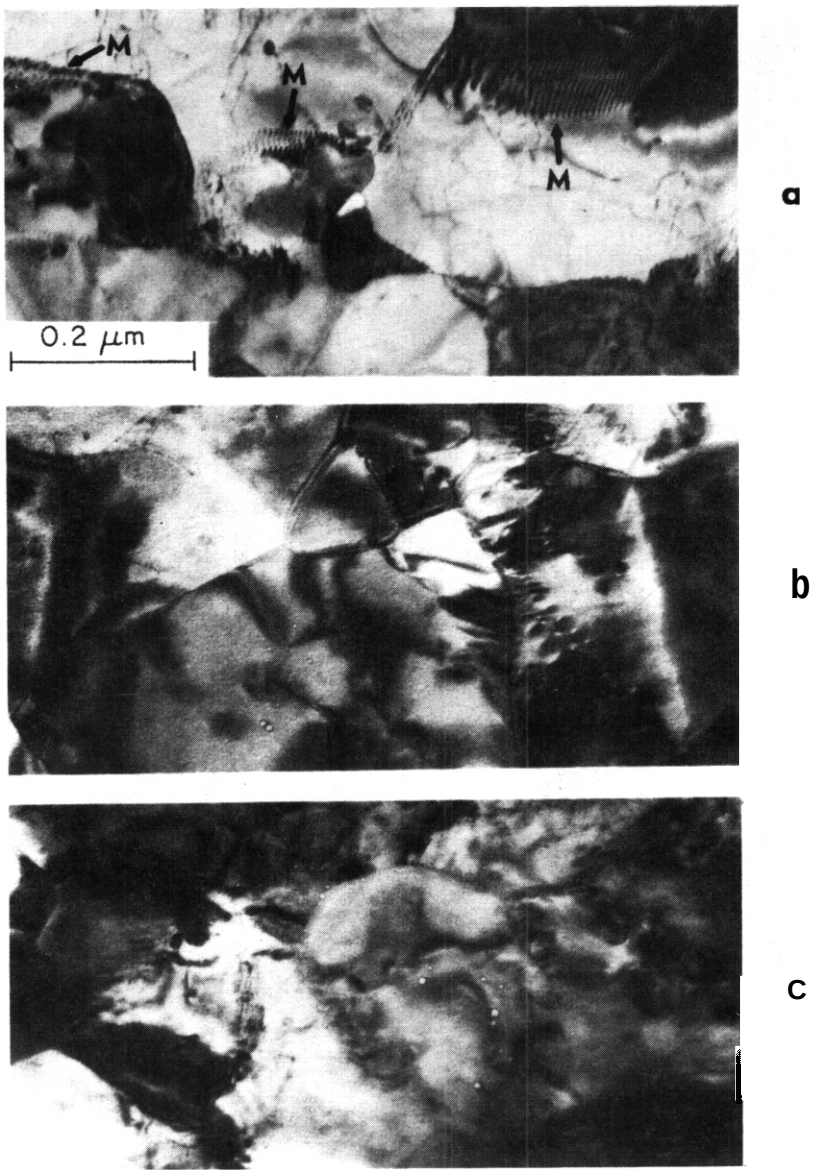

Figure 2. Micrographs showing samples dual-ion irradiated at 4 x 10^{-3} dpa • s^{-1} and 500°C with 15:1, appm He:dpa. The features labeled "M" are moire' fringes at low-angle subgrain boundaries. (a) 5 dpa, (b) 10 dpa and (c) 25 dpa.

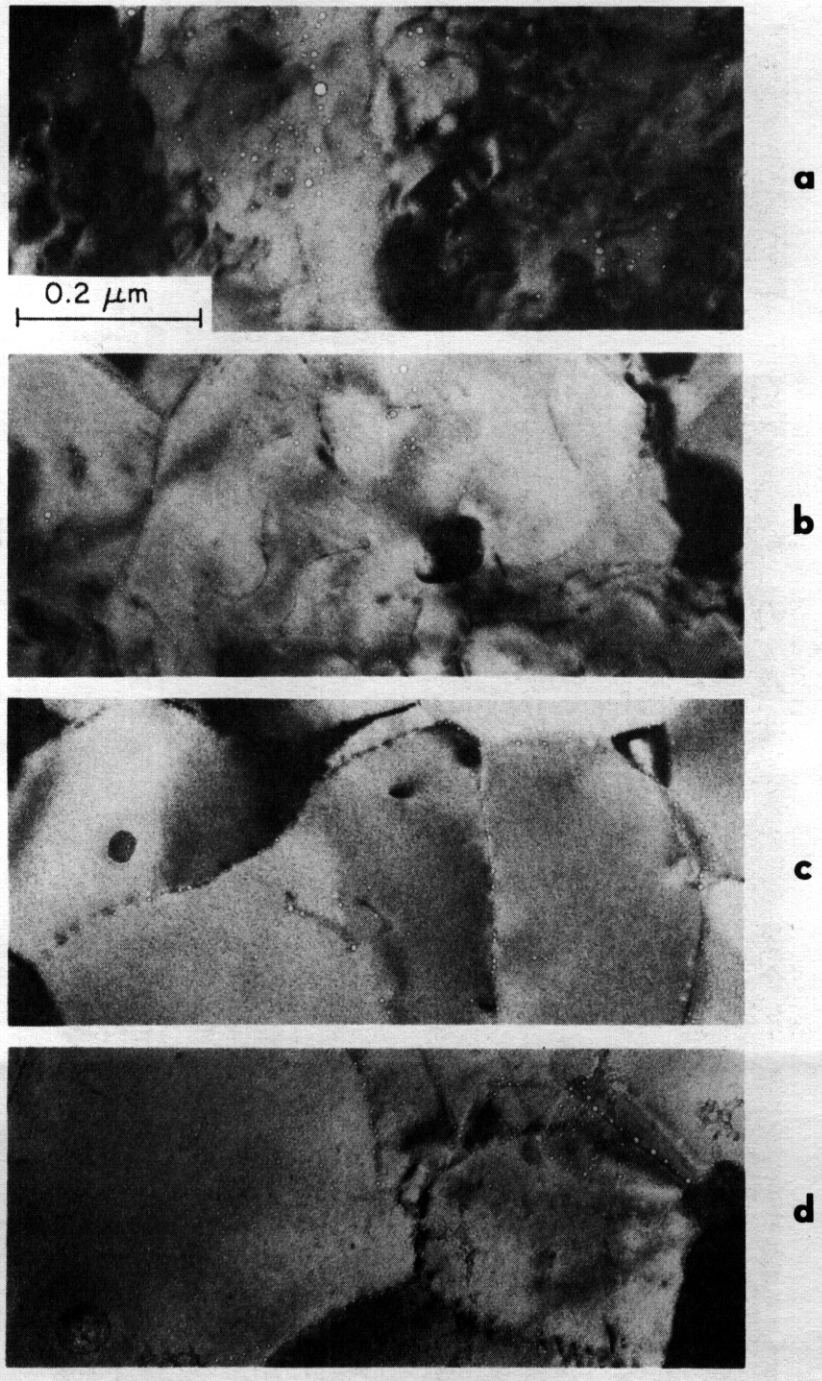

Figure 3. Micrographs showing samples dual-ion irradiated to 25 dpa at 3 x 10^{-3} dpa • s^{-1} with 15:1, appm He:dpa. (a) 450°C, (b) 500°C, (c) 550°C and (d) 600°C.

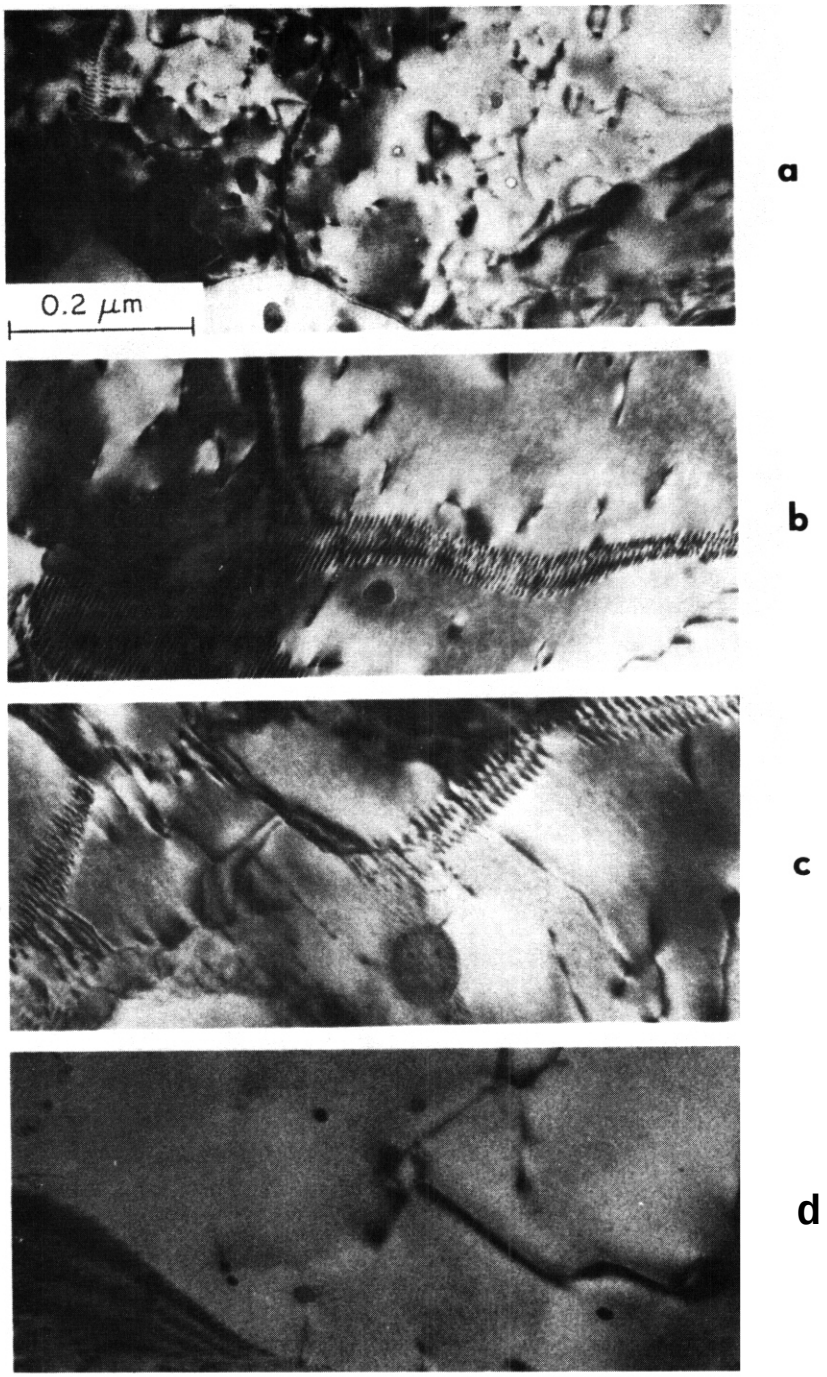

Figure *4.* **Micrographs showing samples which were preinjected with 15 appm He and single-ion irradiated to 25 dpa at** *3* x 10^{-3} **dpa** • s^{-1}. (a) 450°C, (b) 500°C, (c) 550°C and (d) 600°C.

I. PROGRAM

Title: Irradiation Effects Analysis (AKJ)
Principal Investigator: D. G. Doran
Affiliation: Hanford Engineering Development Laboratory

II. OBJECTIVE

The objective of this work is to develop correlation methods for irradiation effects on tensile properties of materials important to magnetic fusion energy devices.

III. RELEVANT DAFS PROGRAM TASK/SUBTASK

Subtask II.C.2.2 Fast spectrum/mixed-spectrum correlations
Subtask II.C.16.1 Correlation model development

IV. SUMMARY

Yield strength data on 20% cold-worked 316 stainless steel irradiated in fast and thermal reactors and by 14 MeV neutrons were analyzed and a ten-parameter equation was developed to describe the yield strength behavior for the temperature range $25 < T < 800°C$. The equation includes the irradiation parameters: displaced atoms, helium content, and irradiation temperature. It is applicable to strain rates $< 5 \times 10^{-4}$/second and test temperatures approximately equal to the irradiation temperature.

V. ACCOMPLISHMENTS AND STATUS

Yield Strength Correlation for 20% CW 316 Stainless Steel - R. L. Simons

Introduction

It is expected that 20% cold-worked (CW) AISI 316 stainless steel will be used in the construction of the Fusion Engineering Device (FED) and possibly later fusion devices. Consequently, a correlation of available data on yield strength of irradiated 20% CW 316 stainless steel was made for the

irradiation temperature range 20°C to 800°C. Ultimate tensile strength, uniform elongation, and total elongation will be addressed in a subsequent report.

There were two primary sources of data--N lots and T lots of heat 87210 used for Fast-Flux Test Facility (FFTF) cladding, and DO heat used in irradiation experiments by Oak Ridge National Laboratory (ORNL). The primary difference between the two heats is the silicon content. Other differences between the data sets are primarily due to differences in the irradiation environment. Materials from the former heat were irradiated in the Experimental Breeder Reactor II (EBR-II) at 370 < T < 800°C and at the Rotating Target Neutron Source II (RTNS-II) at 25°C.[1,2] The latter heat of material was irradiated in the High Flux Isotope Reactor (HFIR) at 55 < T < 680°C.[3,4,5] HFIR produces large concentrations (generally greater than 50 appm) of helium due to the two step nickel (n,α) reaction, whereas the EBR-II reactor produces only small concentrations by one-step (n,α) reactions. Some additional data for a Nb modified AISI 316 stainless steel (M316)[6] irradiated in the Dounreay Fast Reactor (DFR) and on AISI 304 stainless steel[7] irradiated in the Engineering Test Reactor (ETR) were also considered in this analysis. The M316 and 304 data were used to supplement the single data point available between 50 and 350°C. Generally speaking these two materials should show the same fluence and temperature trends, although the magnitude of the changes in tensile properties may be different. It turns out that these two data sets are entirely consistent with the damage exposure behavior of AISI 316. The consistency may be fortuitous; however, Higgy and Hammond[8] simultaneously irradiated annealed 304, 316, and 347 stainless steels at T < 100°C, and similarly found consistent behavior among all three steels.

Data Compilation

The exposure parameter used by Fish et al.[1] in reporting tensile data from irradiations in EBR-II was fluence >0.1 MeV. For application to fusion environments the dose parameter was converted to displaced atoms per atom (dpa). The basis for determining the dpa values were the fluxes and spectrum-

averaged displacement cross sections calculated from results obtained from the EBR-II run 50H and run 75D dosimetry tests.[9,10] The 50H dosimetry was used for the irradiations performed prior to the blanket change (run 56), and the 75D dosimetry was used for the post-blanket change irradiations.

For HFIR tensile data the reported dpa values were used except for those from reference (3). They were high by a factor of two, relative to the other values, because they are based on a 25 eV displacement energy and β = 1.0. For ETR tensile data a 1650 barns/fluence > 1.0 MeV displacement cross section was used. The British data on M316 was reported in terms of the half-Nelson displacement model. These values were reduced by 15%[11] to be consistent with the values for the rest of the data used in this analysis.

It is generally recognized that helium can affect tensile properties. Helium concentrations are reported for the HFIR data. They are based on a semi-empirical equation for helium production in HFIR.[12] No values were reported for the EBR-II data. Consequently, it was necessary to estimate helium concentrations based on helium cross sections determined from the measurements made in EBR-II by McElroy and Farrar.[13] For DFR irradiations, EBR-II core center values were used. This is justified because both reactors are metal fueled and sodium cooled, and thus have similar neutron spectra. Helium concentrations for ETR irradiated specimens were estimated to be one-fourth that predicted for HFIR at the same fluence. The values are probably correct to within a factor of two. The value per unit fluence should be less in ETR than in HFIR because HFIR is a thermal flux trap reactor configuration designed to enhance the thermal neutron flux and, consequently, helium generation rate, whereas ETR is a water-moderated reactor with no thermal flux enhancement.

The other parameters of importance are test temperature and strain rate. All available data were used in this analysis through the temperature range 25°C to 800°C, provided the strain rate was $\leq 5 \times 10^{-4}$/second and the test

temperature was near the irradiation temperature. Most of the data used in this analysis were for a strain rate of 5×10^{-5}/second. There was no obvious strain rate effect in the data used. Higher strain rates are known to increase yield strength at temperatures > 600°C.[14] The data were grouped by irradiation temperature. Each group is identified by the mean temperature of the group. The maximum deviation from the mean of any group was 10°C.

There were a total of 104 data points used in this analysis. Not all of the data were from the same heat or same specimen geometry. Consequently, it would not be prudent to give all the data the same weight in the analysis. Assigning weights to the data to account for material differences is unquestionably arbitrary. Since the largest portion of the data were from N and T lots of heat 87210, this correlation was tailored to this data set by giving it a weight of 1.0 and the other sets lesser weights. This is further justified by the fact that the temperatures are somewhat better known in EBR-II than HFIR. Most of the HFIR data were given a weight of 0.5. One set of 316 data[3] from HFIR showed a high unirradiated yield strength (approximate 280-350 MPa higher than the rest of the data) presumably due to the method of fabrication[4] and was given a weight of 0.125. The 304 and M316 data made up 13% of the total and were given weights of 0.125. The small weight was assigned because the material was either sufficiently different (304) or had different unirradiated properties (M316). The simplicity of the design equations developed in this analysis did not permit accounting for this large variation in yield strength. However, several of these specimens exhibited the same property level as the rest of the specimens after extended damage exposure. This supports the premise that, regardless of the starting point, the stainless steel will eventually reach the same property level.[15] Table I summarizes the yield strength data used in this analysis.

Correlation Equation Development

The correlation equation fit to the data should be as physically based as possible. Traditionally, yield strength is modeled as a sum of incremental changes in yield strength due to various dislocation pinning mechanisms. The correlation equation developed assumed the yield strength was equal to

TABLE I YIELD STRENGTH DATA FOR 20% C.W. 316 STAINLESS STEEL.

TEMPERATURE GROUP (°C)	DPA	HELIUM PER ATOM (APPM)	YIELD STRENGTH (MPa) UNIRRADIATED	IRRADIATED	ASSIGNED WEIGHT
376.	17.7	10.0	531.	807.	1.000
376.	7.0	1.7	531.	765.	1.000
376.	28.8	20.0	531.	889.	1.000
376.	8.7	4.9	531.	821.	1.000
376.	3.4	.9	531.	678.	1.000
376.	15.0	10.0	531.	834.	1.000
376.	43.0	29.0	531.	855.	1.000
376.	43.0	29.0	531.	876.	1.000
420.	3.9	.8	517.	679.	1.000
420.	7.2	1.8	517.	738.	1.000
420.	15.9	8.8	517.	758.	1.000
420.	1.9	.4	517.	574.	1.000
420.	3.6	.9	517.	654.	1.000
420.	7.9	4.3	517.	724.	1.000
420.	19.0	13.0	517.	642.	1.000
468.	17.0	8.8	517.	654.	1.000
468.	3.8	2.5	517.	538.	1.000
468.	75.0	51.0	517.	517.	1.000
468.	37.0	24.0	517.	618.	1.000
468.	45.0	31.0	517.	553.	1.000
515.	1.1	.3	510.	493.	1.000
515.	19.0	13.0	510.	421.	1.000
515.	27.0	18.0	510.	405.	1.000
515.	29.0	19.0	510.	392.	1.000
568.	18.0	12.0	480.	355.	1.000
568.	12.0	7.1	480.	361.	1.000
568.	28.0	19.0	480.	354.	1.000
568.	28.0	19.0	480.	335.	1.000
568.	15.0	7.7	480.	332.	1.000
568.	4.4	3.0	480.	452.	1.000
604.	12.0	7.0	450.	359.	1.000
604.	4.3	3.0	450.	381.	1.000
604.	4.3	3.0	450.	335.	1.000
604.	4.3	3.0	450.	394.	1.000
665.	42.0	28.0	400.	313.	1.000

TABLE I (CONT'D) YIELD STRENGTH DATA FOR 20% C.W. 316 STAINLESS STEEL.

TEMPERATURE GROUP (°C)	DPA	HELIUM PER ATOM (APPM)	YIELD STRENGTH (MPa) UNIRRADIATED	IRRADIATED	ASSIGNED WEIGHT
665.	43.0	29.0	400.	301.	1.000
665.	43.0	29.0	400.	291.	1.000
665.	18.0	12.0	400.	299.	1.000
665.	30.0	20.0	400.	283.	1.000
665.	30.0	20.0	400.	295.	1.000
665.	40.0	27.0	400.	276.	1.000
665.	45.0	31.0	400.	276.	1.000
719.	19.0	13.0	280.	229.	1.000
719.	4.9	3.6	280.	231.	1.000
780.	4.9	3.6	200.	165.	1.000
840.	4.9	3.6	150.	83.	1.000
840.	4.9	3.6	150.	63.	1.000
25.	1.54-004	2.90-003	633.	635.	1.000
25.	1.65-004	3.10-003	633.	636.	1.000
25.	1.74-004	3.30-003	633.	644.	1.000
25.	1.79-004	3.40-003	633.	645.	1.000
25.	3.90-004	7.30-003	633.	644.	1.000
25.	4.80-004	9.00-003	633.	628.	1.000
25.	4.80-004	9.00-003	633.	667.	1.000
25.	4.80-004	9.00-003	633.	660.	1.000
25.	5.00-004	8.50-003	633.	663.	1.000
25.	1.80-003	3.40-003	633.	708.	1.000
25.	2.07-003	3.90-003	633.	735.	1.000
25.	2.13-003	4.00-003	633.	723.	1.000
25.	1.86-003	5.40-003	633.	696.	1.000
55.	4.0	180.0	814.	958.	.500*
55.	8.8	380.0	814.	938.	.500*
55.	10.8	520.0	814.	945.	.500*
285.	7.7	350.0	570.	1000.	.500*
376.	5.0	180.0	556.	779.	.500*
376.	8.0	390.0	556.	955.	.500*
376.	8.8	380.0	556.	611.	.500*
376.	13.6	740.0	556.	594.	.500*
376.	13.6	740.0	556.	688.	.500*
376.	49.0	2900.0	903.	752.	.125*

* DO HEAT OF 316 STAINLESS STEEL.

TABLE I (CONT'D) YIELD STRENGTH DATA FOR 20% C.W. 316 STAINLESS STEEL.

TEMPERATURE GROUP (°C)	DPA	HELIUM PER ATOM (APPM)	YIELD STRENGTH (MPa) UNIRRADIATED	IRRADIATED	ASSIGNED WEIGHT
376.	33.0	2200.0	903.	1014.	.125♦
376.	57.0	3800.0	903.	752.	.125♦
468.	7.2	290.0	536.	481.	.500♦
468.	10.4	500.0	536.	405.	.500♦
468.	11.2	600.0	536.	459.	.500♦
468.	16.8	1020.0	536.	395.	.500♦
468.	54.0	3500.0	848.	499.	.125♦
568.	4.0	105.0	772.	416.	.125♦
568.	15.2	880.0	543.	310.	.500♦
568.	7.2	290.0	543.	296.	.500♦
568.	9.6	440.0	543.	332.	.500♦
568.	11.2	600.0	543.	341.	.500♦
530.	57.0	3300.0	827.	438.	.125♦
604.	1.8	29.0	772.	525.	.125♦
604.	3.2	70.0	772.	510.	.125♦
604.	33.0	2200.0	772.	209.	.125♦
604.	70.0	4500.0	772.	323.	.125♦
604.	60.0	4100.0	772.	324.	.500♦
604.	16.8	1020.0	543.	290.	.500♦
293.	.1	1.0	669.	834.	.125♦♦
293.	.1	1.3	669.	855.	.125♦♦
293.	.3	3.0	669.	827.	.125♦♦
293.	.6	6.0	669.	883.	.125♦♦
293.	1.2	23.0	669.	972.	.125♦♦
293.	2.5	30.0	669.	1014.	.125♦♦
293.	10.2	150.0	669.	1041.	.125♦♦
300.	.8	.4	345.	421.	.125+
300.	2.2	1.1	345.	510.	.125+
300.	2.7	1.4	345.	683.	.125+
300.	5.0	2.5	345.	683.	.125+
300.	6.8	3.4	345.	683.	.125+
300.	8.4	4.2	345.	683.	.125+
300.	14.0	7.0	345.	696.	.125+
300.	16.0	8.0	345.	683.	.125+
300.	43.0	21.0	345.	648.	.125+

♦ DO HEAT OF 316 STAINLESS STEEL.
♦♦ MS16 STAINLESS STEEL.
+ 304 STAINLESS STEEL.

the initial value plus or minus an incremental change in yield strength which depends on damage parameter and irradiation temperature. This assumption appears to work well at lower temperatures (<300°C) but does not work as well at higher temperatures where the yield strength depends on the initial state of the material. Thus, this analysis method is appropriate for a single heat of material. Below 500°C, an irradiation hardening mechanism(s) was evident which shows a tendency to saturate with exposure. Saturation is definitely evident at low temperatures (<300°C) in 304 and M316 stainless steels used in this analysis.

The EBR-II data appear to show a high dose softening in yield strength. This is particularly evident at 470°C . Figure 1-A shows data from irradiations in EBR-II and HFIR. The EBR-II data clearly shows softening at high doses, while the HFIR data shows an immediate softening at low doses. The primary differences between the two irradiation is the helium concentration; both reactors have about the same displacement rate, $\sim 10^{-6}$ dpa/s, but EBR-II produces < 50 appm helium while HFIR easily produces > 100 appm helium. Helium is a possible cause of irradiation softening. Figure 1-B shows the same data plotted as a function of the empirical parameter $\sqrt{hpa \cdot dpa}$. The data show some overlap in the $\sqrt{hpa \cdot dpa}$ parameter and appear to correlate well. However, since this is an empirical correlation, one cannot rule out another function of helium and dpa. Figure 2 shows the same effect at 375°C.

The irradiation hardening is described by the function

$$\Delta YS_H = Y_H \left(1 - e^{-\beta dpa}\right) e^{-\alpha \cdot \sqrt{hpa \cdot dpa}} \qquad (1)$$

where Y_H, α , and β are temperature dependent parameters. Since α and 6 appear as rate constants, this suggests an Arhenius-type equation for the temperature dependence. A preliminary analysis of the data at 25, 375, 420, and 475°C confirmed this. The equations for a and β have the form

$$\alpha, \beta = \xi e^{\eta/T}, \qquad (2)$$

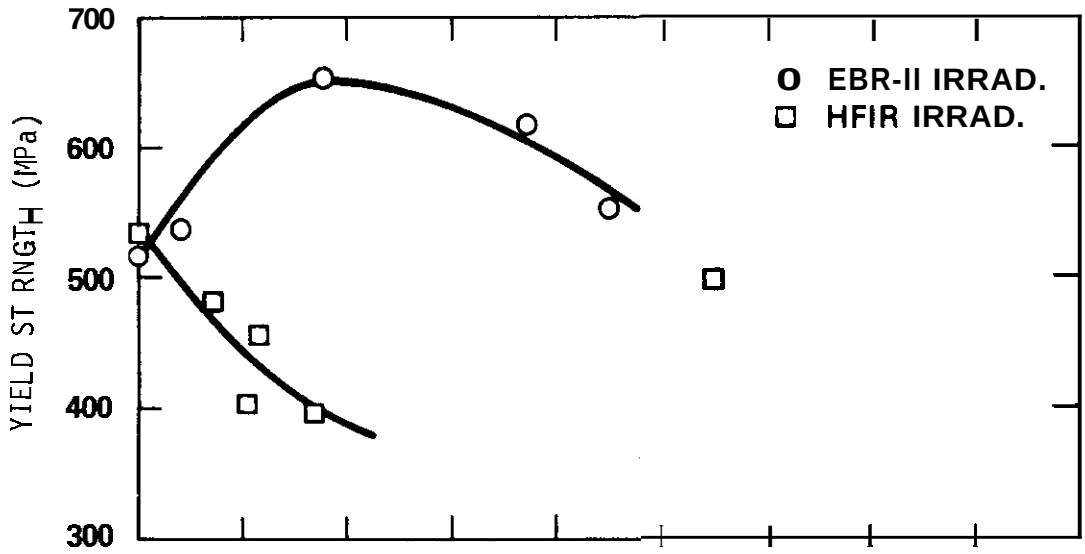

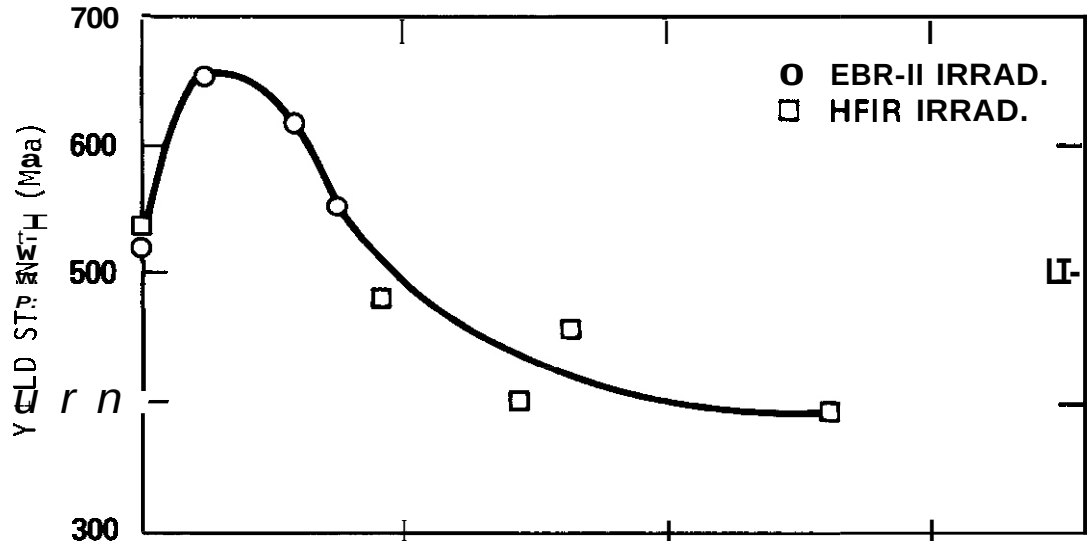

$\sqrt{hpa \cdot dpa}$

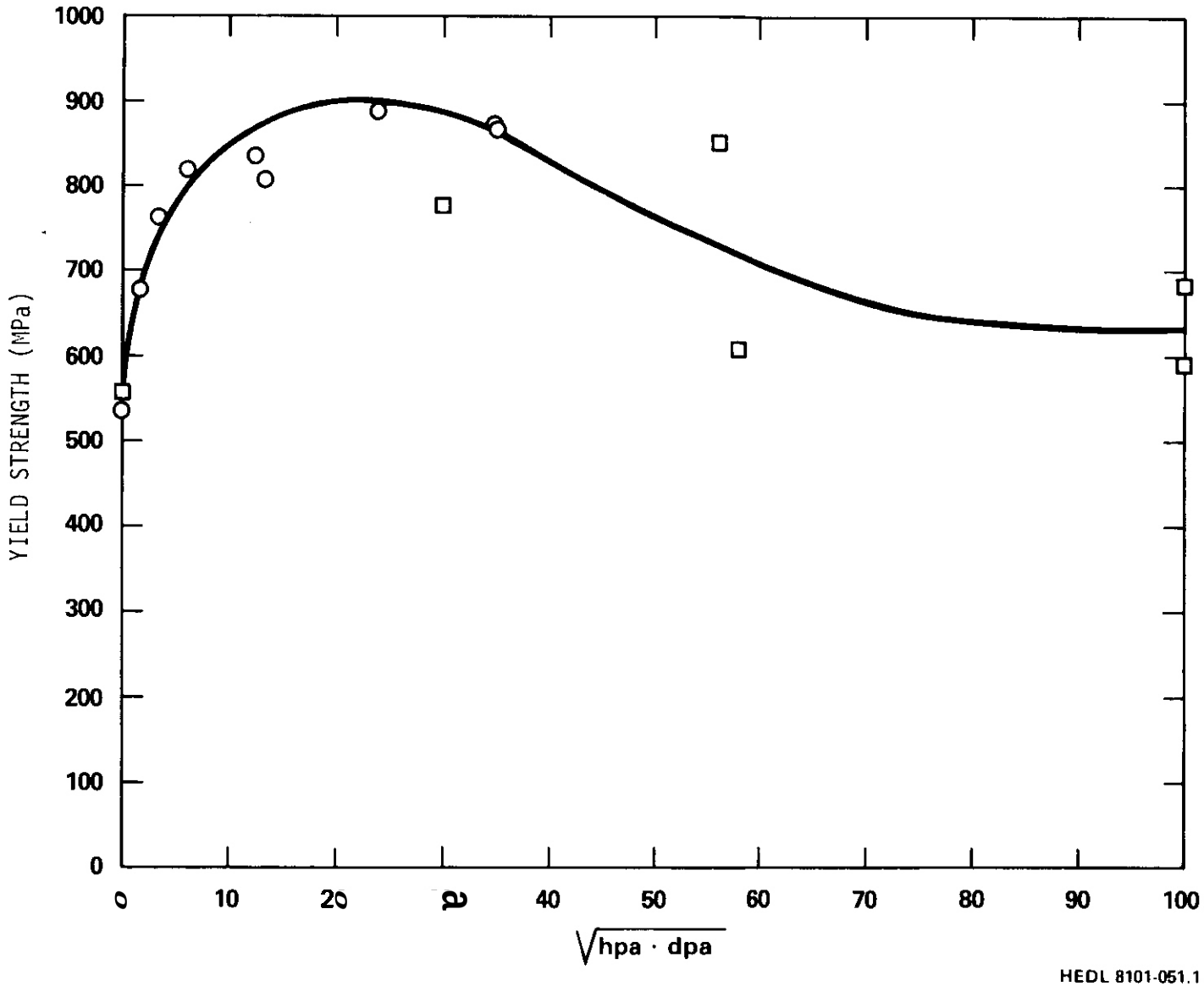

Figure 2 Yield Strength versus $\sqrt{hph \cdot dpa}$ for 380°C Irradiation Temperature.

where ξ and η are fitted constants. The constant η is positive for β and negative for α. A simple rate constant as in equation (2) implies a single mechanism or multiple mechanism with additive activation energies. In equation (1), β dominates at low temperatures, giving a saturation effect, while α dominates at high temperatures, resulting in essentially no hardening. With the form of a and β established, the Y_H function was described by a linear function of temperature (°K). In the analysis of the data, the best fit to the high temperature data was obtained when Y_H was constant above 500°C.

The high temperature (T > 500°C) yield strength shows softening in both EBR-II and HFIR irradiations, and in ex-reactor aging experiments. Fish et al.[1] point out that aging accounts for most of the yield strength softening. Although irradiation appears to contribute to the softening, the mechanism causing it is not clear. The exposure or time dependent term is probably a saturation function; however, it appears to have such a short time constant that it has little effect for irradiation times in excess of ~1000 hours. There were too few data points to determine the temperature dependence of the time constant, and consequently it was treated as independent of irradiation temperature. This may introduce some scatter in the data at low doses. The softening effect is largest in the 550 - 650°C range, with less softening at both ends of this temperature range. A function which describes this temperature dependence is

$$\Delta YS_A = \Omega(T - T_o)\, e^{-\omega(T - T_o)}, \quad T \geq T_o \qquad (3)$$
$$= 0, \quad T < T_o$$

where Ω, ω and T_o are fitted parameters. This function includes effects from aging and irradiation.

The final yield strength equation used for the temperature range 25 < T < 800°C is

$$Y = Y_o + Y_1 (1 - e^{-\beta dpa})\, e^{-\alpha\sqrt{dpa \cdot hpa}} - Y_2 (1 - e^{-\gamma dpa}) \qquad (4)$$

where

$$Y_1 = A \cdot T - B \qquad T \leq T_1$$
$$Y_1 = A\ T_1 - B \qquad T \geq T_1$$
$$T_1 = 773°K$$
$$\beta = C \exp(+ D/T)$$
$$a = E \exp(-F/T)$$
$$Y_2 = G\ (T - T_o) \exp\left[-H(T - T_o)\right], \quad T \geq T_o$$
$$Y_2 = 0, \quad T \leq T_o$$

where A, B, C, O, E, F, G, H, T_o, and γ are fitted constants. The temperature T is in units of degrees Kelvin, dpa is the number of displaced atoms per atom, hpa is the helium atoms per atom in units of appm, and Y_o is the measured unirradiated yield strength in MPa.

Results and Discussion

The primary emphasis of this analysis was placed on the heat 87210 (N and T lots) with lower emphasis on the DO heat. Table II summarizes the parameters which minimize the weighted sum of the squares of the residuals for equation (4). The weighted 2σ uncertainty with these parameters is ± 65 MPa.

TABLE II

Fitted Parameters for Equation (4)

Parameter	Value	Units
A	0.969	MPa/°K
B	168.	MPa_{-1}
C	4605.	$(dpa)^{-1}$
O	10080.	(°K)
E	617.	$(hpa\ dpa)^{-1/2}$
F	7079.	(°K)
G	6.55	MPa/°K
H	0.01389	$(°K)^{-1}$
T_o	730.	(°K)
γ	0.384	$(dpa)^{-1}$

Two additional solutions were determined with alternate weights (1.0 and 0.0) for the DO heat. Initially using the parameters of Table II and a weight of one far the DO heat data, the 2σ uncertainty was 110 MPa. However,

the solution diverged. With a weight of zero for the DO heat data (i.e., excluding DO heat data), the solution converge poorly (i.e., the solution exhibited small oscillations) with a 2σ uncertainty of about 50 MPa. In both cases the determination of the parameters E and F adversely affected the solution convergence. These parameters determine α, which influences the high exposure softening in yield strength. With a weight of one there is apparently too much scatter in the data, and with a weight of zero there is insufficient information to determine the constants for a. The intermediate weight allows a compromise between the two extremes. This demonstrates the need for accurate data with high helium content (>50 appm) from HFIR irradiations to complement the data from EBR-II.

Figure 3 shows the data for heat 87210 and the curves for each temperature group. The curves correspond to an EBR-II core center spectrum. With only a few exceptions the curves fit the data reasonably well. The one major exception is for 515°C. The yield strength data drops further at low dpa than predicted by the curve. This is probably due to the simplicity of the model. This temperature corresponds to the onset of recrystalization and recovery which may require additional parameters to describe adequately. However, it is observed that the general features of the data are apparent in the curve, i.e., a weak peak around 20 dpa.

At higher temperatures, the temperature independent constant for the transient term may be an over-simplification; however, a more complex temperature dependence may be difficult to determine due to the scarcity and scatter in the data. A dpa transient was found to fit the data best. With a helium dependent transient term, the least square fitting routine would not converge. This does not rule out any helium effect at temperatures above 500°C. At 840°C the equation (4) is about 50% higher than the measured data. Although this is within the 95% confidence level of certainty, the application of equation (4) is limited to <800°C.

Figure 4 shows a plot of measured versus calculated yield strength for heat 87210. The dashed lines represent the 95% confidence bounds (±65 MPa).

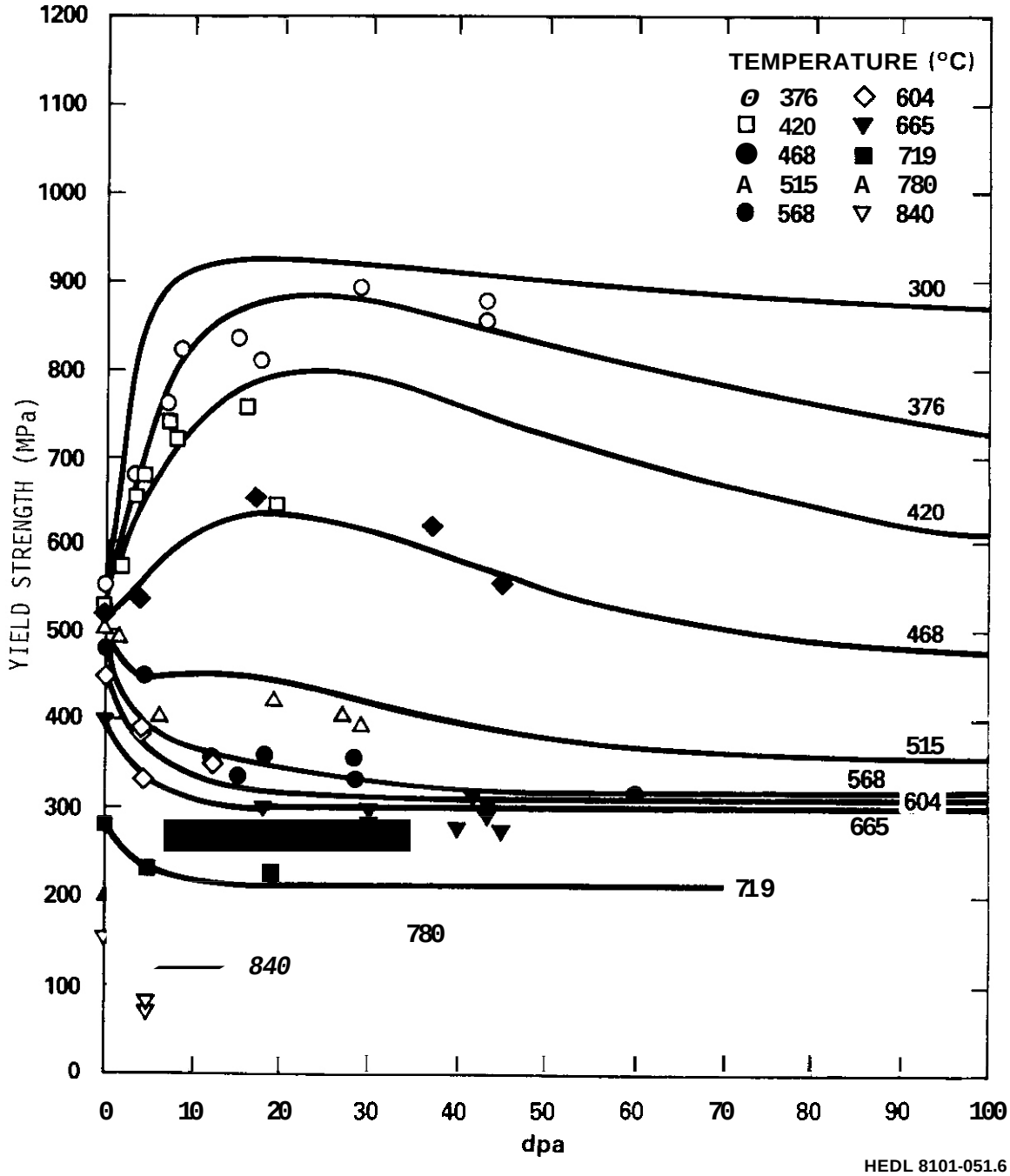

FIGURE 3. Heat 87210 Yield Strength Data Versus Damage Exposure.

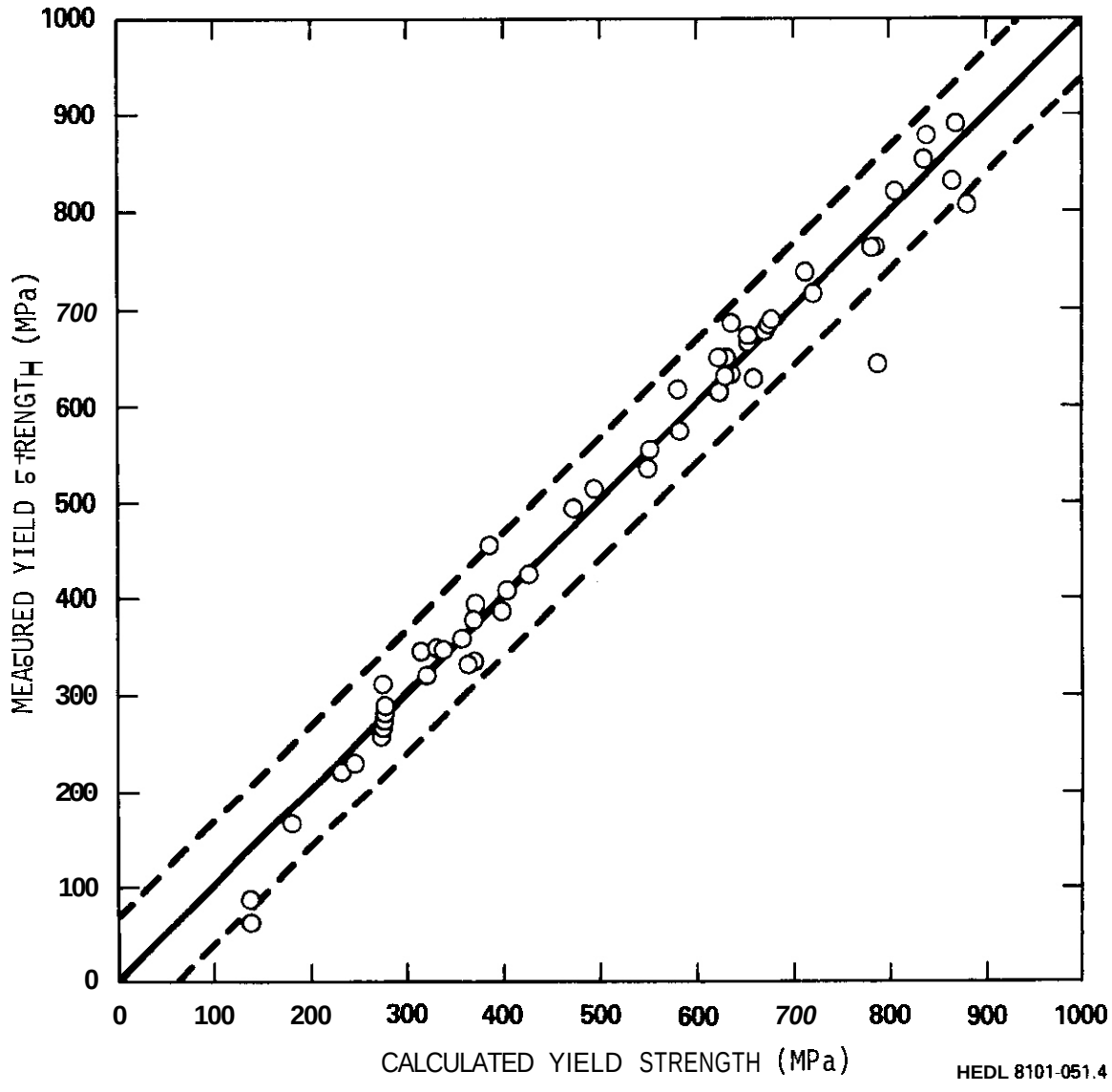

FIGURE 4. Heat 87210 Yield Strength Data Versus Calculated Yield Strength.

The high exposure softening is strongest in the temperature range 300 < T < 568°C. This temperature range also corresponds to the swelling region of 316 SS. Helium is generally considered as a source of void nucleation. Since the softening correlated fairly well with helium content, it is assumed that void or gas bubble swelling is involved in the softening mechanism. Bloom and Wiffen[3] found that the high density of voids and/or bubbles produced in HFIR irradiated specimens was associated with a reduction in the dislocation density. Thus, the voids, which are generally considered as a weak hardening mechanism, possibly act indirectly to reduce dislocation density which, in turn, lowers the yield strength.

Figure 5 shows the DO heat data and the predicted curves for the corresponding temperature for HFIR irradiations. The scatter in the data about the predicted curves is substantially greater than for the heat 87210. Since the gamma heating rates are ten times higher in HFIR than in EBR-II and are uncertain by 10%, the temperatures are harder to pre-select and control in HFIR than in EBR-II. Grossbeck and Mazias2[4] reported that the temperature for the HFIR specimens are accurate on a relative scale but could be as much as 50 - 75°C low on an absolute scale. For heat 87210 irradiated in EBR-II a temperature increase from 475 to 525°C decreases the yield strength nearly 200 MPa. Consequently, the large scatter is not surprising.

The HFIR data show a more rapid softening than the EBR-II data in the intermediate temperature region (300 - 500°C). This is assumed to be related to the much higher helium generation in HFIR than in EBR-II. Below about 300°C the displacement-related hardening appears to dominate the yield strength behavior. Similarly the yield strength behavior above about 600°C appears to be generally similar to that in EBR-II.

Figure 6 shows the DO heat yield strength data plotted versus calculated yield strength. The dashed lines show the same 95% confidence bounds shown for the heat 87210 data. One half of the DO heat data falls within the boundaries, about 25% of the data fall just outside the boundaries, and the remaining data fall significantly outside the boundaries. Note that two-

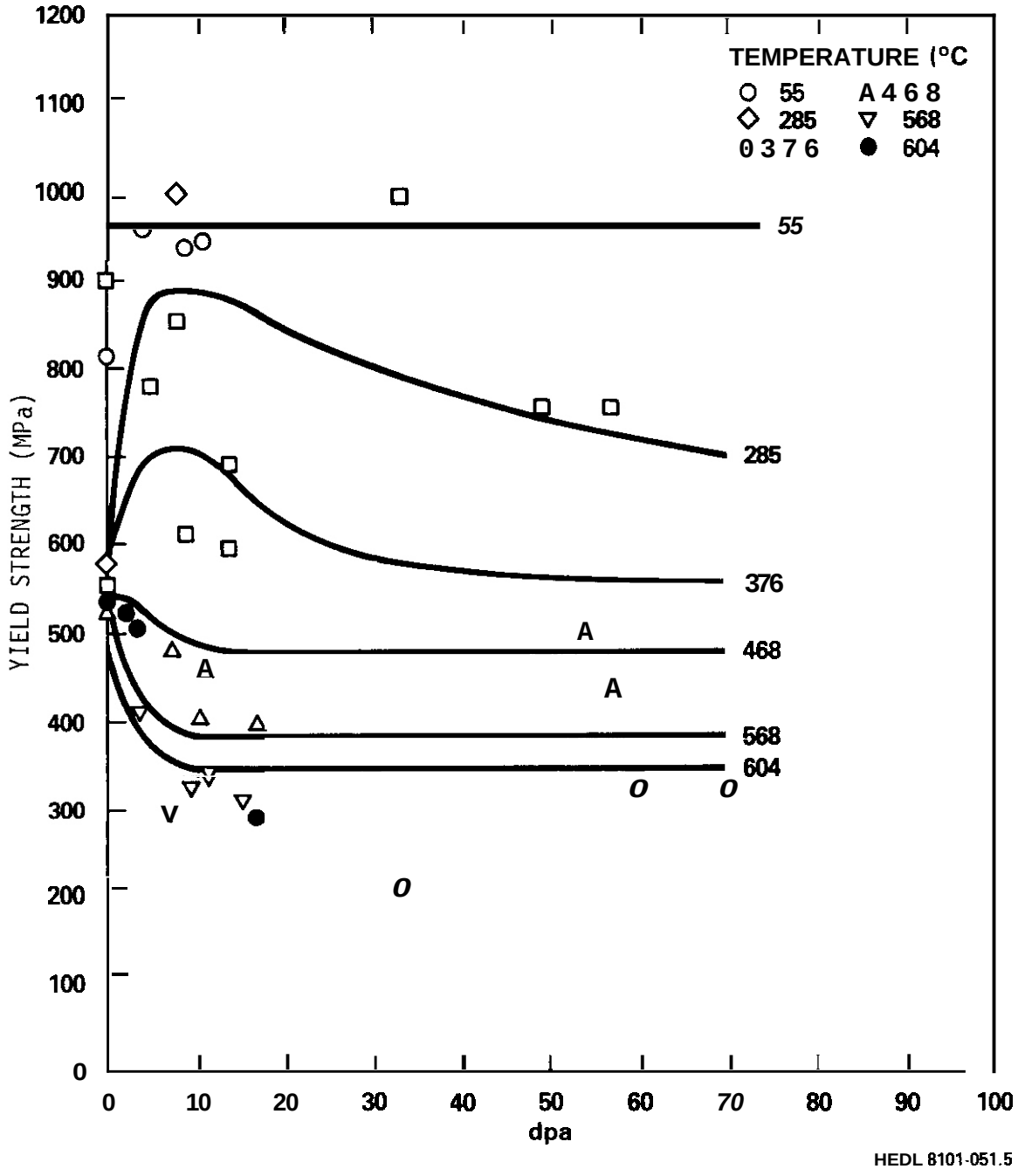

FIGURE 5. **DO** Heat Yield Strength Data Versus Damage Exposure.

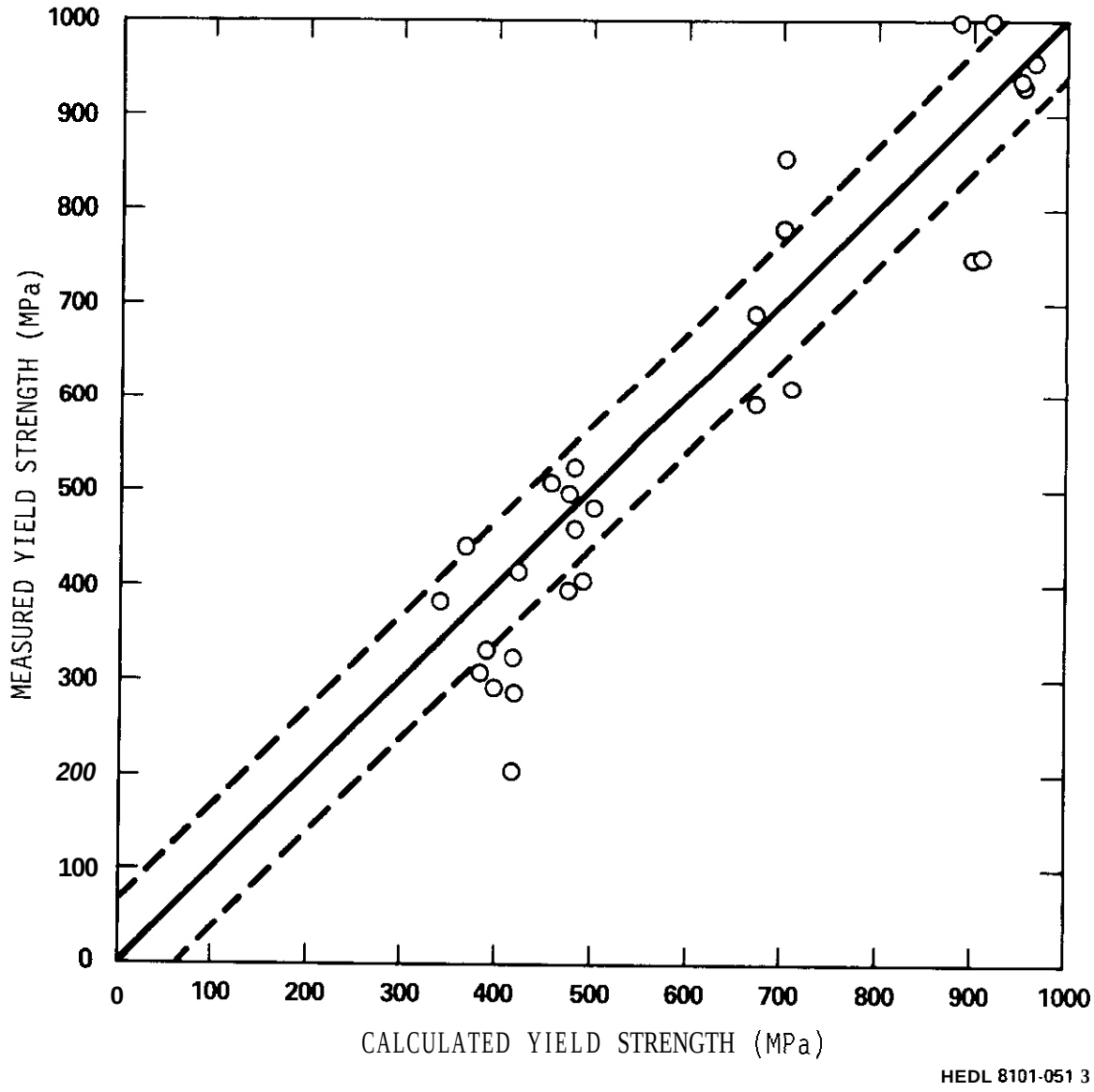

FIGURE 6. DO Heat Yield Strength Data Versus Calculated Yield Strength.

thirds of the DO heat data fall on the low side of the curve, which indicates that the predicted values are high. Note also that these predicted values are based on unirradiated values which are higher. Most of the over predictions are at low yield strength values which correspond to high temperatures (>500°C).

Summary and Conclusions

Data on tensile properties of irradiated 20% CW 316 stainless steel were compiled and helium and dpa values were calculated for all the data. A ten-parameter equation was developed to describe behavior of yield strength for irradiation temperatures ranging from 25 to 800°C. The equation uses both high helium (>100 appm) and low helium (<50 appm) data so that it should be applicable to all neutron environments. The test conditions are for strain rates < 5×10^{-4}/second and irradiation temperatures approximately equal to test temperatures. The equation fits the heat 87210 (N and T lots) data *to* within ±65 MPa (15%) at the 95% confidence level. The DO heat data irradiated in HFIR shows larger scatter, but it is predicted to within about ± 100 MPa. The correlation equation is characterized by an initial irradiation hardening which saturates, followed by a softening effect, which is correlated with the square root of helium concentration and displacements per atom. Above approximately 500°C the yield strength change appears to be dominated by recrystallization and recovery as noted by Fish et al.[1]

VI. REFERENCES

1. R. L. Fish, N. S. Cannon, and G. L. Wire, "Tensile Property Correlations for Highly Irradiated 20% Cold Worked Type 316 Stainless Steel," ASTM STP 683, 1979, pp. 450 - 465.

2. R. J. Puigh and N. F. Panayotou, "Tensile Properties Data on 316 SS Irradiated at RTNS-II," DAFS Quarterly Progress Report DOE/ER-0046/3, November 1980.

3. E. E. Bloom and F. W. Wiffen, "The Effects of Large Concentrations of Helium on the Mechanical Properties of Neutron-Irradiated Stainless Steel," J. Nuc. Mat., 58, (1975), p. 171.

4. M. L. Grossbeck and P. J. Maziasz, "Tensile Properties of Type 316 Stainless Steel Irradiated in a Simulated Fusion Reactor Environment," J. Nuc. Mat., 85 and 86 (1979), 883 - 887.

5. F. W. Wiffen, "The Effects of Irradiation at About 55°C on Type 316 Stainless Steel," ADIP Quarterly Progress Report, January - March 1978, DOE-ET-0058/1.

6. K. Q. Bagley, J. W. Barnaby, and A. S. Fraser, "Irradiation Embrittlement of Austenitic Stainless Steels," from British Nuclear Energy Society Conference Irradiation Embrittlement and Creep in Fuel Cladding and Core Components, November 9 - 10, 1972.

7. J. E. Irvin and A. L. Bement, "Nature of Radiation Damage to Engineering Properties of Various Stainless Steel Alloys," ASTM STP 426, 1967.

3. H. R. Higgy and F. H. Hammond, "Effect of Fast-Neutron Irradiation on the Mechanical Properties of Stainless Steels: AISI Types 304, 316, and 347," J. Nuc. Mat., 55 (1975), 177 - 186.

9. R. L. Simons, J. A. Ulseth, N. J. Graves, "EBR-II Spectral Parameters (Reactor Run 50H)," HEDL-TME-74-44, July 1974.

10. C. L. Long, et al., "EBR-II Spectral Parameters Run 75D," HEDL-78-84, March 1979.

11. J. K. Brammen, et al., "Radiation Damage Units for Fast Reactor Steels," ibid. ref. 6.

12. F. W. Wiffen, et al., "The Production Rate of Helium During Irradiation of Nickel in Thermal Spectrum Fission Reactors," J. Nuc. Mat., 85 and 36 (1979).

13. W. N. McElroy and H. Farrar IV, in Proceedings of Conference on Radiation Induced Voids on Metals, CONF-710601, April 1972, p. 137.

14. J. M. Steichen, High Strain Rate Tensile Properties of 20% CW Type 316 Stainless Steel, HEDL-TME-74-39, Hanford Engineering Development Laboratory, Richland, WA, February, 1974.

15. G. D. Johnson, et al., "A Microstructural Interpretation of the Fluence and Temperature Dependence of the Mechanical Properties of Irradiated AISI 316," HEDL-SA-2045, April 17, 1980.

VII. FUTURE WORK

Ultimate tensile strength, uniform elongation and total elongation data will be analyzed.

I. PROGRAM

Title: Irradiation Effects Analysis (AKJ)
Principal Investigator: D. G. Doran
Affiliation: Hanford Engineering Development Laboratory

II. OBJECTIVE

The objective of this work is to determine the effects of high energy neutrons on damage production and evolution, and the relationships of these effects to effects produced by fission reactor neutrons. Specific objectives of current work are the planning and performance of irradiation programs at the Rotating Target Neutron Source (RTNS)-II at the Lawrence Livermore National Laboratory (LLNL) and the Omega West Reactor (OWR) at the Los Alamos National Laboratory (LANL).

111. RELEVANT OAFS PROGRAM TASK/SUBTASK

Subtask	II.B.3.2	Experimental Characterization of Primary Damage State; Studies of Metals
	II.C.6.3	Effects of Damage Rate and Cascade Structure on Microstructure; Low-Energy/High-Energy Neutron Correlations
	II.C.11.4	Effects of Cascades and Flux on Flow; High-Energy Neutron Irradiations
	II.C.18.1	Relating Low- and High-Exposure Microstructures; Nucleation Experiments

IV. SUMMARY

A new reactor furnace fabricated at LLNL has been installed in the OWR, a thermal reactor located at LANL. The flux-spectrum of the reactor has been measured by Argonne National Laboratory and the initial experiment assembled at Hanford Engineering Development Laboratory (HEDL). This experiment,

HEDL-Ia, will be one of several low-energy irradiations which will complement HEDL-VR, an ongoing high-energy neutron experiment at RTNS-II (LLNL). Together these experiments will provide a basis for the correlation of displacement effects of low and high energy neutrons. The matrices *of* both experiments are described. A new furnace fabricated at HEDL has been delivered to the RTNS-II facility at LLNL. The furnace permits irradiation of specimens at two temperatures simultaneously without any significant loss of high flux irradiation volume.

V. ACCOMPLISHMENTS AND STATUS

Spectral Effects Experiments - N. F. Panayotou (HEDL)

A. Omega West Reactor

The Type A In-Core Furnace, designed and built by R. Van Konynenberg (LLNL), has been installed in the 4F position of the OWR facility at Los Alamos National Laboratory. Irradiation temperatures from 70 to about 120°C can be obtained using this furnace. It will permit irradiation of specimens identical to those currently undergoing irradiation in HEDL-VR. For irradiations attemperatures in excess of 120°C, a Type B In-Core Furnace is currently under construction at LLNL.

OWR is a thermal, heterogeneous, sealed and pressurized tank-type research reactor located at the Omega site *of* Los Alamos National Laboratory.(1) The reactor utilizes aluminum-clad fuel elements of the Materials Testing type and is light water moderated and cooled. The normal operating power level of the reactor is 8 MW. Based on the analysis by L. R. Greenwood (see report elsewhere in this volume), the neutron flux at the specimen capsule position is 5.7 x 10^{13} n/cm^2-s, E >0.1 MeV.

The In-Core Furnace was originally intended to be used in the Livermore Pool Type Reactor (LPTR). A sealed specimen capsule, separated from reactor coolant by a void space, was designed to be heated by a

combination of nuclear and electrical heating to temperatures ranging from reactor ambient to 800°C. Various temperatures could be obtained by altering the thermal conductivity of the void space: reactor water could be used from reactor ambient to about 95°C, static helium for intermediate temperatures, and a vacuum for temperatures up to 800°C. Upon the termination of the operation of LPTR, the furnace was modified for use in the OWR facility. Due to the higher gamma heating rate in OWR, provisions for the use of circulating coolants had to be made. With circulating reactor coolant water, the Type A In-Core Furance can operate at temperatures between 70 (reactor ambient) and 120°C with ±1°C control. The maximum permissible irradiation temperature is limited by the boiling point of the pressurized reactor cooling water. The use of circulating helium gas was judged to be impractical. Therefore, a second furnace (designated Type B) is currently being modified at LLNL so that helium can be circulated using a small Roots-type blower.

A sectional view of the lower 25 cm of the Type A In-Core Furnace is shown in Figure 1. Specimen temperature is monitored and controlled with a chromel-alumel sheathed thermocouple inserted in the center of the specimen capsule. The thermocouple assembly also acts as the specimen capsule positioning device. As shown, the capsule is seated firmly against a stainless steel hot finger. Two heaters (one a spare) are wound around the hot finger and the main furnace tube. Two additional thermocouples were brazed into holes in the hot finger. A tube, added for circulation of reactor coolant, is also shown.

An exploded view of the specimen capsule assembly is shown in Figure 2. The assembly consists of three components: an outer shell, a specimen holder, and a capsule cover with a thermocouple well. For low temperature irradiations the specimen capsule is fabricated using aluminum alloys. TEM disk and microtensile wire specimens are loaded into the 10 drilled and tapped holes in the specimen holder. Specimens are held in place by set screws. This holder design can accommodate 500, 0.38-mm-thick TEM disk specimens. The total available specimen volume within the

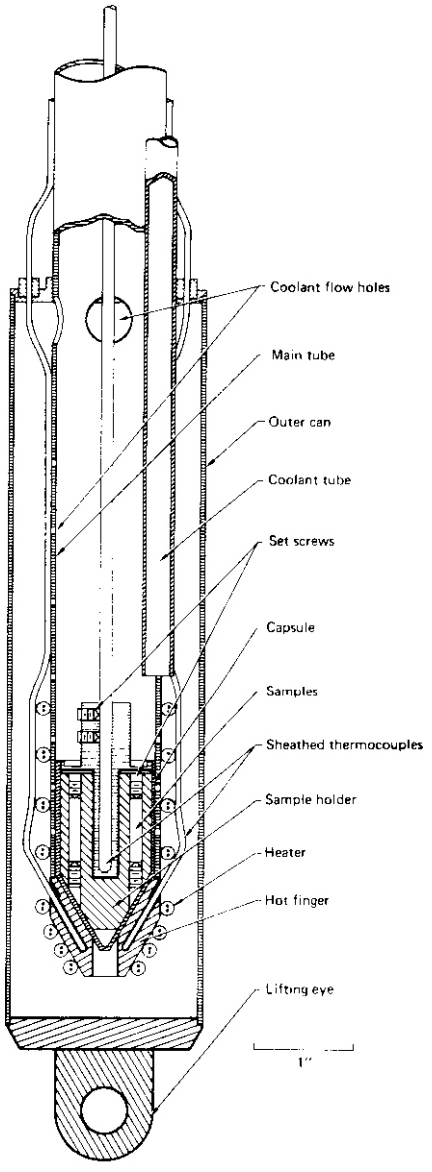

FIGURE 1. Sectional View of the Type A In-Core Furnace Currently Located in the 4F Position of the Omega-West Reactor, Los Alamos National Laboratory.

shell is about 13 cm^3. Other specimen holders can be fabricated to accommodate other specimen geometries.

After loading, the assembly is clamped together, evacuated, electron beam welded shut and leak checked. This procedure assures good thermal contact between the components of the specimen capsule, and minimizes oxygen contaiiiination

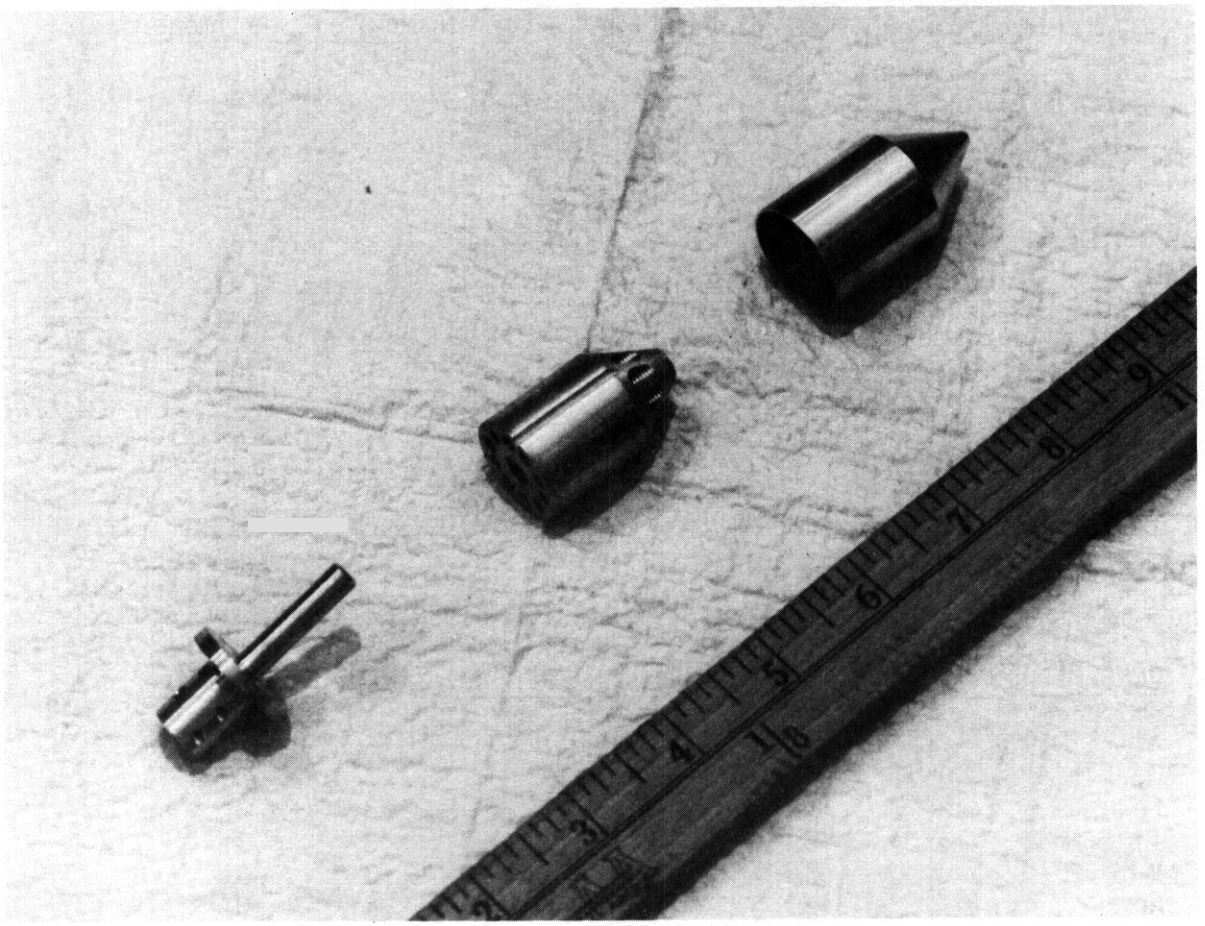

FIGURE 2. Exploded View of the In-Core Furnace Specimen Capsule Assembly.

of the specimens.

The HEDL-Iω experiment will be initiated during the next reportin
period. The irradiation te 5°C and the goal fluence is
$2 \cdot 10^{19}$ n/cm^2, E >0.1 MeV, a fluence currently being obtained in the HEDL-VR
e: 20 microtensile wire
s| oils and wire supplied
by L. R. Greenwood (ANL) are included in the experiment.

adiation condition and postirradiation specimen test
ir le
three metals in four conditions were included (Table 1). The recrystallizа
tion heat treatments for the wire specimens were chosen so that a minimum

TABLE 1

HEDL-IΩ: MICROTENSILE WIRE SPECIMEN MATRIX

Alloy	Condition	Number of Specimens
HT-9	A & T	10
MFE 316 SS	CW	9
MFE 316 SS	Rxl	6
Ni	Rxl	3

CW = Cold Worked
SA = Solution Annealed
A&T = Austenitized and Tempered
Rxl = Recrystallized
μH = Microhardness Testing
PIA = Postirradiation Annealing
A = Aged
SR = Stress Relief
Recon. = Experiment Reconstitution

TABLE 2

HEDL-IΩ: TEM DISK SPECIMEN MATRIX

PURE METALS	CONDITION	μH /RECON.	TEM	μH/PIA
Ni	Rxl	1	3	3
Cu	SR	13	3	3
Fe	Rxl	1	3	3
Ti	Rxl	15	3	3
V	Rxl	5	3	3
Nb	Rxl	5	5	3
PATH A TYPE ALLOYS				
FFTF 1st Core 316 SS	20% CW	6	3	3
FFTF 1st Core 316 SS	Rxl	13	3	3
N lot 316	Rxl	6	3	3
MFE 316 SS	40% CW	8	3	3
MFE 316 SS	Rxl	6	3	3
PCA	40% CW	1	3	3
PCA	Rxl	8	3	3
Fe-15Cr-20Ni (E-19)	30% CW	8	3	3
Fe-15Cr-20Ni (E-19)	Rxl	8	3	3
Fe-15Cr-20Ni-2Mo	40% CW	6	3	3
Fe-15Cr-20Ni-2Mo	Rxl	6	3	3
Fe-15Cr-20Ni	30% CW	6	3	3
Fe-15Cr-20Ni	Rxl	6	3	3
Fe-15Cr-20Ni-.12C	30% CW			3
Fe-15Cr-20Ni-.12C	Rxl			3

TABLE 2 (Cont'd)

PATH A TYPE ALLOYS	CONDITION	μH/RECON.	TEM	μH/PIA
Fe-15Cr-20Ni-.3Si	30% CW	6	3	3
Fe-15Cr-20Ni-.3Si	Rxl	6	3	3
Fe-15Cr-20Ni-.12C-.3Si	30% CW	6	3	3
Fe-15Cr-20Ni-.12C-.3Si	Rxl	6	3	3
BINARY ALLOYS*				
Cu-5Al	SA	6	3	3
Cu-5Ni	SA	6	3	3
Cu-5Mn	SA	5	3	3
Cu-50Ni	SA	6	3	3
Ni-5Al	SA	6	3	3
Ni-5Si	SA	6	3	3
Ni-8Si	SA	6	3	3
Ni-5Mn	SA	6	3	3
Ni-19.6Al	A	-	2	-
Ni-12.8Al	SA	-	2	-
Ni-12.8Al	A	-	2	-
Ni-12.7Si	SA	-	2	-
Ni-12.7Si	A	-	2	-
PATH E TYPE ALLOYS				
HT-9	A & T	8	3	3
Fe-10Cr	30% CW	6	3	3
Fe-10Cr	Rxl	6	3	3
A533	A & T	8	3	3

*Atomic percent

of ten grains would be obtained across the 0.254-mm diameter gage section. TEM disk specimens (Table 2) of six pure metals, ten Path A type alloys in nineteen conditions, thirteen binary alloys, and three Path E type alloys in four conditions were included. Specimens of alloy E-19 and a 2 w/o Mo variation of E-19 have been included in previous irradiations. The second Fe-15Cr-20Ni alloy listed and the carbon/silicon variations of this alloy have a different prior histories than E-19 and are new additions to the DAFS metals stockpile at HEDL. A total of ten specimens of Ni-Al and Ni-Si alloys were received from Don Potter (U. of Conn.) and Mike Guinan (LLNL) and were included in this experiment.

Specimens of an Fe-10Cr binary alloy were also included. This particular composition was chosen to bridge the gap between pure Fe and HT-9. As in HEDL-VR disk specimens of A533, a light water reactor pressure vessel steel, were included. In all cases the recrystallized condition was defined as that heat treatment which produced a minimum grain size. when applied to the cold-worked stock material. The copper stock material, however, was received in an annealed condition and was therefore only stress-re1ieved prior to irradiation.

Except for the Potter/Guinan binary alloys at least three specimens of each metal-condition will be set aside for both TEM and microhardness, followed by annealing studies. The balance of the specimens will be available for reconstitution into another, higher dose, experiment.

B. RTNS-II Facility

In order to maximize the data obtained from long-term elevated temperature high-energy neutron experiments, a new HEDL vacuum furnace, designated Type C, was fabricated and delivered to the RTNS-II facility. Figure 3 illustrates the evolution which has occurred in the three vacuum furnaces built by HEDL for use at the RTNS-II facility. The Type C RTNS-II furnace was designed so that high energy neutron irradiations could be performed at two temperatures simultaneously. A difference of 250°C can be maintained between the two temperature zones, which are separated by only 1.8 mi. This device increases HEDL's utilization of the source time of RTNS without any significant loss of high flux irradiation volume. Like its predecessors, the Type C furnace maintains a high vacuum environment. It also minimizes the distance between specimens and the neutron source by using efficient thermal barriers.

The specimen cage of the Type C furnace can accommodate specimen capsules approximately 6 x 47 mm in size. The controlled temperature zone is 10 cm in depth. The furnace can heat specimens up to 400°C while maintaining a continuous 10^{-5} torr vacuum.

FURNACE DESIGN EVOLUTION

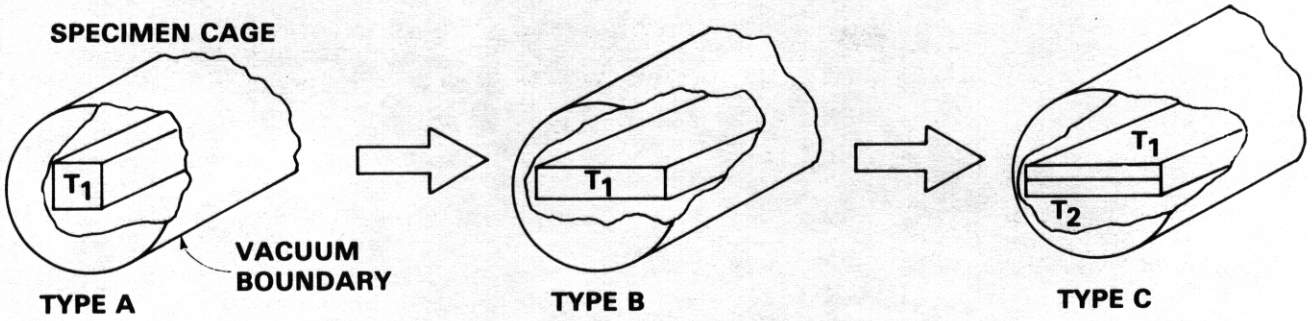

FIGURE 3. Evolution of the Specimen Cage of HEDL Vacuum Furnaces.

The Type A and B furnaces were designed to heat specimens up to 800°C while maintaining a continuous 10^{-7} torr vacuum. The Type A furnace can accommodate 15 x 15 mm specimen capsules and was designed specifically for use with the 23-cm diameter rotating target. The Type B furnace can accommodate 15 x 47 mm specimen capsules; it was designed for use with the 50-cm diameter rotating target, but can also be used with the smaller target. The depth of the controlled temperature zone is 2.5 cm for both furnaces.

Specimen holders for the Type C furnace are both modular and multi-purpose. Actual holders and specimens are shown in Figure 4. Specimens are stacked into the appropriate spaces and cover foils are spot welded on both sides of each module to maintain specimen positions during handling and irradiation. Iron dosimeter foils and wires are also loaded in to appropriate positions. The specimen holder modules can then be stacked so that the proper fluences will be obtained. This type of holder design permits both disk and tensile specimens to be irradiated simultaneously while also allowing for other experiments to be included either within or behind the main experiment.

A view of the Type C furnace specimen cage is shown in Figure 5 as it would appear from the neutron source. The first specimen holder module in the two specimen holder stacks is visible. Each specimen holder stack occupies a separate temperature zone.

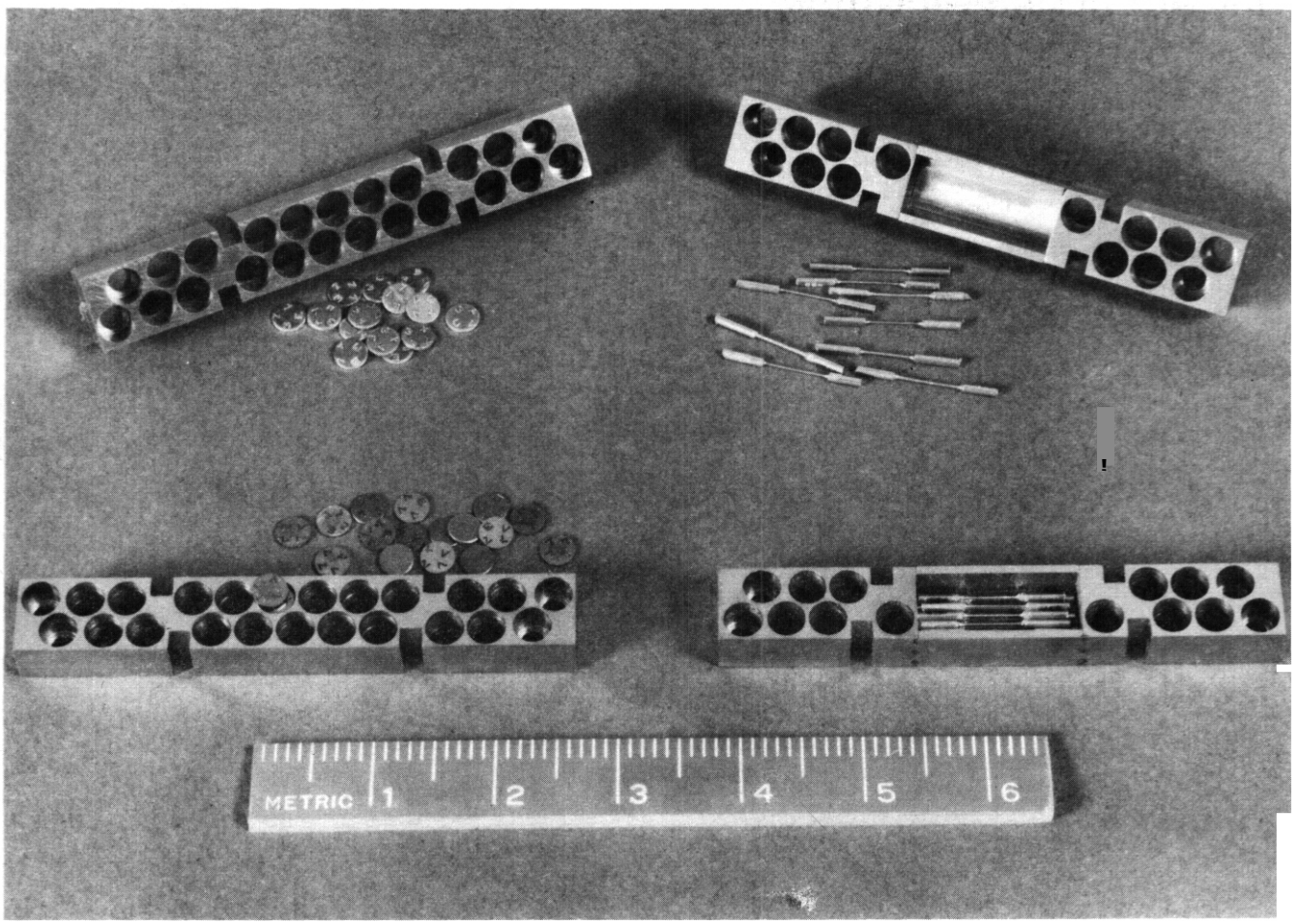

FIGURE 4. Modular Multipurpose Specimen Holders and TEM Disk and Microtensile Wire specimens

In these first specimen holder modules the maximum and minimum microtensile specimen doses are estimated to differ by a factor of 2.8. The maximum and minimum disk specimen doses are estimated to differ by a factor of 10. Over the specimen holder assembly depth of 100 mm it is estimated that the maximum and minimum specimen doses will differ by about a factor of 400.

Four thermocouples are in place in each temperture zone, three platinum-rhodium and one chromel-alumel type. (Decalibration of chromel-alumel thermocouples exposed to high energy neutrons has been observed by Guinan, LLNL). Each temperature zone is independently heated and can be quenched rapidly to room temperature by circulating water.

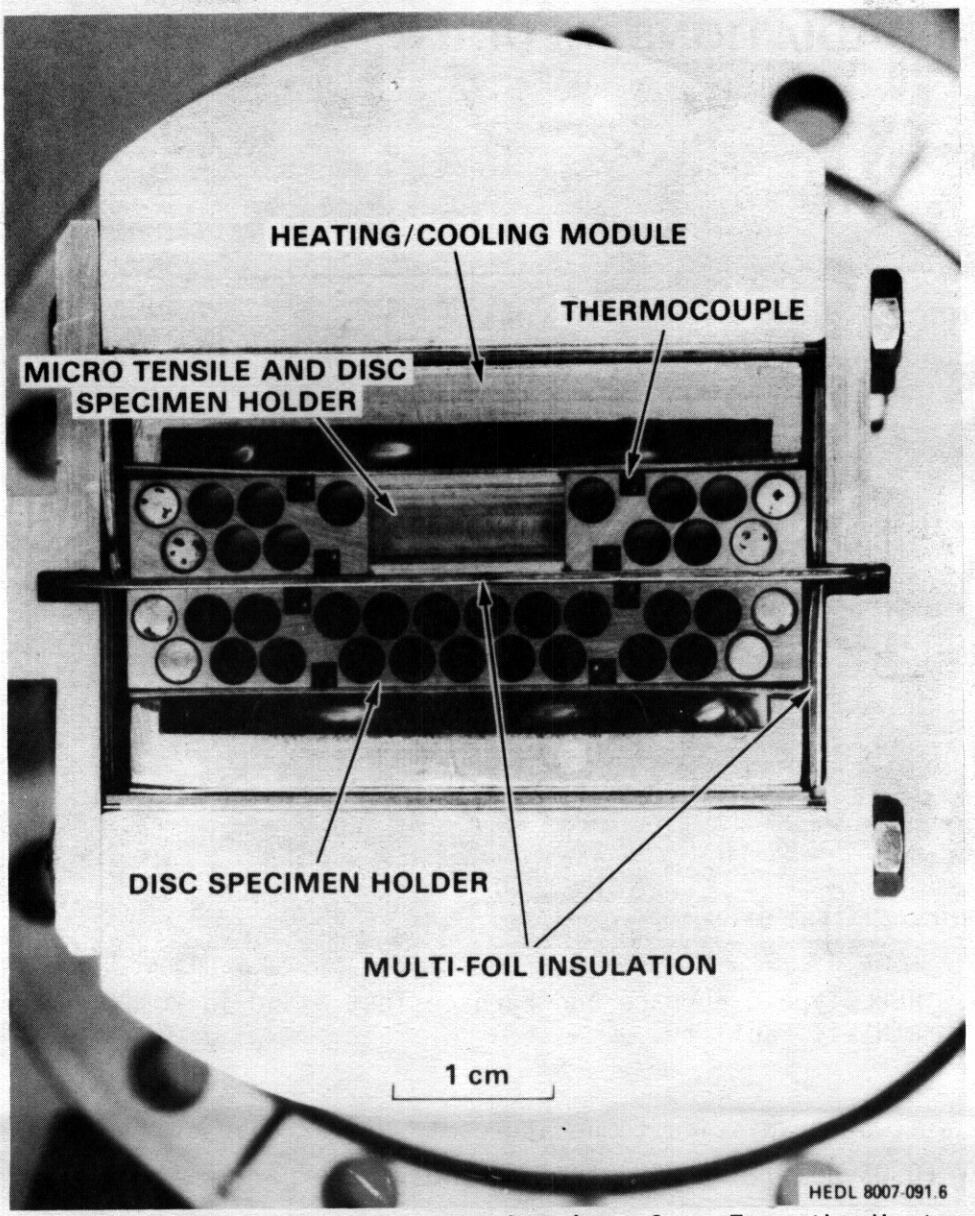

FIGURE 5. View of the Type C Furnace Specimen Cage From the Vantage Point of the Neutron Source.

A view of the Type C furnace and furnace stand is shown in Figure 6 in position at the RTNS-II facility. The continuous vacuum is produced by a turbo molecular vacuum pump. Initial difficulties with the vacuum system appear to have been resolved.

The objective of the HEDL-VR experiment is to obtain data on high energy neutron damage of alloys important to the design of the Engineering Test

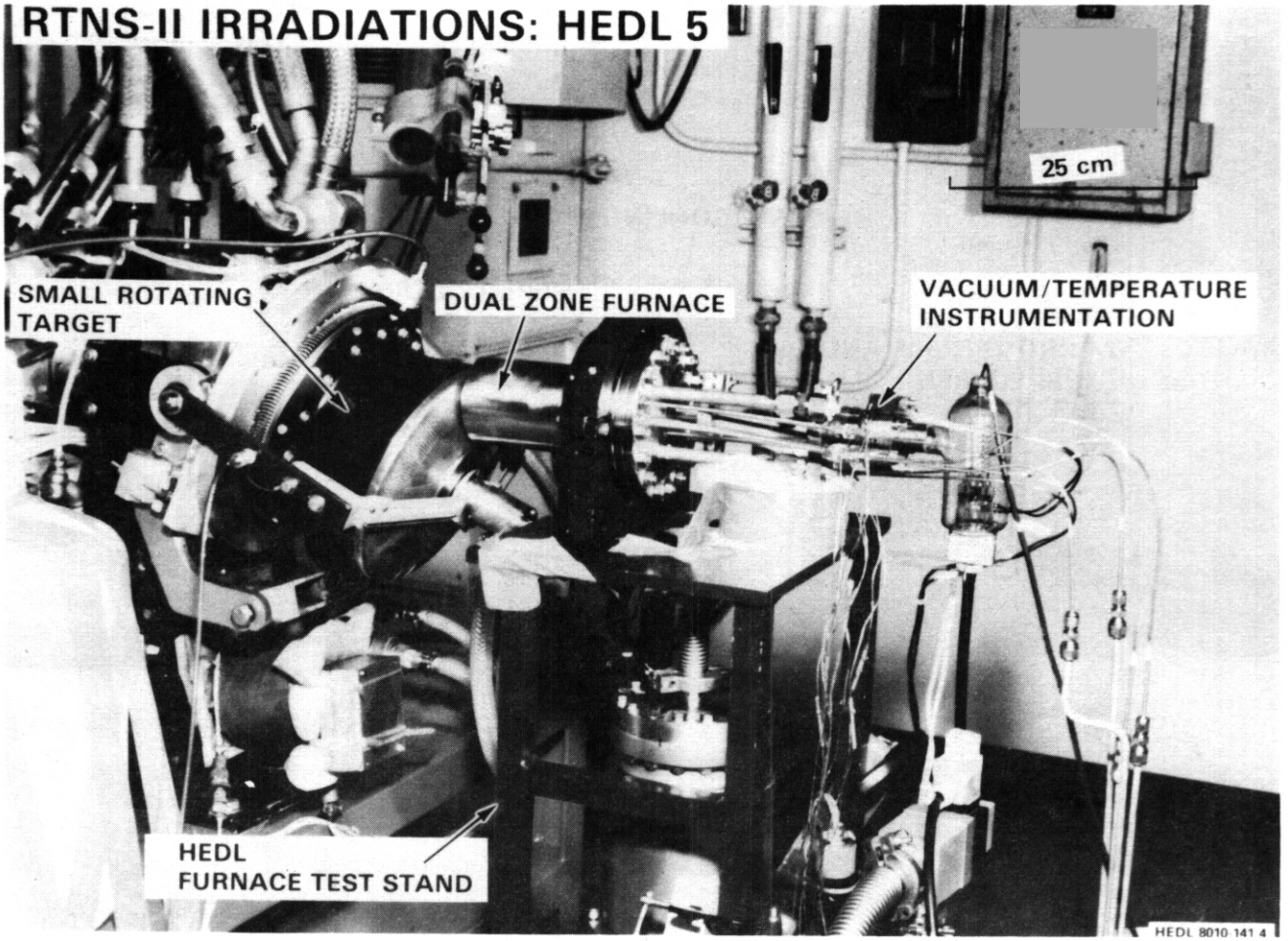

FIGURE 6. HEDL Type C Furnace and Furnace Test Stand in Position at the RTNS-II Facility.

Facility at two irradiation temperatures to a peak dose of $1 \cdot 10^{19}$ n/cm^2, E >14 MeV (0.03 dpa). The eventual goal of the experiment is $3 \cdot 10^{19}$ n/cm^2. The experiment employs the Type C furnace and modular multipurpose specimen holders described above in order to maximize the utilization of source time and volume. This is an important consideration since 20 weeks of facility time (80 hours per week) are required to reach $1 \cdot 10^{19}$ n/cm^2 with the available 23-cm diameter rotating targets.

The irradiation schedule for the experiment is shown in Table 3. Specimens will be removed after 5 and 20 weeks. Interim goal dose levels range from .05 . 10^{18} to 3.3 . 10^{18} for disk specimens and from $1 \cdot 10^{18}$ to

TABLE 3

IRRADIATION SCHEDULE: HEDL-VR

Dose Levels, x 10^{18} n/cm^2, E ~14 MeV

Specimen Type	5 weeks'	20 weeks'
Disk	0.05 0.2 0.4	0.8 1.7 3.3
Tensile		

+ Total facility time required assuming use of 23-cm diameter rotating targets operating 80 hours per week.

11 . 10^{18} for microtensile wire specimens. Additional dose levels and metals not included in the original specimen matrix can be added at the five week experiment reconstitution. A reconstitution matrix is currently being developed.

The preirradiation condition and postirradiation specimen test matrix are reported in Tables 4 through 8. The specimen matrix for each nominal temperature level is identical. The nominal temperature levels selected for the experiment were 80 and 288°C. Operating temperatures for ETF have been cited as 50 to 350°C.[2] A review of the literature by Simons (HEDL) indicates that irradiation-induced property changes in yield strength with dose are independent of irradiation temperature below about 200°C, while above 200°C, yield strength is strongly dependent upon irradiation temperature. Accordingly, a low nominal temperature of 80°C was selected. A high nominal temperature of 288°C was selected so that comparison of our data with the large body of light water reactor data would be possible.

A total of 72 microtensile wire specimens and 422 TEM disk specimens in each temperature level were included in the experiment. Microtensile wire specimens of three metals in four conditions were included (Table 4). The recrystallization heat treatments for the wire specimens were chosen so that

TABLE 4

HEOL-VR MICROTENSILE WIRE SPECIMEN MATRIX

Dose: $1 \cdot 10^{18}$, $1.1 \cdot 10^{19}$ n/cm^2, E ~14 MeV

T_i: 80 and 288°C

Metal	Condition	Number of Specimens
MFE 316	20% CW	12
MFE 316	Rxl	12
HT-9	A & T	8
Ni	Rxl	4

T_i = Irradiation Temperature
CW = Cold-Worked
SA = Solution-Annealed
A&T = Austenitized and Tempered
Rxl = Recrystallized
μH = Microhardness Testing
PIA = Postirradiation Annealing

a minimum of ten grains would be obtained across the 0.254-mm diameter gage section.

The TEM disk specimen matrices are reviewed according to their final calculated dose levels in Tables 5-8. For each of the six disk specimen dose levels there are four Path A type alloys in a total of eight conditions, two Path E type alloys, and one pure metal. At the lowest disk dose level, three additional pure metals and eight binary alloys were included. The A533 ferritic alloy disk specimens were obtained from Charpy-V-Notch specimen blank 3PT-34. This charpy specimen, in turn, was cut from plate 03 of ASTM A-533 Grade B class 1 steel, a well-characterized Heavy Section Steel Technology Program steel.[3] In most cases, 3 specimens will be set aside for both TEM and microhardness followed by postirradiation annealing studies. The balance of the specimens will be available for reconstitution into another, higher dose, experiment.

TABLE 5

HEDL-VR TEM DISK SPECIMEN MATRIX

Dose: 3.3 . 10^{18} n/cm^2, E$\sim$14 MeV

T_i: 80 and 288°C

Path A Type Alloys	Condition	μH/Recon.	μH/TEM	μH/PIA
FFTF 1st Core 316 SS	20% CW	0	3	3
FFTF 1st Core 316 SS	Rxl	0	3	3
MFE 316 SS	40% CW	5	3	3
MFE 316 SS	Rxl	7	3	3
PCA	40% CW	4	3	3
PCA	Rxl		3	3
Fe-15Cr-20Ni (E-19)	30% CW	2	3	3
Fe-15Cr-20Ni (E-19)	Rxl	3	3	3
Path E Type Alloys				
HT-9	A & T	0	3	3
A533	A & T	0	3	3
Pure Metals				
Ni	Rxl	3	3	3
V	Rxl	0	0	0
Ti	Rxl	0	0	0
Nb	Rxl	0	0	0
Binary Alloys*				
Cu-5Al	SA	0	0	0
Cu-5Ni	SA	0	0	0
Cu-5Mn	SA	0	0	0
Cu-50Ni	SA	0	0	0
Ni-5A1	SA	0	0	0
Ni-5Si	SA	0	0	0
Ni-8Si	SA	0	0	0
Ni-5Mn	SA	0	0	0

*Atomic percent

TABLE 6

HEDL-VR TEM DISK SPECIMEN MATRIX

Dose: 0.8 and 0.2 . 10^{18} n/cm^2, E ~14 MeV

T_i: 80 and 288°C

Path A Type Alloys	Condition	μH/Recon.	TEM	μH/PIA
FFTF 1st Core 316 SS	20% CW	0	2	
FFTF 1st Core 316 SS	RxI	0	2	
MFE 316 SS	40% CW	2	2	2
MFE 316 SS	RxI	0	0	0
PCA	40% CW	0	2	2
PCA	RxI	0	2	2
Fe-15Cr-20Ni(E-19)	30% CW	0	2	2
Fe-15Cr-20Ni(E-19)	RxI	0	3	2
Path E Type Alloys				
HT-9	A C T	0	2	
A533	A & T	0	1	
Pure Metals				
Ni	RxI	0	2	2
V	RxI	0	0	0
Ti	RxI	0	0	0
Nb	RxI	0	0	0
Binary Alloys*				
Cu-5Al	SA	0	0	0
Cu-5Ni	SA	0	0	0
Cu-5Mn	SA	0	0	0
Cu-50Ni	SA	0	0	0
Ni-5Al	SA	0	0	0
Ni-5Si	SA	0	0	0
Ni-8Si	SA	0	0	0
Ni-5Mn	SA	0	0	0

*Atomic percent

TABLE 7

HEDL-VR TEM DISK SPECIMEN MATRIX

Dose: 1.7 and 0.4 . 10^{18} n/cm^2, E ~14 MeV

T_i: 80 and 288°C

Path A Type Alloys	Condition	μH/Recon.	TEM	μH/PIA
FFTF 1st Core 316 SS	20% CW	2	2	2
FFTF 1st Core 316 SS	Rxl	2	2	2
MFE 316 SS	40% CW	3	3	3
MFE 316 SS	Rxl	2	2	2
PCA	40% CW	3	3	3
PCA	Rxl	0	3	2
Fe-15Cr-20Ni(E-19)	30% CW	2	2	3
Fe-15Cr-20Ni(E-19)	Rxl	3	3	3
Path E Type Alloys				
HT-9	A & T	0	3	3
A533	A & T	0	3	0
Pure Metals				
Ni	Rxl	2	2	3
V	Rxl	0	0	0
Ti	Rxl	0	0	0
Nb	Rxl	0	0	0
Binary Alloys*				
Cu-5Al	SA	0	0	0
Cu-5Ni	SA	0	0	0
Cu-5Mn	SA	0	0	0
Cu-50Ni	SA	0	0	0
Ni-5A1	SA	0	0	0
Ni-5Si	SA	0	0	0
Ni-8Si	SA	0	0	0
Ni-5Mn	SA	0	0	0

*Atomic percent

TABLE 8

HEDL-VR TEM DISK SPECIMEN MATRIX

Dose: 0.05 . 10^{18} n/cm^2, E ~14 MEV

T_i: 80 and 288°C

Path A Type Alloys	Condition	μH/Recon.	TEM	μH/PIA
FFTF 1st Core 316 SS	20% CW	0	0	3
FFTF 1st Core 316 SS	Rxl	0	0	3
MFE 316 SS	40% CW	0	3	3
MFE 316 SS	Rxl	0	0	0
PCA	40% CW	0	2	2
PCA	Rxl	0	2	2
Fe-15Cr-20Ni(E-19)	30% CW	0	0	
Fe-15Cr-20Ni(E-19)	Rxl	0	3	
Path E Type Alloys				
HT-9	A & T	0	0	2
A533	A & T	0	0	0
Pure Metals				
Ni	Rxl	0	2	
V	Rxl	3	3	
Ti	Rxl	0	0	
Nb	Rxl	0	0	4
Binary Alloys*				
Cu-5Al	SA	0	3	3
Cu-5Ni	SA	0	3	4
Cu-5Mn	SA	0	3	3
Cu-50Ni	SA	0	3	4
Ni-5Al	SA	0	3	4
Ni-5Si	SA	0	3	4
Ni-8Si	SA	0	3	4
Ni-5Mn	SA	0	3	4

*Atomic percent

VI. REFERENCES

1. 1969 Status Report on the Omega-West Reactor, with Revised Safety Analysis; H. T. Williams, O. W. Stopinski, J. L. Yarnell, A. R. Lyle, C. L. Warner, and H. L. Maine, LA-4192 Los Alamos National Laboratory, University of California, Los Alamos, NM.

2. R. E. Nygren, Comments on ERF Needs for Materials Data, November 1979, ETF Design Center, Oak Ridge, TN.

3. C. E. Childress, ORNL-TM-3193, March 1971.

VII. FUTURE WORK

Initiate and complete HEDL-In, irradiating specimens in a thermal neutron spectrum to $2 \cdot 10^{18}$ n/cm^2 E >0.1 MeV and at a temperature of 90°C. Re-initiate HEDL-VR and achieve a peak dose of 2.5 $\cdot 10^{18}$ n/cm^2 E $\sim$14 MeV and at nominal temperatures of 80 and 288°C. Reconstitute HEDL-VR and continue irradiation to peak dose levels of 1 and eventually $3 \cdot 10^{19}$ n/cm^2 E $\sim$14 MeV.

I. PROGRAM

Title: Irradiation Effects Analysis
Principal Investigator: D. G. Doran
Affiliation: Hanford Engineering Development Laboratory

II. OBJECTIVE

The objective of this effort is to design and stock an expanded matrix of simple alloys from which to draw specimens for HEDL and OAFS intercorrelation experiments aimed at studying the microchemical/microstructural evolution of alloys subjected to simulated fusion environments.

111. RELEVANT DAFS PROGRAM PLAN TASK/SUBTASK

II.C.l Effects of Material Parameters on Microstructure
II.C. 17 Microstructural Characterization

IV. SUMMARY

Thirty-six different iron based alloys, previously used on other programs, have been obtained and are being processed into TEM disks. These specimens are iron-nickel-chromium austenitic or iron-chromium ferritic alloys some of which contain small additions of carbon, silicon, titanium or molybdenum. These alloys will be used to investigate the effects of different neutron energy environments on the microstructural and mechanical properties of simple austenitic and ferritic metal systems.

V. ACCOMPLISHMENTS AND STATUS

A. Expanded Matrix of Fe-Ni-Cr Solute Alloys for HEDL Experiments - H. R. Brager and F. A. Garner (HEOL).

1. Introduction

It is now known that the microchemical evolution that occurs in irradiated Fe-Ni-Cr alloys is as important as the concurrent microstructural evolution.[1-2] Elements known to play a large role in this evolution are nickel, silicon, carbon, titanium and molybdenum.[1] The role of each of these elements is difficult to study in complex alloys, however. Therefore, the available matrix of alloys has been expanded to provide a stockpile from which to draw specimens for HEDL contributions to DAFS goals. An effort has been made to use alloys which were employed not only in previous DAFS efforts but also neutron and ion irradiation programs conducted in the U.S. Breeder Reactor Program.[3]

This report describes the composition and thermal mechanical treatment scheduled for these alloys.

2. Specimen Selection and Preparation

Specimens in the form of TEM disks have been processed from a series of iron-based alloys. Thesematerials, previously used on various irradiation effects programs, were made from high purity ingredients and cover a range of Fe-Cr-Ni austenitic or Fe-Cr ferritic base alloys, as shown in Table 1. Also, materials were used that contained minor amounts of one or two alloy additions to an austenitic or to a ferritic base alloy composition, Table 2. The primary austenitic base alloy composition, modified by minor additions, was Fe-20Ni-15Cr and is a simple ternary version of the PCA alloy employed in the ADIP program. The ferritic base alloy was Fe-12Cr, which is similar to HT-9.

The specimens are being prepared in three different conditions: solution treated, 30% cold-worked, and 30% cold-worked plus aging. It is envisioned that these specimens will be included in near-term experiments designed to be irradiated in RTNS-II, Omega-West, HFIR, ORR, and possibly EBR-II.

TABLE 1

COMPOSITION OF SIMPLE Fe-Cr-Ni AUSTENITIC OR FERRITIC ALLOYS

Alloy #	Ni	Cr	Fe
E-89	0.5	3	96
E-60	0.1	6	95
E-62	0.1	11	90
E-17	0.1	15	85
E-18	12	15	73
E-90	15	15	69
E-39	20	8	70
E-26	20	11	69
E-19	20	15	65
G-121	20	15	65
E-20	25	15	60
E-21	30	15	56
E-37	35	8	58
E-22	35	15	49
E-38	35	20	45
E-23	45	15	40

Figure 1 illustrates the compositional regime encompassed by this alloy matrix.

VI. REFERENCES

1. F. A. Garner, "The Microchemical Evolution of Irradiated Stainless Steels," Proceedings of AIME Symposium on Irradiation Phase Stability, Pittsburg, PA, October 5-9, 1980, (in press), HEOL-SA-2159.

2. H. R. Brager and F. A. Garner, "llicrochemical Evolution of Neutron-Irradiated Stainless Steel," Proceedings of ASTM 10th International Symposium on Effects of Radiation on Materials, Savannah, GA, June 3-5, 1980, (in press), HEDL-SA-2001.

3. J. F. Bates and W. G. Johnston, "Effects of Alloy Composition on Void Swelling," Radiation Effects in Breeder Reactor Structural Materials, M. L. Bleiberg and J. W. Bennett (Eds), The Metallurgical Society of the AIME, (1977), p. 625.

TABLE 2

COMPOSITIONS OF ALLOYS CONTAINING MINOR ADDITIONS (weight %)

Alloy #	Ni	Cr	Fe	C	Si	Ti	Mo	
E-72	0.1	12	88	-	-	-	1.0	
E-99	0.2	12	86	0.09	-	-	1.0	
E-96	0.8	12	84	0.20	-	-	-	
G-34	20	15	65	-	0.7	-	-	
G-36	20	15	65	-	-	0.7	-	
G-44	20	15	65	0.05	-	-	-	
6-45	20	15	65	0.12	-	-	-	
6-46	20	15	65	-	0.3	-	-	
6-48	20	15	65	-	-	-	0.5	
G-49	20	15	65	-	-	-	1.5	
6-54	20	15	65	-	0.35	0.35	-	
6-63	20	15	65	-	0.7	0.7	-	
6-70	20	15	65	-	-	0.7	0.5	
G-105	20	15	65	0.12	0.3	-	-	
G-107	20	15	65	-	0.7	-	0.5	
6-108	20	15	65	0.12	-	-	0.5	
E-34	24	15	61	0.05	-	-	-	
E-35	25	15	59	0.04	-	0.1	-	
E-104	25	15	59	-	-	-	-	.06P
E-30	25	16	58	-	0.4	-	-	

FIGURE 1

COMPOSITION OF Fe-Cr-Ni ALLOYS

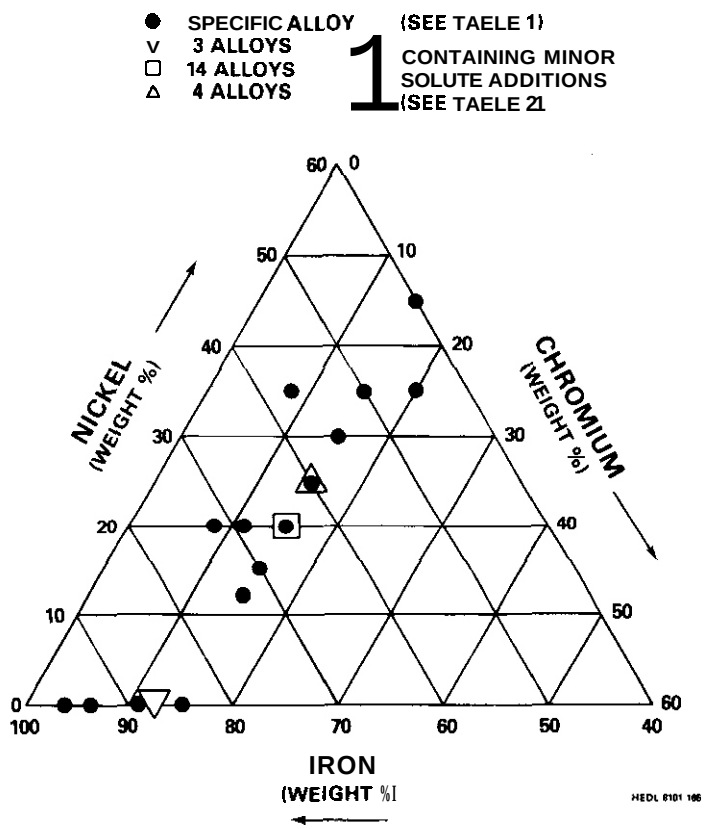

FIGURE 1. Fe-Ni-Cr Composition of Simple Alloys Being Processed into TEM Disks.

VII. FUTURE WORK

It is anticipated that all specimen preparation for this alloy series will be completed in the next reporting period.

DISTRIBUTION

UC-20 (117)

uc-2oc (79)

DOE/RRT-HQ (7)
Mail Stop B-107
Washington, DC 20545

Asst Director, Materials Tech
NA Oavies
KG Moses
JF Decker
RE Price
PB Hemmig
FT Scott

DOE/RL (3)
Richland, WA 99352

HA House
GM Chenevert
LA Pasquini

Argonne National Laboratory (4)
9700 South Cass Avenue
Argonne, IL 60439

LR Greenwood
APL Turner
A. Taylor
H. Wiedersich

Brookhaven National Laboratory
Associated Universities
Upton, NY 11973

Chairman, Nuclear Energy Dept

Columbia University
Plasma Physics Laboratory
New York, NY 10027

RA Gross

General Atomics Company (2)
P.O. Box 81608
San Diego, CA 92138

GR Hopkins

INESCO
11011 Torreyana Rd
San Diego, CA 92121

RD Stevenson

Lawrence Livermore Laboratory (2)
P.O. Box 808
Livermore, CA 94550

MW Guinan
CM Logan

Los Alamos Scientific Laboratory (2)
P.O. Box 1663
Los Alamos, NM 87544

DJ Dudziak
CR Emigh

Massachusetts Institute of Technology (3)
Cambridge, MA 02139

L. Lidsky
IW Chen
NJ Grant

McDonnell-Douglas Astronautics
P.O. Box 516
St. Louis, MO 63166

D. Kummer

Mound Laboratory
P.O. Box 32
Miamisburg, OH 45342

Manager, Tech Appl & Development

National Bureau of Standards
Gaithersburg, MD 20760

CO Bowman

DISTRIBUTION (Cont'd)

Naval Research Laboratory (2)
Metallurgy Division, Code 6390
Washington, DC 20375

I. Manning
JA Sprague

North Carolina State University
Department of Nuclear Engineering
Raleigh, NC 26707

JR Beeler, Jr.

Oak Ridge National Laboratory (7)
P.O. Box X
Oak Ridge, TN 37830

Director, Thermonuclear Oiv,
(Bldg 9201-2)
RJ Colchin, Bldg 9201-2
FG Perey
M. Roberts, Bldg 9204-1
JO Stiegler
C. Weisbin
FW Wiffen

Pacific Northwest Laboratory (4)
P.O. Box 999
Richland, WA 99352

JL Brimhall AB Johnson
T. Chikalla LC Schmid

Princeton University (2)
Plasma Physics Laboratory
Forrestal Campus
P.O. Box 451
Princeton, NJ 08540

C. Osgood
K. Wakefield

Rockwell International Energy Systems
8900 DeSoto Avenue
Canoga Park, CA 91304

O. Kramer

Sandia Laboratories (2)
Albuquerque, NM 87115

FL Vook

Sandia Laboratories
Livermore, CA 94550

WD Wilson

University of Michigan
Nuclear Engineering Department
Ann Arbor,-MI 48165

T. Kammash

University of Missouri
Dept of Mechanical and
Aerospace Engineering
1006 Engineering Bldg
Columbia, MO 65211

M. Jolles

University of Virginia
Charlottesville, VA 22901

WA Jesser

University of Wisconsin
1500 W. Johnson Drive
Madison, WI 53706

WG Wolfer

Westinghouse R&D Center (2)
Beulah Road
Pittsburgh, PA 15234

S. Wood
JA Spitznagel

DISTRIBUTION (Cont'd)

AERE Harwell
Metallurgy Division
Building 388
Oxfordshire, OX11 ORA, UK

Dr. D. R. Harries

Commission for the European Communities
200, Rue de la Loi
B-1049 Brussels, Belgium

Dr. J. Darvas

ECN
Westerdionweg 3
NL-1755 ZG Petten, The Netherlands

Dr. B. Van Der Schaaf

EIR Swiss Federal Institute for Reactor Research
CH-5303 Wuerenlingen, Switzerland

Dr. W. V. Green

GFK-IMF II
Postfach 3640
D-75 Karlsruhe 1,
Federal Republic of Germany

Dr. K. Ehrlich

HMI - Berlin,
Glienicherstrasse 100
D-1000 Berlin.
Federal Republic of Germany

Dr. H. Wollenberger

Japan Atomic Energy Research Institute
Physical Metallurgy Laboratory
Division of Nuclear Fuel Research
Fukoku Seimei Bldg
2-2, Uchisaiwai-cho 2-chome, Chiyoda-ki,
Tokyo 100, Japan

Dr. K. Shiraishi

KFA-IFF
Postfach 1913
D-517 Julich,
Federal Republic of Germany

Dr. H. Ullmaier

Materials Science Division Joint Research Center
I-21020 Ispra, Varese, Italy

Dr. P. Schiller

National Research Council
Montreal Road
Ottawa, Canada

Dr. E. V. Kornelson

SCK/CEN
Boeretang 200
B-2400 Mol, Belgium

Dr. J. Nihoul

DISTRIBUTION (Cont'd)

HEDL **(39)**

HR Brager	W/A-64	EK Dpperman	W/A-58
WL Bunch	W/C-47	NF Panayotou	W/A-53
LL Carter	W/C-47	EF Parker	W/E-17
DG Doran (5)	W/A-57	RW Powell	W/A-64
EA Evans	W/JAD-6	RJ Puigh	W/A-58
FA Garner	W/A-57	FH Ruddy	W/A-4
DS Gelles	W/A-64	FA Schmittroth	W/A-4
R. Gold	W/C-39	WF Sheely	W/C-62
HL Heinisch	W/A-57	RL Simons	W/A-57
DL Johnson	W/A-4	AL Trego	W/E-15
GD Johnson	W/A-65	GL Wire	W/A-58
NE Kenny	W/C-115	HH Yoshikawa	W/A-44
FM Mann	W/A-5	Central Files (5)	W/C-110
WN McElroy	W/C-39	Publ Services (2)	W/C-115
RE Nygren	W/A-58	Doc Management	W/C-125